J. Plasma Phys. (2026), *vol*. 92, E113 © The Author(s), 2026. Published by Cambridge University Press.
This is an Open Access article, distributed under the terms of the Creative Commons Attribution licence (https://creativecommons.org/licenses/by/4.0/), which permits unrestricted re-use, distribution and reproduction, provided the original article is properly cited. doi:10.1017/S0022377826102153

The 3-D linear stability CASTOR3D code and its applications

Erika Strumberger[1], Jonas Puchmayr[1], Mike Dunne[1], Sibylle Günter[1], Florian Hindenlang[1], Gabriella Pautasso[1], the ASDEX Upgrade Team[1,†] and the W7-X Team[2,‡]

[1]Max Planck Institute for Plasma Physics, Boltzmannstr. 2, Garching 85748, Germany
[2]Max Planck Institute for Plasma Physics, Wendelsteinstr. 1, Greifswald 17491, Germany

Corresponding author: Jonas Puchmayr, Jonas.Puchmayr@ipp.mpg.de

(Received 28 May 2026 UTC; revision received 17 July 2026 UTC; accepted 20 July 2026 UTC)

The CASTOR3D code is a linear, extended, magnetohydrodynamic stability code that can be applied to tokamak and stellarator equilibria with and without ideal and resistive complex wall and coil structures in the surrounding vacuum region. The code enables the investigation of the effects of resistivity, parallel viscosity, gyroviscosity, ion drift velocity, ExB-velocity, electron diamagnetic drift, parallel heat conductivity and externally driven flows on growth rate, oscillation frequency and mode structure. This review article describes the three-dimensional (3-D) linear stability CASTOR3D code, its versatile application possibilities (e.g. ideal and resistive modes, vertical stability investigations, edge stability limit studies in presence of magnetic perturbation fields, resistive wall modes, etc.) and interesting effects concerning 3-D plasma configurations (e.g. toroidal mode coupling leading to overstable modes, mode locking, critical rotation threshold for locked modes and non-uniform rotation).

Key words: fusion plasma, plasma instabilities, plasma simulation

1. Introduction

Linear magnetohydrodynamic (MHD) stability codes are important tools to investigate the stability properties of fusion plasmas which are magnetically confined in tokamak or stellarator devices.

Axisymmetric tokamaks were the favoured fusion devices for many years. However, the axisymmetry is perturbed by the toroidal field ripple and by error fields. The latter result, for example, from imperfections of the magnetic field coils, ferromagnetic inserts, etc. Although these error fields are small, they constrain the operational space of a tokamak. Error fields can deteriorate the confinement,

[†]For the ASDEX Upgrade Team see the author list: T. Pütterich *et al*. Nucl. Fusion **66** (2026) 116002. https://doi.org/10.1088/1741-4326/ae61c8.

[‡]For the Wendelstein 7-X Team see the author list: O. Grulke *et al*. Nucl. Fusion **64** (2024) 112002. https://doi.org/10.1088/1741-4326/ad2f4d.

https://doi.org/10.1017/S0022377826102153 Published online by Cambridge University Press

intensify the growth of instabilities, reduce the toroidal rotation, lock modes and cause disruptions. So, they became a main topic in fusion research. So-called saddle coils were installed in many devices to investigate the effects and to reduce the error fields (e.g. Hender *et al*. 1992; La Haye *et al*. 1992; Buttery *et al*. 1999). Besides, special error field correction coils were integrated in various tokamaks in order to achieve an optimal correction of the error fields (e.g. Barlow *et al*. 2001; Piron *et al*. 2020). Yet, the use of such coils is not limited to the compensation of error fields. Depending on their number and location, they can be used to probe the plasma stability (Piron *et al*. 2023), to control resistive wall modes (Okabayashi *et al*. 2005) and to mitigate or even suppress edge localised modes (ELMs) (e.g. Evans *et al*. 2004; Liang *et al*. 2007; Suttrop *et al*. 2011; Nazikian *et al*. 2015).

Nowadays, stellarators are again a subject of focus in nuclear fusion research. Their inherent properties, namely steady-state operation and the absence of disruptions, are especially important requirements for a fusion power plant (Warmer *et al*. 2024). Ongoing optimisation of the magnetic field geometries leads to major improvements of their confinement properties. There are quasisymmetric and quasiisodynamic devices. Using magnetic coordinates (Boozer coordinates (Boozer 1982)), the magnetic field strength of quasisymmetric stellarators is symmetric in toroidal direction (quasiaxisymmetric (QA) (Nührenberg *et al*. 1994; Henneberg *et al*. 2019)), in helical direction (quasihelically symmetric (Nührenberg & Zille 1988)) or in poloidal direction (quasipoloidally symmetric (Spong *et al*. 2005)). Quasiisodynamic stellarators have no explicit quasisymmetry, but their contours of the magnetic field strength are closed poloidally and the magnetic field is optimised to confine the trapped particles (Goodman *et al*. 2023; Lion *et al*. 2025). Figure 1 shows examples of a three-dimensional (3-D) tokamak equilibrium, a QA and a quasiisodynamic stellarator equilibrium. Here, the tokamak equilibrium is 3-D because of an additional two-periodic perturbation field produced by the magnetic perturbation (MP) coils shown in figure 1(*a*). In the considered case, the phase offset of the upper coil ring relative to the lower ring amounts to $\delta\phi = -90^{\circ}$. This weak perturbation field (normal component: $b_N \approx \pm 8$ mT) leads to a small corrugation[1] of the flux surfaces. Here, the maximum corrugation of the plasma boundary amounts to $\delta_N \approx \pm 0.8$ cm.

Due to their 3-D geometry, the numerical description of 3-D tokamaks and stellarators is much more complicated than for axisymmetric tokamaks. There exist numerous numerical tools to investigate the linear stability properties of axisymmetric tokamak plasmas, but only few for 3-D tokamak and stellarator plasmas. Linear stability codes can be subdivided into two major groups. The first group makes use of the ideal MHD energy principle. Axisymmetric codes of this group are, for example, PEST (Grimm *et al*. 1976), PEST 2 (Grimm, Dewar & Manickam 1983), ERATO (Gruber *et al*. 1981), GATO (Bernard, Helton & Moore 1981), KINX (Degtyarev *et al*. 1997), MINERVA-DI (Aiba 2016) and ELITE (Wilson *et al*. 2002), while DCON3D (Glasser 2025), CAS3D (Schwab 1993; Nührenberg 2016) and TERPSICORE (Anderson *et al*. 1990; Fu *et al*. 1992) are 3-D codes. A mathematical formulation of the weak form of the stability equation with flow was implemented in the CAS3D code in order to describe the perpendicular ExB flow in stellarators (Nührenberg 2021), whereas TERPSICHORE provides a treatment of the pressure anisotropy (Moen & Suzuki 2023). The second group of codes

[1]For the definition of the corrugation see Strumberger *et al*. (2014*b*).

https://doi.org/10.1017/S0022377826102153 Published online by Cambridge University Press

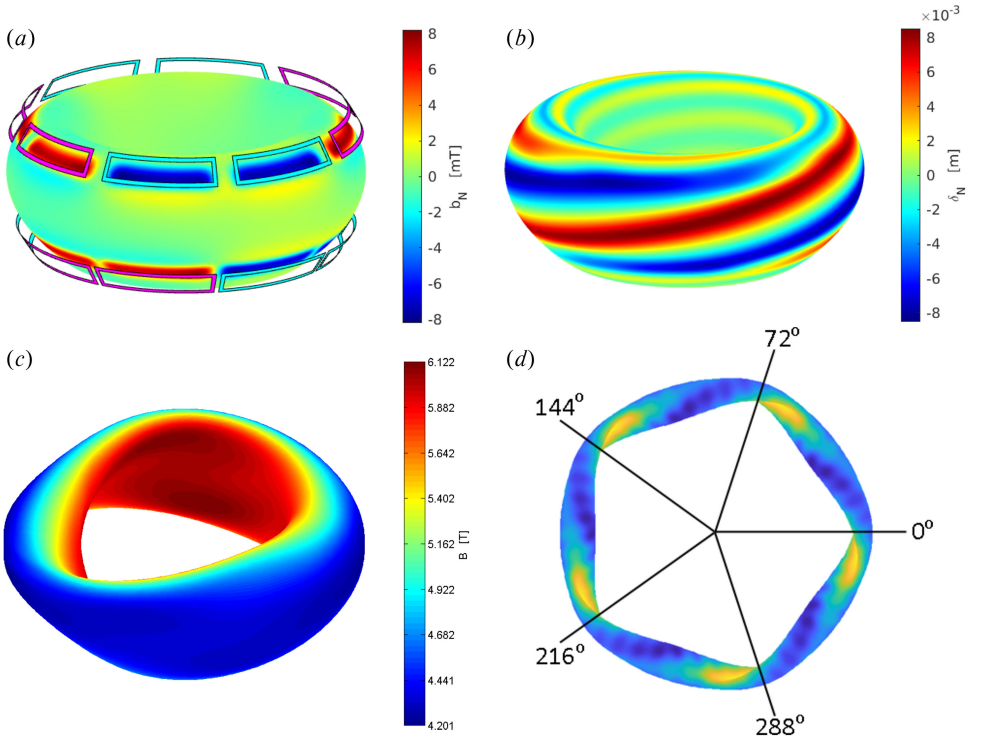


FIGURE 1. (*a,b*) The AUG-type equilibrium with MP coils. The colours of the plasma boundary mark (*a*) the normal component of the MP perturbation field and (*b*) the corrugation caused by the MP field. The colours of the MP coils indicate the antipodal coil currents. (*c*) Two-periodic QA equilibrium (reproduced with permission from Nucl. Fusion vol. 59, 2019, p. 106008 and EUROfusion; copyright EURATOM 2019) and (*d*) five-periodic W7-X equilibrium with the colours indicating the magnetic field strength B (reproduced with permission from Nucl. Fusion vol. 60, 2020, p. 106013 and EUROfusion; copyright EURATOM 2020). The colour range in (*d*) corresponds to 2.1 (dark blue) $\leqslant B \leqslant$ 2.9 T (yellow).

solves the linearised MHD equations. Examples of those codes are MISHKA-D (Huysmans *et al*. 2001), MISHKA-F (Chapman *et al*. 2006), MARS-F (Liu *et al*. 2000), MARS-K (Liu *et al*. 2008) and CASTOR (Kerner *et al*. 1991; Huysmans, Goedbloed & Kerner 1993; Kerner *et al*. 1998). While these codes take several physical effects into account simultaneously, their application is restricted to axisymmetric plasma equilibria. The CarMa code (Portone *et al*. 2008) and its extended version CarMa-D (Bonotto *et al*. 2020) result from the coupling of the 3-D eddy current integral formulation of the CARIDDI code (Albanese & Rubinacci 1988, 1997) with the two-dimensional (2-D) MARS-F (Liu *et al*. 2000) and MARS-K (Liu *et al*. 2008) stability code, respectively. They investigate resistive wall modes of axisymmetric equilibria including a detailed description of 3-D conducting structures of finite width[2] surrounding the plasma.

The CASTOR3D code (Strumberger & Günter 2017) makes use of the thin wall approximation (Merkel & Strumberger 2015). Figure 2 shows the plasma facing

[2]The finite width becomes important if the penetration depth is comparable to the width of the wall structure or smaller (Bonotto *et al*. 2020).

https://doi.org/10.1017/S0022377826102153 Published online by Cambridge University Press

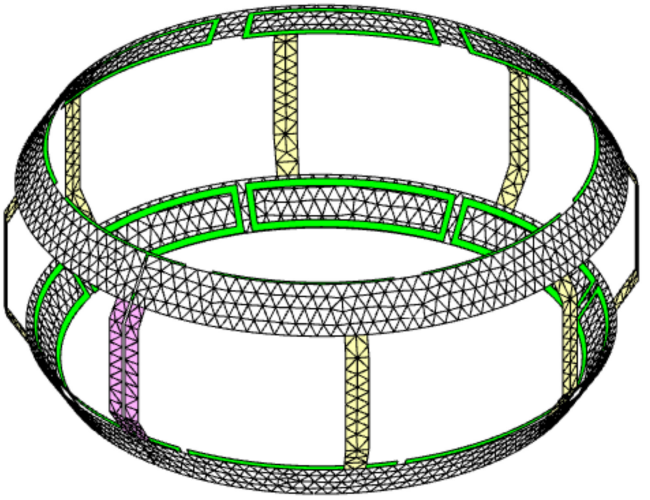


FIGURE 2. The PSL (grey) of AUG with support (yellow) and current (magenta) bridges and MP coils (green) presented in the thin wall approximation.

surfaces of the passive stabilisation loop (PSL) of ASDEX upgrade (AUG) with support and current bridges and the 16 MP coils as used by the CASTOR3D code. Neglecting their finite width, these multiply connected surface structures are represented by triangles which have different conductivities indicated by various colours, while Fourier representations are used for the plasma boundary and simple, smooth, closed wall structures. To our knowledge, CASTOR3D is the only code that includes two fluid and resistive wall effects and can be applied to 2-D (Strumberger *et al*. 2023; Vanovac *et al*. 2026) and 3-D equilibria (Strumberger & Günter 2019; Strumberger *et al*. 2020; Puchmayr *et al*. 2023; Puchmayr *et al*. 2023, 2024).

The acronym CASTOR3D stands for 'complex Alfvén spectrum of toroidal plasmas' with '3D' indicating its ability to handle 3-D equilibria. The 2-D CASTOR code (Kerner *et al*. 1998) and CASTOR3D have only the name and the weak formulation of the eigenvalue problem in common. The CASTOR3D also uses a Fourier finite-element discretisation in a flux coordinate system, and its ansatz for the test and eigenfunctions is similar to the 2-D CASTOR code. Besides those similarities of the used method, the CASTOR3D code is a completely new code. Its main characteristics are: (i) inclusion of kinetic effects (e.g. diamagnetic effects, viscosity, etc.) in the MHD equations by expressing them in terms of low-order fluid moments (Chang & Callen 1992*b*); (ii) weak formulation of the MHD equations in 3-D general flux coordinates; (iii) integration of modified routines of the STARWALL code (Merkel & Strumberger 2015) to compute the vacuum response and to take multiply connected resistive wall and coil structures into account in the vacuum region; (iv) combination of the MHD equations with the vacuum equations to an extended eigenvalue problem which enables the inclusion of plasma inertia and wall resistivity simultaneously; (v) many-valued current potentials (Lüst & Martensen 1960) used in the STARWALL part allow a correct treatment of vertical instabilities; (vi) efficient solution of the 3-D non-Hermitian eigenvalue problem by using the parallelised SLEPc Krylov–Schur solver (Roman *et al*. 2025); (vii) besides growth rates, oscillation frequencies and Fourier spectra of the modes, the CASTOR3D code also yields the mode structures in real space; (viii) the resistive energy functional, which

https://doi.org/10.1017/S0022377826102153 Published online by Cambridge University Press

is implemented in the diagnostic part of CASTOR3D, is used to analyse the energetic composition of the eigenfunctions. It provides information on the different energetic drives and stabilising phenomena of the instability (Puchmayr, Dunne & Strumberger 2022).

The CASTOR3D code was already successfully applied to external kink modes with low toroidal mode numbers in a QA stellarator configuration including parallel viscosity and toroidal flow (Strumberger & Günter 2019), and to resistive internal kink and double tearing modes (DTMs) in Wendelstein 7-X (W7-X) (Strumberger *et al*. 2020). Diamagnetic drift effects were studied for ideal and resistive internal kink modes using simple axisymmetric and 3-D test equilibria (Strumberger *et al*. 2023), and CASTOR3D was also used for benchmarks with nonlinear extended MHD codes (e.g. JOREK (Pamela *et al*. 2020; Nikulsin *et al*. 2022; Ramasamy *et al*. 2024) and NIMSTELL (Patil & Sovinec 2024)). While former 3-D CASTOR3D stability calculations were restricted to low toroidal mode numbers, now stability studies are also possible for peeling–ballooning modes in 3-D tokamak (Puchmayr *et al*. 2023, 2024) and stellarator configurations (Strumberger, Puchmayr & Hindenlang 2025) because of increasing memory and computing power, substantial improvement of the performance of the CASTOR3D code (Puchmayr 2023) and, last but not least, using high fidelity equilibrium solutions computed with the GVEC code (Hindenlang *et al*. 2025*a*).

The article is organised as follows. The underlying theoretical basis of the CASTOR3D code is described in § 2. The first part (§ 2.1) concerns the plasma, that is, the extended MHD equations, their linearisation and weak formulation and the boundary conditions. The second part (§ 2.2) deals with the vacuum energy functional, the vacuum equations and the conducting structures surrounding the plasma, whereas the various types of eigenvalue problems solved by CASTOR3D are subject of § 2.3. The structure and details of the CASTOR3D code are described in § 3. Section 4 gives an overview of stability studies performed with the CASTOR3D and interesting results concerning internal kink and interchange modes (§ 4.1), double tearing and internal resistive kink modes (§ 4.2), locked modes (§ 4.3), edge localised and external modes (§ 4.4), overstable modes (§ 4.5), resistive wall modes (§ 4.6) and vertical instabilities (§ 4.7). A short summary and an outlook to further extensions and applications of the code are given in § 5. Finally, the appendices contain details of the weak formulation (Appendix A) and a short description of the COTRANS code (Appendix B). The latter provides the Fourier representation of equilibrium quantities as needed by the CASTOR3D code.

2. Theory

Resistive wall structures surrounding the plasma complicate the solution of the eigenvalue problem because the vacuum response depends on the eigenvalue. Often, resistive wall mode codes (e.g. CarMa (Portone *et al*. 2008) and STARWALL (Merkel & Strumberger 2015)) avoid this problem by using the so-called massless approximation, that is, neglecting the plasma inertia. Using the control surface concept, the CarMa code is a combination of the linear MHD solver MARS-F (Liu *et al*. 2000) and the 3-D CARIDDI code (Albanese & Rubinacci 1988, 1997). Neglecting plasma mass and rotation, it couples self-consistently the computation of the eddy currents in the 3-D wall structures to the solution of simplified, single-fluid, ideal and linearised MHD equations for axisymmetric plasma configurations. To treat resistive wall mode problems in the case of 3-D plasma configurations and

https://doi.org/10.1017/S0022377826102153 Published online by Cambridge University Press

in the presence of 3-D resistive conducting structures, the STARWALL code uses the thin wall approximation. It takes the potential energy matrix of the plasma provided by the ideal CAS3D code[3] (Nührenberg 1996) and makes use of a Lagrangian which describes the magnetic energy of the currents in the plasma boundary and in the external wall and coil structures. Applying a variational procedure (Haney & Freidberg 1989), an eigenvalue problem was derived which yields the growth rates of slow resistive wall modes. However, the growth rates of realistic plasma configurations are not necessarily slow enough to justify the negligence of the plasma inertia. The plasma may have a finite velocity, and resistivity and/or drift effects may be important. Therefore, Bonotto *et al*. (2020) improved the CarMa code, called CarMa-D, taking into account plasma dynamics, toroidal rotation and drift-kinetic damping. Concerning the CASTOR3D code, we coupled the linearised MHD equations including resistivity, flow and drift effects with the vacuum equations used in the STARWALL code to an extended eigenvalue problem which correctly accounts for the plasma inertia. It comprises the MHD equations and the equations derived from the vacuum energy functional. In the first part of this section, we will discuss the plasma part of the eigenvalue problem.

2.1. *Plasma part*

2.1.1. Extended MHD equations

The 2-D CASTOR code is based upon the resistive single-fluid MHD equations (Kerner *et al*. 1998). We extended these equations step by step including the viscous force density $-\nabla\cdot\boldsymbol{\Pi}$, the heat flux term $(\Gamma-1)(m_i/\rho)\nabla\cdot\boldsymbol{q}$, the electron pressure term $(\alpha/\rho)\nabla p_e$ and the Hall term $(\alpha/\rho)\boldsymbol{j}\times\boldsymbol{B}$. The extended MHD equations read (Schnack *et al*. 2006)

$$\frac{\partial\rho}{\partial t}=-\boldsymbol{V}\cdot\nabla\rho-\rho\nabla\cdot\boldsymbol{V}, \tag{2.1}$$

$$\rho\frac{\partial\boldsymbol{V}}{\partial t}=-\rho(\boldsymbol{V}\cdot\nabla)\boldsymbol{V}-\nabla p-\nabla\cdot\boldsymbol{\Pi}+\boldsymbol{j}\times\boldsymbol{B}, \tag{2.2}$$

$$\frac{\partial T}{\partial t}=-\boldsymbol{V}\cdot\nabla T-(\Gamma-1)T\nabla\cdot\boldsymbol{V}-(\Gamma-1)\frac{m_i}{\rho}\nabla\cdot\boldsymbol{q}, \tag{2.3}$$

$$\boldsymbol{E}=-\boldsymbol{V}\times\boldsymbol{B}-\frac{\alpha}{\rho}\nabla p_e+\frac{\alpha}{\rho}\boldsymbol{j}\times\boldsymbol{B}+\eta\boldsymbol{j} \tag{2.4}$$

with $\alpha=\alpha_s(m_i/e)$, ion mass m_i, elementary charge e and scaling parameter α_s.[4] These equations are derived from the two-fluid MHD equations (Braginskii 1965) making several assumptions and approximations, e.g. assuming quasineutrality $n=n_i=n_e$ ($n_i=$ ion density, $n_e=$ electron density), neglecting the electron mass m_e ($m_i\gg m_e$, mass density $\rho=m_in+m_en\approx m_in$), using the pressure $p=p_i+p_e=n(T_i+T_e)=nT$ ($T_i=$ ion temperature, $T_e=$ electron temperature, $T=T_i+T_e$) and making the velocity approximation $\boldsymbol{V}=((m_i\boldsymbol{V}_i+m_e\boldsymbol{V}_e)/(m_i+m_e)\approx\boldsymbol{V}_i)$ with $\boldsymbol{V}_i$ being the ion velocity. The set of equations is closed with the Maxwell equations

$$\nabla\cdot\boldsymbol{E}=0,\quad \nabla\times\boldsymbol{E}=-\frac{\partial\boldsymbol{B}}{\partial t},\quad \nabla\times\boldsymbol{B}=\mu_0\boldsymbol{j},\quad \nabla\cdot\boldsymbol{B}=0 \tag{2.5}$$

[3]Code for the analysis of the MHD stability of 3-D equilibria.

[4]The scaling parameter α_s was implemented in CASTOR3D in order to scale the strength of the ion and electron diamagnetic drift effects.

https://doi.org/10.1017/S0022377826102153 Published online by Cambridge University Press

($\boldsymbol{E}$ = electric field, $\boldsymbol{B}$ = magnetic field, $\boldsymbol{j}$ = current density). Here, the displacement current $\mu_0\epsilon_0(\partial \boldsymbol{E}/\partial t)$ is neglected.

In CASTOR3D, the ion velocity

$$\boldsymbol{V}_i = \underbrace{\frac{\boldsymbol{E}\times\boldsymbol{B}}{B^2}}_{=\boldsymbol{V}_{ExB}} + \underbrace{\frac{\alpha}{\rho}\frac{\boldsymbol{B}\times\nabla p_i}{B^2}}_{=\boldsymbol{V}_i^*} + \boldsymbol{V}^{ext} \tag{2.6}$$

is implemented with ExB-velocity $\boldsymbol{V}_{ExB}$, ion diamagnetic drift velocity $\boldsymbol{V}_i^*$ and an externally driven velocity $\boldsymbol{V}^{ext}$. Drives of the latter are, for example, neutral beam injection, ion cyclotron range of frequencies waves, etc. (Rice 2016).

The viscous stress tensor $\boldsymbol{\Pi}$ splits into $\boldsymbol{\Pi} = \boldsymbol{\Pi}_\parallel + \boldsymbol{\Pi}_\wedge + \boldsymbol{\Pi}_\perp$ with parallel $\boldsymbol{\Pi}_\parallel$, cross (gyroviscous) $\boldsymbol{\Pi}_\wedge$ and perpendicular $\boldsymbol{\Pi}_\perp$ parts. The parallel viscous force density is approximated by

$$-\nabla\cdot\boldsymbol{\Pi}_\parallel \approx \mu_\parallel \Delta_\parallel \boldsymbol{V} \tag{2.7}$$

with $\mu_\parallel$ being the dynamic viscosity coefficient. We neglect the perpendicular viscous force density $-\nabla\cdot\boldsymbol{\Pi}_\perp$ and use

$$-\nabla\cdot\boldsymbol{\Pi}_\wedge \approx \rho(\boldsymbol{V}_i^*\cdot\nabla)\boldsymbol{V} \tag{2.8}$$

for the gyroviscous force density (Chang & Callen 1992*a*). This expression is generally known as gyroviscous cancellation. Using (2.7) and (2.8), the momentum equation (2.2) reads

$$\rho\frac{\partial \boldsymbol{V}}{\partial t} = -\rho((\boldsymbol{V}-\boldsymbol{V}_i^*)\cdot\nabla)\boldsymbol{V} - \nabla p + \mu_\parallel\nabla_\parallel\boldsymbol{V} + \boldsymbol{j}\times\boldsymbol{B}. \tag{2.9}$$

Presently, only the parallel part (Braginskii 1965)

$$\boldsymbol{q}_\parallel = \boldsymbol{q}_{\parallel e} + \boldsymbol{q}_{\parallel i} = -\kappa_{\parallel e}\nabla_\parallel T_e - \kappa_{\parallel i}\nabla_\parallel T_i \tag{2.10}$$

of the heat flux $\boldsymbol{q} = \boldsymbol{q}_\parallel + \boldsymbol{q}_\wedge + \boldsymbol{q}_\perp$ is included in the energy equation (2.3) with $\kappa_{\parallel e}$ and $\kappa_{\parallel i}$ being the electron and ion thermal conductivity coefficients and $\nabla_\parallel = (1/B^2)\boldsymbol{B}(\boldsymbol{B}\cdot\nabla)$. Besides, $\Gamma = 5/3$ is used as adiabatic index, η denotes the plasma resistivity and μ_0 is the vacuum permeability.

The extended Ohm's law (2.4) is simplified by using the drift approximation of the Hall term (Schnack *et al*. 2006)

$$\nabla_\perp p \approx \boldsymbol{j}\times\boldsymbol{B} \tag{2.11}$$

which leads to

$$\boldsymbol{E} = -\boldsymbol{V}\times\boldsymbol{B} - \frac{\alpha}{\rho}\nabla_\parallel p_e + \frac{\alpha}{\rho}\nabla_\perp p_i + \eta\boldsymbol{j}. \tag{2.12}$$

Single-fluid codes which include two-fluid effects often use the assumption $p_i = p_e = 0.5p$, that is, $T_i = T_e$. Since measured ion and electron temperatures may be different, we use

$$p_i = \alpha_T p = n\alpha_T T \quad \text{and} \quad p_e = (1-\alpha_T)p = n(1-\alpha_T)T \tag{2.13}$$

with $0 \leqslant \alpha_T \leqslant 1$. The parameter α_T provides an additional degree of freedom that allows to choose a more realistic ratio of ion and electron pressures with respect to

https://doi.org/10.1017/S0022377826102153 Published online by Cambridge University Press

the measured temperatures, so that a more realistic treatment of the ion and electron diamagnetic drift effects and the heat flux is possible. Application of the relations (2.13) to the ion drift velocity (2.6), the heat flux (2.10) and the pressure terms of Ohm's law (2.12) yields

$$\boldsymbol{V}_i^* = \frac{\alpha\alpha_T}{\rho}\frac{\boldsymbol{B}\times\nabla p}{B^2}, \tag{2.14}$$

$$\boldsymbol{q}_\parallel = -(\kappa_{\parallel e}(1-\alpha_T)+\kappa_{\parallel i}\alpha_T)\nabla_\parallel T \tag{2.15}$$

and

$$\boldsymbol{E} = -\boldsymbol{V}\times\boldsymbol{B} - \frac{\alpha}{\rho}\nabla_\parallel p + \frac{\alpha\alpha_T}{\rho}\nabla p + \eta\boldsymbol{j}. \tag{2.16}$$

2.1.2. Linearised extended MHD equations

We use $\boldsymbol{B} = \nabla\times\boldsymbol{A}$ ($\boldsymbol{A}$ = magnetic vector potential) to fulfil $\nabla\cdot\boldsymbol{B} = 0$, and the Weyl gauge (electric scalar potential $\Phi_E = 0$) yields $\boldsymbol{E} = -(\partial\boldsymbol{A}/\partial t)$. The time dependence of the perturbed quantities is assumed to be $\sim \mathrm{e}^{\lambda t}$ with eigenvalue

$$\lambda = \gamma + \mathrm{i}\omega. \tag{2.17}$$

Here, γ is the growth rate and ω the oscillation frequency of the mode. Using the ansatz $f(\boldsymbol{r},t) = f_0(\boldsymbol{r}) + \mathrm{e}^{\lambda t} f_1(\boldsymbol{r})$ for ρ, $\boldsymbol{V}$, T and $\boldsymbol{A}$, the linearised forms of the extended fluid equations (2.1, 2.9, 2.3, 2.16) read

$$\lambda\rho_1 = -\boldsymbol{V}_0\cdot\nabla\rho_1 - \boldsymbol{V}_1\cdot\nabla\rho_0 - \rho_1\nabla\cdot\boldsymbol{V}_0 - \rho_0\nabla\cdot\boldsymbol{V}_1, \tag{2.18}$$

$$\begin{aligned}\rho_0\lambda\boldsymbol{V}_1 = {}& -\rho_1(\boldsymbol{V}_0\cdot\nabla)\boldsymbol{V}_0 - \rho_0(\boldsymbol{V}_1\cdot\nabla)\boldsymbol{V}_0 - \rho_0(\boldsymbol{V}_0\cdot\nabla)\boldsymbol{V}_1\\ &+ \rho_1(\boldsymbol{V}_{i0}^*\cdot\nabla)\boldsymbol{V}_0 + \rho_0(\boldsymbol{V}_{i1}^*\cdot\nabla)\boldsymbol{V}_0 + \rho_0(\boldsymbol{V}_{i0}^*\cdot\nabla)\boldsymbol{V}_1\\ &- \frac{1}{m_i}\nabla(\rho_0 T_1) - \frac{1}{m_i}\nabla(T_0\rho_1) + \mu_{||}\Delta_{||}\boldsymbol{V}_1\\ &+ \frac{1}{\mu_0}(\nabla\times(\nabla\times\boldsymbol{A}_1))\times(\nabla\times\boldsymbol{A}_0)\\ &+ \frac{1}{\mu_0}(\nabla\times(\nabla\times\boldsymbol{A}_0))\times(\nabla\times\boldsymbol{A}_1),\end{aligned} \tag{2.19}$$

$$\begin{aligned}\lambda T_1 = {}& -\boldsymbol{V}_1\cdot\nabla T_0 - \boldsymbol{V}_0\cdot\nabla T_1 - (\Gamma-1)T_1\nabla\cdot\boldsymbol{V}_0\\ &- (\Gamma-1)T_0\nabla\cdot\boldsymbol{V}_1 - (\Gamma-1)\frac{m_i}{\rho_0}\nabla\cdot\boldsymbol{q}_{\parallel 1},\end{aligned} \tag{2.20}$$

$$\begin{aligned}\lambda\boldsymbol{A}_1 = {}& \boldsymbol{V}_1\times\boldsymbol{B}_0 + \boldsymbol{V}_0\times(\nabla\times\boldsymbol{A}_1) + \frac{\alpha}{\rho_0}\frac{1}{B_0^2}\boldsymbol{B}_0\left((\nabla\times\boldsymbol{A}_1)\cdot\frac{1}{m_i}\nabla(\rho_0 T_0)\right)\\ &+ \frac{\alpha}{\rho_0}\frac{1}{B_0^2}\boldsymbol{B}_0\left(\boldsymbol{B}_0\cdot\frac{1}{m_i}\nabla(\rho_1 T_0 + \rho_0 T_1)\right) - \alpha\alpha_T\frac{1}{\rho_0}\frac{1}{m_i}\nabla(\rho_1 T_0 + \rho_0 T_1)\\ &+ \alpha\alpha_T\frac{\rho_1}{\rho_0^2}\frac{1}{m_i}\nabla(\rho_0 T_0) - \frac{\eta}{\mu_0}(\nabla\times(\nabla\times\boldsymbol{A}_1)).\end{aligned} \tag{2.21}$$

https://doi.org/10.1017/S0022377826102153 Published online by Cambridge University Press

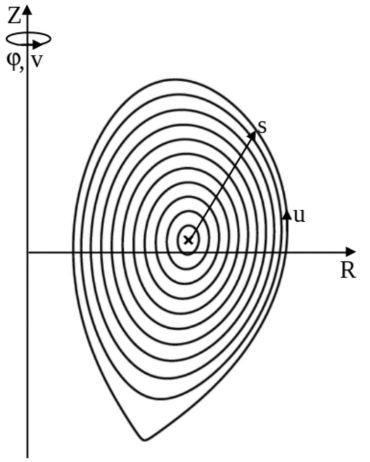


FIGURE 3. Cylindrical (R, φ, Z) and magnetic flux coordinates (s, v, u). The flux surfaces described by $s = \text{const.}$ lines are shown for a toroidal cross-section of a tokamak plasma.

Here, ρ_0, $\boldsymbol{V}_0$, T_0, $\boldsymbol{A}_0$ are the equilibrium quantities of density, ion velocity, temperature ($T_0 = T_{0e} + T_{0i}$) and magnetic vector potential, while ρ_1, $\boldsymbol{V}_1$, T_1, $\boldsymbol{A}_1$ are their perturbations. The perturbation of the ion diamagnetic drift velocity (2.14) and the parallel heat flux term $\nabla \cdot \boldsymbol{q}_{\parallel}$ read

$$\boldsymbol{V}_{i1}^{*} = -\alpha\alpha_T \frac{\rho_1}{\rho_0^2} \frac{\boldsymbol{B}_0 \times \nabla p_0}{B_0^2} + \alpha\alpha_T \frac{1}{\rho_0} \frac{\boldsymbol{B}_0 \times (T_0 \nabla \rho_1 + T_1 \nabla \rho_0 + \rho_0 \nabla T_1 + \rho_1 \nabla T_0)}{B_0^2}$$
$$+ \alpha\alpha_T \frac{1}{\rho_0} \frac{(\nabla \times \boldsymbol{A}_1) \times \nabla p_0}{B_0^2} - 2\alpha\alpha_T \frac{1}{\rho_0} \frac{\boldsymbol{B}_0 \cdot (\nabla \times \boldsymbol{A}_1)}{B_0^4} (\boldsymbol{B}_0 \times \nabla p_0) \qquad (2.22)$$

and

$$\nabla \cdot \boldsymbol{q}_{\parallel 1} = -(\kappa_{\parallel e}(1 - \alpha_T) + \kappa_{\parallel i}\alpha_T) \cdot$$
$$\left[(\boldsymbol{B}_0 \cdot \nabla) \frac{((\nabla \times \boldsymbol{A}_1) \cdot \nabla) T_0}{B_0^2} + \nabla \cdot \frac{\boldsymbol{B}_0 (\boldsymbol{B}_0 \cdot \nabla) T_1}{B_0^2} \right]. \qquad (2.23)$$

2.1.3. Weak formulation of the MHD equations

The accuracy and the numerical effort of the solution of the linearised MHD equations (2.18–2.21) depends strongly on the chosen coordinates. Since the behaviour of the plasma is extremely anisotropic with respect to the parallel and the perpendicular direction to the magnetic field $\boldsymbol{B}_0$, magnetic flux coordinates are the preferential choice. Figure 3 shows flux surfaces of a tokamak plasma at a toroidal cross-section $\varphi = \text{const.}$ and the directions of right-handed cylindrical (R, φ, Z) and magnetic flux coordinates (s, v, u). The toroidal v- and poloidal u-coordinates are angle-like variables with $0 \leqslant v < 1$ and $0 \leqslant u < 1$. Coordinate surfaces with constant radial coordinate s correspond to flux surfaces with $s = 0$ being the magnetic axis and $s = 1$ representing the plasma boundary. Using the right-handed magnetic flux coordinates and the so-called weak formulation, an eigenvalue problem is derived from

https://doi.org/10.1017/S0022377826102153 Published online by Cambridge University Press

the linearised MHD equations. For this purpose, we use a procedure analogous to the one described in Huysmans *et al*. (1993) and Kerner *et al*. (1998).

In a first step, a complex ansatz is made for the perturbed quantities

$$\rho_1 = \frac{1}{s}\hat{\rho}, \tag{2.24}$$

$$\boldsymbol{v}_1 = \frac{R^2}{\sqrt{g}}\hat{v}^s \boldsymbol{r}_{,s} + \frac{R^2}{\mathrm{i}\sqrt{g}}\hat{v}^u \boldsymbol{r}_{,u} + \frac{R^2}{\mathrm{i}u\hat{f}}\hat{v}^v \boldsymbol{B}_0, \tag{2.25}$$

$$T_1 = \frac{1}{s}\hat{T} \tag{2.26}$$

and

$$\boldsymbol{A}_1 = -\mathrm{i}\hat{A}_s \nabla s + \hat{A}_u \nabla u + \hat{A}_v \nabla v \tag{2.27}$$

with Jacobian $\sqrt{g}$, $\hat{f} = (\partial \Phi_0/\partial s)$ and Φ_0 being the toroidal flux. The ansatz is inserted into the linearised equations (2.18–2.21) which are summarised in an eigenvalue problem

$$\lambda \boldsymbol{L}\boldsymbol{w} = \boldsymbol{R}\boldsymbol{w}. \tag{2.28}$$

The symbolic vector

$$\boldsymbol{w} = (\hat{\rho}, \hat{v}^s, \hat{v}^u, \hat{v}^v, \hat{T}, \hat{A}_s, \hat{A}_u, \hat{A}_v) \tag{2.29}$$

comprises the eight variables.

For the numerical calculations, each component of $\boldsymbol{w}$ is approximated by a Fourier series[5] in the u- and v-directions and a finite element interpolation in the s-direction:

$$\begin{aligned}\hat{w}_f(s, v, u) &= \sum_{m,n,j,q} \left(a^{\mathrm{s},m,n}_{f,j,q} h^j_{f,q}(s)\sin(2\pi(mu+nv)) + a^{\mathrm{c},m,n}_{f,j,q} h^j_{f,q}(s)\cos(2\pi(mu+nv))\right) \\ &= \sum_{m,n,j,q} c^{m,n}_{f,j,q} h^j_{f,q}(s)\mathrm{e}^{2\pi\mathrm{i}(mu+nv)} + \sum_{m,n,j,q} \check{c}^{m,n}_{f,j,q} h^j_{f,q}(s)\mathrm{e}^{-2\pi\mathrm{i}(mu+nv)} = \hat{w}_{f,c} + \hat{w}_{f,\check{c}}\end{aligned} \tag{2.30}$$

with f labelling $\hat{\rho}, \hat{v}^s, \hat{v}^u, \hat{v}^v, \hat{T}, \hat{A}_s, \hat{A}_u, \hat{A}_v$. The Hermite polynomials $h^j_{f,q}(s)$ are either quadratic ($f = \hat{\rho}, \hat{v}^u, \hat{v}^v, \hat{T}, \hat{A}_s$)[6] or cubic ($f = \hat{v}^s, \hat{A}_u, \hat{A}_v$). The complex Fourier coefficients $\{c^{m,n}_{f,j,q}, \check{c}^{m,n}_{f,j,q}\}$ are related with the complex coefficients $\{a^{\mathrm{s},m,n}_{f,j,q}, a^{\mathrm{c},m,n}_{f,j,q}\}$ via

$$c^{m,n}_{f,j,q} = \frac{1}{2}a^{\mathrm{c},m,n}_{f,j,q} + \frac{1}{2\mathrm{i}}a^{\mathrm{s},m,n}_{f,j,q} \quad \text{and} \quad \check{c}^{m,n}_{f,j,q} = \frac{1}{2}a^{\mathrm{c},m,n}_{f,j,q} - \frac{1}{2\mathrm{i}}a^{\mathrm{s},m,n}_{f,j,q}. \tag{2.31}$$

[5]The STARWALL routines used in the vacuum part of CASTOR3D use Fourier series based on sin- and cos-functions, while e-functions are used in the plasma part. Therefore, both types of Fourier representations are used in the CASTOR3D code.

[6]Cubic Hermite polynomials have to be used for all variables if gyroviscosity in combination with plasma velocity and/or the pressure term $((\alpha\alpha_T)/\rho)\nabla p$ in Ohm's law (2.16) are taken into account because then additional first derivatives of the Hermite polynomials are needed.

https://doi.org/10.1017/S0022377826102153 Published online by Cambridge University Press

The indices m and n denote the poloidal and toroidal Fourier harmonics of the perturbation spectrum[7] and $q = 1, 2$ labels the two quadratic and the two cubic Hermite polynomials at a radial grid point j (Kerner *et al*. 1998).

The integral

$$(z, \boldsymbol{w}) = \int \mathrm{d}\tau z^* \cdot \boldsymbol{w} \tag{2.32}$$

denotes an inner product in the appropriate Hilbert space. Taking the inner product of (2.28) by using a weighting function z and by integrating over the plasma volume τ,

$$\lambda(z, \boldsymbol{L}\boldsymbol{w}) = (z, \boldsymbol{R}\boldsymbol{w}), \tag{2.33}$$

we get the matrix eigenvalue problem

$$\lambda \boldsymbol{B}\boldsymbol{x} = \boldsymbol{A}\boldsymbol{x} \tag{2.34}$$

with the eigenvector

$$\boldsymbol{x} = \left(\{c^{m,n}_{f,j,q}, \check{c}^{m,n}_{f,j,q}\}\right) \tag{2.35}$$

and the complex eigenvalue λ. The components of the weighting vector z^* read

$$\begin{aligned}\hat{z}^{*\mathrm{s},\tilde{m},\tilde{n}}_{\tilde{f},\tilde{j},\tilde{q}}(s, v, u) &= \hat{t}_{\tilde{f}} h^{\tilde{j}}_{\tilde{f},\tilde{q}}(s)\sin(2\pi(\tilde{m}u + \tilde{n}v)) \\ &= \hat{t}_{\tilde{f}} h^{\tilde{j}}_{\tilde{f},\tilde{q}}(s)\frac{1}{2\mathrm{i}}\left(\mathrm{e}^{2\pi\mathrm{i}(\tilde{m}u+\tilde{n}v)} - \mathrm{e}^{-2\pi\mathrm{i}(\tilde{m}u+\tilde{n}v)}\right)\end{aligned} \tag{2.36}$$

and

$$\begin{aligned}\hat{z}^{*\mathrm{c},\tilde{m},\tilde{n}}_{\tilde{f},\tilde{j},\tilde{q}}(s, v, u) &= \hat{t}_{\tilde{f}} h^{\tilde{j}}_{\tilde{f},\tilde{q}}(s)\cos(2\pi(\tilde{m}u + \tilde{n}v)) \\ &= \hat{t}_{\tilde{f}} h^{\tilde{j}}_{\tilde{f},\tilde{q}}(s)\frac{1}{2}\left(\mathrm{e}^{2\pi\mathrm{i}(\tilde{m}u+\tilde{n}v)} + \mathrm{e}^{-2\pi\mathrm{i}(\tilde{m}u+\tilde{n}v)}\right)\end{aligned} \tag{2.37}$$

with

$$\hat{t}_{\hat{\rho}} = \frac{1}{s}, \tag{2.38}$$

$$\hat{t}_{\hat{v}_s} = \frac{R^2}{\sqrt{g}}\boldsymbol{r}_{,s}\,, \quad \hat{t}_{\hat{v}_u} = \frac{\mathrm{i}R^2}{\sqrt{g}}\boldsymbol{r}_{,u}\,, \quad \hat{t}_{\hat{v}_v} = \frac{\mathrm{i}R^2}{\sqrt{g}}\boldsymbol{r}_{,u} - \frac{\mathrm{i}J_0}{4\pi^2\iota\hat{f}}\boldsymbol{r}_{,v} \tag{2.39}$$

$$\hat{t}_{\hat{T}} = \frac{1}{s}, \tag{2.40}$$

$$\hat{t}_{\hat{A}_s} = \mathrm{i}\nabla s, \quad \hat{t}_{\hat{A}_u} = \nabla u, \quad \hat{t}_{\hat{A}_v} = \nabla v \tag{2.41}$$

and J_0 being the equilibrium poloidal current.

More details of the weak formulation concerning the Hermite polynomials and the computation of the matrix elements are described in the Appendices A.1 and A.2. Eventually, the structures of the matrices $\boldsymbol{A}$ and $\boldsymbol{B}$, their dimensions and possibilities to reduce them are discussed in § 3.5.

[7]It should be mentioned that the spectrum of the poloidal harmonics m is generally different for each toroidal harmonic n and may be different for each radial grid point j (see also § 3.5).

https://doi.org/10.1017/S0022377826102153 Published online by Cambridge University Press

2.1.4. Boundary conditions

At the magnetic axis, the boundary conditions

$$v_1^s(s=0)=0, \quad A_{1u}(s=0)=0, \quad A_{1v}(s=0)=0 \tag{2.42}$$

result from the regularity conditions (Huysmans 1991).

If the plasma is enclosed by a perfectly conducting wall, the boundary conditions read

$$\boldsymbol{n}_\mathrm{p}\cdot\boldsymbol{v}_1=0, \quad \boldsymbol{n}_\mathrm{p}\cdot\boldsymbol{B}_1=0, \quad \boldsymbol{n}_\mathrm{p}\times\boldsymbol{E}_1=0 \tag{2.43}$$

with $\boldsymbol{n}_\mathrm{p}$ being the exterior unit normal vector at the plasma boundary. That is,

$$v_1^s(s=1)=0, \quad A_{1u}(s=1)=0, \quad A_{1v}(s=1)=0. \tag{2.44}$$

Both boundary conditions (2.42) and (2.44) are essential boundary conditions. They must be applied to the variables and the test functions (Kerner *et al*. 1998). As in the CASTOR code, these conditions are implemented in the CASTOR3D code by removing the rows and columns of the corresponding matrix elements on the magnetic axis and the plasma boundary.

If the plasma is surrounded by a vacuum region, the corresponding boundary conditions implemented in CASTOR and CASTOR3D are restricted to plasma equilibria without surface currents. That is, the equilibrium pressure has to fall to zero at the plasma boundary, $p_0(s=1)=0$, so that the equilibrium magnetic field is continuous across the plasma boundary, $\boldsymbol{B}_0=\boldsymbol{B}_0^{vac}$. Then, in the case of an ideal plasma, the normal component of the magnetic field perturbation and the total pressure perturbation

$$\boldsymbol{B}_1\cdot\boldsymbol{n}_\mathrm{p}=\boldsymbol{B}_1^{vac}\cdot\boldsymbol{n}_\mathrm{p} \quad \text{and} \quad p_1+\boldsymbol{B}_0\cdot\boldsymbol{B}_1=\boldsymbol{B}_0^{vac}\cdot\boldsymbol{B}_1^{vac} \tag{2.45}$$

are continuous at plasma boundary. It is $p_1=\rho_0 T_1+T_0\rho_1$.

In the case of resistive stability studies, surface currents are no longer allowed in the plasma perturbation. This leads to the additional condition

$$\boldsymbol{n}_\mathrm{p}\times\boldsymbol{B}_1=\boldsymbol{n}_\mathrm{p}\times\boldsymbol{B}_1^{vac}. \tag{2.46}$$

Then, the tangential components of the magnetic field perturbations are also continuous,

$$\boldsymbol{B}_0\cdot\boldsymbol{B}_1=\boldsymbol{B}_0^{vac}\cdot\boldsymbol{B}_1^{vac}, \tag{2.47}$$

and it has to be $p_1=0$ at the plasma boundary. In order to fulfil this condition, only equilibria with $p_0(s=1)=0$ and $(\partial p_0/\partial s)\big|_{s=1}=0$ are allowed for free-boundary resistive stability studies because then this condition is trivially satisfied (Huysmans *et al*. 1993).

The weak formulation of the linearised MHD equations (2.18)–(2.21) yields the following boundary terms which result from partial integration[8] of the corresponding terms in the momentum equation (2.19):

$$W^{\mathrm{s},\tilde{m},\tilde{n}}_{\hat{v}_s,\tilde{q}}=-\frac{1}{\mu_0}\int_0^1 \mathrm{d}v\int_0^1 \mathrm{d}u\; H_{\tilde{q}}\sin(2\pi(\tilde{m}u+\tilde{n}v))R^2\boldsymbol{B}_0\cdot\boldsymbol{B}_1^{vac})|_{s=1}, \tag{2.48}$$

$$W^{\mathrm{c},\tilde{m},\tilde{n}}_{\hat{v}_s,\tilde{q}}=-\frac{1}{\mu_0}\int_0^1 \mathrm{d}v\int_0^1 \mathrm{d}u\; H_{\tilde{q}}\cos(2\pi(\tilde{m}u+\tilde{n}v))R^2\boldsymbol{B}_0\cdot\boldsymbol{B}_1^{vac})|_{s=1} \tag{2.49}$$

[8]The partial integration is used to reduce the order of the derivatives.

https://doi.org/10.1017/S0022377826102153 Published online by Cambridge University Press

and Ohm's law (2.21),

$$W^{\mathrm{s},\tilde{m},\tilde{n}}_{\hat{A}_u,\tilde{q}} = \frac{1}{\mu_0}\int_0^1 \mathrm{d}v \int_0^1 \mathrm{d}u\; H_{\tilde{q}}\,\sin(2\pi(\tilde{m}u+\tilde{n}v))(-\eta)B^{vac}_{1v}|_{s=1}, \tag{2.50}$$

$$W^{\mathrm{c},\tilde{m},\tilde{n}}_{\hat{A}_u,\tilde{q}} = \frac{1}{\mu_0}\int_0^1 \mathrm{d}v \int_0^1 \mathrm{d}u\; H_{\tilde{q}}\,\cos(2\pi(\tilde{m}u+\tilde{n}v))(-\eta)B^{vac}_{1v}|_{s=1}, \tag{2.51}$$

$$W^{\mathrm{s},\tilde{m},\tilde{n}}_{\hat{A}_v,\tilde{q}} = \frac{1}{\mu_0}\int_0^1 \mathrm{d}v \int_0^1 \mathrm{d}u\; H_{\tilde{q}}\,\sin(2\pi(\tilde{m}u+\tilde{n}v))\eta B^{vac}_{1u}|_{s=1}, \tag{2.52}$$

$$W^{\mathrm{c},\tilde{m},\tilde{n}}_{\hat{A}_v,\tilde{q}} = \frac{1}{\mu_0}\int_0^1 \mathrm{d}v \int_0^1 \mathrm{d}u\; H_{\tilde{q}}\,\cos(2\pi(\tilde{m}u+\tilde{n}v))\eta B^{vac}_{1u}|_{s=1}. \tag{2.53}$$

The cubic Hermite polynomials are $H_1(s=1)=1$ and $H_2(s=1)=0$. That is, only terms with index $\tilde{q}=1$ do not vanish. Furthermore, the boundary terms of Ohm's law completely disappear in the case of ideal stability studies.

2.2. *Vacuum part*

The vacuum part of CASTOR3D is able to handle a smooth closed wall, several multiply connected wall structures and a number of coils simultaneously. They all can be resistive or perfectly ideal conductors. The vacuum routines consist of modified[9] subroutines of the STARWALL code (Merkel & Strumberger 2015), which uses a variational method and exploits the thin wall approximation. In the following sections, we review the basics of this method.

2.2.1. Energy functional and boundary conditions

In order to describe the basic elements, we concentrate on a configuration with one smooth closed wall, a complex multiply connected structure and N_c coils. Using the indices $i=1$ or p for the plasma boundary, $i=2$ or $\mathrm{w_f}$ for the closed wall, $i=3$ or $\mathrm{w_t}$ for the multiply connected wall and $j=1,\ldots,N_c$ for the coils, we introduce the Lagrangian

$$\begin{aligned}\mathcal{L} = {} & \frac{\mu_0}{8\pi}\sum_{i,i'=1}^{3,3}\int_{S_i}\mathrm{d}f_i\int_{S_{i'}}\mathrm{d}f_{i'}\frac{\boldsymbol{K}_i\cdot\boldsymbol{K}_{i'}}{|\boldsymbol{r}_i-\boldsymbol{r}_{i'}|} + \frac{\mu_0}{8\pi}\sum_{j,j'=1}^{N_c,N_c} I_j I_{j'}\int_{S_j}\mathrm{d}f_j\int_{S_{j'}}\mathrm{d}f_{j'}\frac{\boldsymbol{k}_j\cdot\boldsymbol{k}_{j'}}{|\boldsymbol{r}_j-\boldsymbol{r}_{j'}|}\\ & + \frac{\mu_0}{4\pi}\sum_{j,i=1}^{N_c,3} I_j\int_{S_j}\mathrm{d}f_j\int_{S_i}\mathrm{d}f_i\frac{\boldsymbol{K}_i\cdot\boldsymbol{k}_j}{|\boldsymbol{r}_i-\boldsymbol{r}_j|} - \int_{S_\mathrm{p}}\mathrm{d}f_\mathrm{p}\boldsymbol{K}_\mathrm{p}\cdot\boldsymbol{A}_1\\ & + \frac{1}{2\lambda}\sum_{i=2}^{3}\int_{S_i}\mathrm{d}f_i\frac{1}{\sigma_i d_i}\boldsymbol{K}_i\cdot\boldsymbol{K}_i + \frac{1}{2\lambda}\sum_{j=1}^{N_c} R_j I_j^2\int_{S_j}\mathrm{d}f_j\boldsymbol{k}_j^2,\end{aligned} \tag{2.54}$$

which describes the magnetic energy of the currents in the plasma boundary and in the external wall and coil structures. The latter are considered as passive conductors. The vector quantities $\boldsymbol{K}_i$ are the surface current densities on the plasma and wall surfaces, and $\boldsymbol{k}_j$ are the corresponding normalised quantities on the coil surfaces. Here I_j denotes the magnitude of the current in coil j and R_j its resistances, and σ_i

[9]Some of the routines had to be adapted to the definitions and conventions used in CASTOR3D because the modified STARWALL routines are directly integrated in the source code.

https://doi.org/10.1017/S0022377826102153 Published online by Cambridge University Press

and d_i are the specific conductivity and thickness of wall structure i.[10] The surface integrals $\int_{S_i} \mathrm{d}f_i$ and $\int_{S_j} \mathrm{d}f_j$ are performed over the plasma surface and the wall and coil surfaces. The first term of the Lagrangian (2.54) describes the magnetic energy related to the interaction of the virtual current on the plasma boundary[11] with itself and with the wall currents and the interactions of the wall currents with themselves. The second and the third terms are related to the interaction of the coil currents with themselves and with the surface current densities on the plasma boundary and the wall structures. The last three terms are boundary terms. The first boundary term depends on the vector potential perturbation $\boldsymbol{A}_1$ of the plasma while the last two terms depend on the eigenvalue λ of the plasma perturbation. The boundary terms result from the following boundary conditions.

Applying the condition that the tangential component of the electric field perturbation is continuous at the plasma boundary,

$$\boldsymbol{n}_\mathrm{p} \times \boldsymbol{E}_1^{vac} = \boldsymbol{n}_\mathrm{p} \times \boldsymbol{E}_1 \tag{2.55}$$

together with the relation $\boldsymbol{E}_1 = -\lambda \boldsymbol{A}_1$ and performing the transformations

$$\boldsymbol{n}_\mathrm{p} \cdot (\boldsymbol{K}_\mathrm{p} \times (\boldsymbol{n}_\mathrm{p} \times \boldsymbol{A}_1^{vac})) = \boldsymbol{n}_\mathrm{p} \cdot (\boldsymbol{K}_\mathrm{p} \times (\boldsymbol{n}_\mathrm{p} \times \boldsymbol{A}_1)), \tag{2.56}$$

we get

$$\boldsymbol{K}_\mathrm{p} \cdot \boldsymbol{A}_1^{vac} = \boldsymbol{K}_\mathrm{p} \cdot \boldsymbol{A}_1, \tag{2.57}$$

that is,

$$\int_{S_\mathrm{p}} \mathrm{d}f_\mathrm{p} \boldsymbol{K}_\mathrm{p} \cdot \boldsymbol{A}_1^{vac} = \int_{S_\mathrm{p}} \mathrm{d}f_\mathrm{p} \boldsymbol{K}_\mathrm{p} \cdot \boldsymbol{A}_1. \tag{2.58}$$

Similarly, the magnetic vector potentials of the wall and coil surfaces are expressed by the corresponding relations derived from Ohm's law $\boldsymbol{E} = \sigma \boldsymbol{j}$ with $\boldsymbol{j}$ being the current density. That is,

$$\boldsymbol{A}_1^{vac} = \begin{cases} \dfrac{1}{\lambda \sigma_i d_i} \boldsymbol{K}_i & \text{on resistive wall surfaces } S_i, \\ \dfrac{R_j}{\lambda} I_j \boldsymbol{k}_j & \text{on resistive coil surfaces } S_j. \end{cases} \tag{2.59}$$

2.2.2. Vacuum equations

The divergence-free surface currents $\boldsymbol{K}_i$ are derived from current potentials Φ^i,

$$\boldsymbol{K}_i = \boldsymbol{n}_i \times \nabla \Phi^i \tag{2.60}$$

with

$$\boldsymbol{n}_i = \frac{\boldsymbol{r}_{,v}^{\,i} \times \boldsymbol{r}_{,u}^{\,i}}{|\boldsymbol{r}_{,v}^{\,i} \times \boldsymbol{r}_{,u}^{\,i}|} \tag{2.61}$$

being the exterior unit normal vector on surface i.

[10] Multiply connected walls may be composed of elements with different specific conductivity and/or thickness. Here, for the sake of convenience, we neglect this detail.

[11] This virtual surface current replaces the currents flowing inside the plasma (Shafranov & Zakharov 1972).

https://doi.org/10.1017/S0022377826102153 Published online by Cambridge University Press

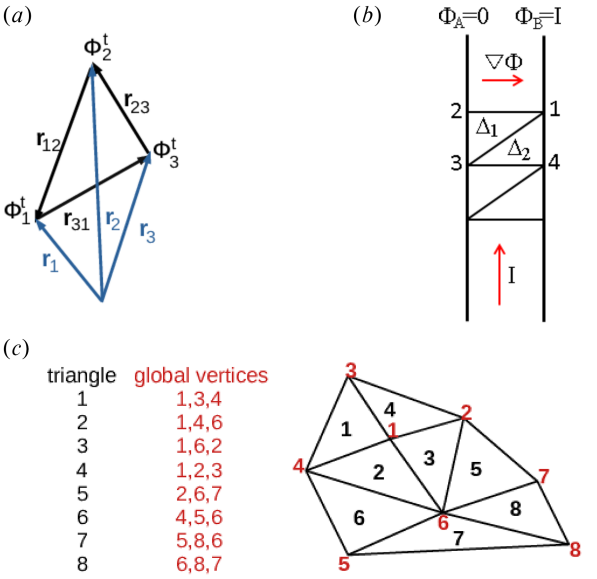


FIGURE 4. Schematic representations of (*a*) a wall triangle, (*b*) a coil segment (reproduced with permission from Nucl. Fusion vol. 57, 2017, p. 016032 and EUROfusion; copyright EURATOM 2016) and (*c*) a wall segment.

A single-valued Fourier ansatz plus net-poloidal, J^i_{pol}, and net-toroidal, I^i_{tor}, currents is made for the current potential

$$\Phi^i(u,v) = J^i_{pol} v + I^i_{tor} u + \sum_{\substack{m_i \geqslant 0, n_i \neq 0 \\ m_i > 0, n_i = 0}} \left(\hat{\Phi}^{i,\mathrm{s}}_{m_i,n_i} \sin(2\pi(m_i u + n_i v)) + \hat{\Phi}^{i,\mathrm{c}}_{m_i,n_i} \cos(2\pi(m_i u + n_i v)) \right) \tag{2.62}$$

on the plasma boundary and on the closed wall with smooth geometry. Here Φ^i is a many-valued potential. Such potentials are necessary to treat the $m = 0$, $n = 0$ harmonic of a vertical instability correctly. An $m = 0$, $n = 0$ normal displacement which corresponds to the dilation/contraction of the plasma induces a net-poloidal and a net-toroidal flux in the vacuum region. These fluxes are related with net currents in the plasma boundary and an external conductor (Lüst & Martensen 1960). Inserting (2.61) and (2.62) in to (2.60) yields

$$\boldsymbol{K}_i = \frac{1}{|\boldsymbol{r}^{\,i}_{,v} \times \boldsymbol{r}^{\,i}_{,u}|} \left(J^i_{pol} \boldsymbol{r}^{\,i}_{,u} - I^i_{tor} \boldsymbol{r}^{\,i}_{,v} \right) + \boldsymbol{n}_i \times \nabla \sum_{\substack{m_i \geqslant 0, n_i \neq 0 \\ m_i > 0, n_i = 0}} \left(\hat{\Phi}^{i,\mathrm{s}}_{m_i,n_i} \sin(2\pi(m_i u + n_i v)) + \hat{\Phi}^{i,\mathrm{c}}_{m_i,n_i} \cos(2\pi(m_i u + n_i v)) \right). \tag{2.63}$$

Walls with complex, multiply connected structures are discretised into triangles. The position vector of a triangle t (see figure 4*a*) of surface i is given by

$$\boldsymbol{r}^{i,t} = \boldsymbol{r}^{i,t}_1 + \alpha \boldsymbol{r}^{i,t}_{21} + \beta \boldsymbol{r}^{i,t}_{31}, \quad 0 < \alpha + \beta < 1, \quad \boldsymbol{r}^{i,t}_{lk} = \boldsymbol{r}^{i,t}_l - \boldsymbol{r}^{i,t}_k, \quad l,k = 1,2,3 \tag{2.64}$$

https://doi.org/10.1017/S0022377826102153 Published online by Cambridge University Press

with the vertices numbered anticlockwise. Assuming that the surface current density is constant on a triangle, it can be written as

$$\boldsymbol{K}_{i,t} = \frac{\phi_1^{i,t}\boldsymbol{r}_{23}^{i,t} + \phi_2^{i,t}\boldsymbol{r}_{31}^{i,t} + \phi_3^{i,t}\boldsymbol{r}_{12}^{i,t}}{\left|\boldsymbol{r}_{21}^{i,t} \times \boldsymbol{r}_{32}^{i,t}\right|} \tag{2.65}$$

or

$$\boldsymbol{K}_{i,t} = \sum_{h=1}^{3} \Phi_h^{i,t}\boldsymbol{e}_{i,h}^{t}, \qquad \boldsymbol{e}_{i,h}^{t} = \frac{1}{2}\epsilon_{hkl}^{i,t}\frac{\boldsymbol{r}_{kl}^{i,t}}{\left|\boldsymbol{r}_{21}^{i,t} \times \boldsymbol{r}_{31}^{i,t}\right|}. \tag{2.66}$$

Then, the total surface current density of wall structure i reads

$$\boldsymbol{K}_i = \sum_{t=1}^{N_i} \boldsymbol{K}_{i,t} = \sum_{t=1}^{N_i}\sum_{h=1}^{3} \Phi_h^{i,t}\boldsymbol{e}_{i,h}^{t} \tag{2.67}$$

with N_i being its total number of triangles.

Figure 4(c) shows a wall segment composed of triangles. Each vertex is characterised by a global node number V with $V = 1, \ldots, N_{V_i}$ and N_{V_i} being the total number of vertices of the triangulated domain i. The current potential of a multiply connected wall with boundaries and/or holes has to be constant along the edges. That is, the current-potential values have to be the same along an edge. So, the number of independent global nodes N_{G_i} is smaller than the number of vertices N_{V_i}. The connectivity tensor $\boldsymbol{H}$ dedicates the independent current potential values $\hat{\Phi}_g^i$ at the global nodes to potential values $\Phi_h^{i,t}$ at the vertices of the individual triangles:

$$\Phi_h^{i,t} = \sum_{g=1}^{N_{G_i}} \boldsymbol{H}(h, t, g)\hat{\Phi}_g^i \quad \text{with} \quad h = 1, 2, 3 \quad \text{and} \quad t = 1, \ldots, 3N_i. \tag{2.68}$$

Inserting (2.68) into (2.67) yields the total surface current density of wall structure i as function of the independent current potential values:

$$\boldsymbol{K}_i = \sum_{t=1}^{N_i}\sum_{h=1}^{3}\sum_{g=1}^{N_{G_i}} \boldsymbol{H}(h, t, g)\boldsymbol{e}_{i,h}^{t}\hat{\Phi}_g^i. \tag{2.69}$$

A coil is represented by an infinitely thin band which is discretised into triangles as shown in figure 4(b). The vertices of the triangles are located on the boundaries of the coil band. All vertices of one side are characterised by the same current potential. Usually, one potential is set to zero while the other corresponds to the amount of the total current I_j flowing through coil j. Here, we define $\Phi_{\mathrm{A}} = 0$ and $\Phi_{\mathrm{B}} = I_j$.

Using again the definition of the position vector (2.64) and assuming that the surface current density is constant on a triangle, $\boldsymbol{K}_{j,t}$ is given by

$$\boldsymbol{K}_{j,t=1} = \Phi_{\mathrm{B}}^{j}\frac{\boldsymbol{r}_{23}^{j}}{\left|\boldsymbol{r}_{12}^{j} \times \boldsymbol{r}_{32}^{j}\right|} = I_j\boldsymbol{k}_{j,t=1}, \tag{2.70}$$

$$\boldsymbol{K}_{j,t=2} = \Phi_{\mathrm{B}}^{j}\frac{\boldsymbol{r}_{14}^{j}}{\left|\boldsymbol{r}_{43}^{j} \times \boldsymbol{r}_{31}^{j}\right|} = I_j\boldsymbol{k}_{j,t=2}, \tag{2.71}$$

https://doi.org/10.1017/S0022377826102153 Published online by Cambridge University Press

etc. with $\boldsymbol{k}_{j,t}$ being the normalised surface current density of triangle t. Then, the total surface current density of coil j reads

$$\boldsymbol{K}_j = I_j \sum_{t=1}^{N_j} \boldsymbol{k}_{j,t} \tag{2.72}$$

with N_j being its total number of triangles.

Inserting (2.63), (2.69) and (2.72) into the Lagrangian (2.54) and making the variations with respect to J^{p}_{pol}, I^{p}_{tor}, $\{\hat{\Phi}^{\mathrm{p,s}}_{m_{\mathrm{p}},n_{\mathrm{p}}}\}$, $\{\hat{\Phi}^{\mathrm{p,c}}_{m_{\mathrm{p}},n_{\mathrm{p}}}\}$, $J^{\mathrm{w_f}}_{pol}$, $I^{\mathrm{w_f}}_{tor}$, $\{\hat{\Phi}^{\mathrm{w_f},s}_{m_{\mathrm{w_f}},n_{\mathrm{w_f}}}\}$, $\{\hat{\Phi}^{\mathrm{w_f,c}}_{m_{\mathrm{w_f}},n_{\mathrm{w_f}}}\}$, $\{\hat{\Phi}^{\mathrm{w_t}}_{g}\}$ and the coil currents $\{I_j\}$, we obtain the following set of equations:

$$\begin{aligned}
\boldsymbol{M}_{\mathrm{pp}}\boldsymbol{x}_{\mathrm{p}} + \boldsymbol{M}_{\mathrm{pc}}\boldsymbol{x}_{\mathrm{c}} + \boldsymbol{M}_{\mathrm{pw}}\boldsymbol{x}_{\mathrm{w}} &= \boldsymbol{R}_{\mathrm{pd}}\boldsymbol{x}_{\mathrm{d}},\\
\boldsymbol{M}_{\mathrm{cp}}\boldsymbol{x}_{\mathrm{p}} + \boldsymbol{M}_{\mathrm{cc}}\boldsymbol{x}_{\mathrm{c}} + \boldsymbol{M}_{\mathrm{wc}}\boldsymbol{x}_{\mathrm{w}} &= -\frac{1}{\lambda}\boldsymbol{R}_{\mathrm{cc}}\boldsymbol{x}_{\mathrm{c}},\\
\boldsymbol{M}_{\mathrm{wp}}\boldsymbol{x}_{\mathrm{p}} + \boldsymbol{M}_{\mathrm{wc}}\boldsymbol{x}_{\mathrm{c}} + \boldsymbol{M}_{\mathrm{ww}}\boldsymbol{x}_{\mathrm{w}} &= -\frac{1}{\lambda}\boldsymbol{R}_{\mathrm{ww}}\boldsymbol{x}_{\mathrm{w}}.
\end{aligned} \tag{2.73}$$

The symbolic vectors are

$$\boldsymbol{x}_{\mathrm{p}} = \left(\hat{\Phi}^{\mathrm{p,s}}_{1}, \ldots, \hat{\Phi}^{\mathrm{p,s}}_{N_{\mathrm{p}}}, I^{\mathrm{p}}_{pol}, \hat{\Phi}^{\mathrm{p,c}}_{1}, \ldots, \hat{\Phi}^{\mathrm{p,c}}_{N_{\mathrm{p}}}, J^{\mathrm{p}}_{tor}\right) \tag{2.74}$$

with N_{p} (m, n)-Fourier harmonics of the plasma boundary,

$$\boldsymbol{x}_{\mathrm{w}} = \left(\hat{\Phi}^{\mathrm{w_f,s}}_{1}, \ldots, \hat{\Phi}^{\mathrm{w_f,s}}_{N_{\mathrm{w_f}}}, I^{\mathrm{w_f}}_{pol}, \hat{\Phi}^{\mathrm{w_f,c}}_{1}, \ldots, \hat{\Phi}^{\mathrm{w_f,c}}_{N_{\mathrm{w_f}}}, J^{\mathrm{w_f}}_{tor}, \hat{\Phi}^{\mathrm{w_t}}_{1}, \ldots, \hat{\Phi}^{\mathrm{w_t}}_{N_{\mathrm{G_{w_t}}}}\right) \tag{2.75}$$

with $N_{\mathrm{w_f}}$ (m, n)-Fourier harmonics of the closed wall and $N_{\mathrm{G_{w_t}}}$ global nodes of the discretised wall structure,

$$\boldsymbol{x}_{\mathrm{c}} = (I_1, \ldots, I_{N_{\mathrm{c}}}) \tag{2.76}$$

with N_{c} coil currents I_j and $\boldsymbol{x}_{\mathrm{d}}$ containing the corresponding boundary elements of the eigenvector (2.35). The boundary term $\boldsymbol{R}_{\mathrm{pd}}\boldsymbol{x}_{\mathrm{d}}$ represents the connection between vacuum and plasma while $\boldsymbol{R}_{\mathrm{cc}}\boldsymbol{x}_{\mathrm{c}}$ and $\boldsymbol{R}_{\mathrm{ww}}\boldsymbol{x}_{\mathrm{w}}$ are the coil and wall boundary terms. The matrices $\boldsymbol{M}_{\mathrm{pp}}$,$\boldsymbol{M}_{\mathrm{pw}}$, ... denote the plasma–plasma $\boldsymbol{M}_{\mathrm{pp}}$, the plasma–wall $\boldsymbol{M}_{\mathrm{pw}}$, $\boldsymbol{M}_{\mathrm{wp}}$, the plasma–coil $\boldsymbol{M}_{\mathrm{pc}}$, $\boldsymbol{M}_{\mathrm{cp}}$, the wall–coil $\boldsymbol{M}_{\mathrm{wc}}$, $\boldsymbol{M}_{\mathrm{cw}}$ and the coil–coil $\boldsymbol{M}_{\mathrm{cc}}$ terms. For details concerning the computation of the matrix elements see (Merkel & Strumberger 2015).

2.3. *Types of eigenvalue problems*

2.3.1. Fixed-boundary eigenvalue problem

Assuming that the plasma boundary is a perfectly ideal conducting wall, the eigenvalue problem (2.34) reads

$$\lambda \begin{pmatrix} \boldsymbol{B}_{\mathrm{ll}} & \boldsymbol{B}_{\mathrm{ld}} \\ \boldsymbol{B}_{\mathrm{dl}} & \boldsymbol{B}_{\mathrm{dd}} \end{pmatrix} \begin{pmatrix} \boldsymbol{x}_{\mathrm{l}} \\ \boldsymbol{x}_{\mathrm{d}} \end{pmatrix} = \begin{pmatrix} \boldsymbol{A}_{\mathrm{ll}} & \boldsymbol{A}_{\mathrm{ld}} \\ \boldsymbol{A}_{\mathrm{dl}} & \boldsymbol{A}_{\mathrm{dd}} \end{pmatrix} \begin{pmatrix} \boldsymbol{x}_{\mathrm{l}} \\ \boldsymbol{x}_{\mathrm{d}} \end{pmatrix} \tag{2.77}$$

with the eigenvector (2.35)

$$\boldsymbol{x} = (\boldsymbol{x}_{\mathrm{l}}, \boldsymbol{x}_{\mathrm{d}}). \tag{2.78}$$

The index l characterises matrix and eigenvector elements of the plasma interior while d marks the boundary components. In accordance with the boundary conditions (2.44), the corresponding matrix elements of submatrix $\boldsymbol{A}_{\mathrm{dd}}$ are set to zero.

https://doi.org/10.1017/S0022377826102153 Published online by Cambridge University Press

2.3.2. Free-boundary eigenvalue problem

If the plasma is surrounded by a vacuum region with perfectly conducting wall and coil structures, the boundary terms of the Lagrangian (2.54) that are related to the dissipation of the wall and coil resistivities disappear and with them the λ-dependence of the vacuum equations (2.73). They are reduced to

$$\begin{pmatrix} \boldsymbol{M}_{\mathrm{pp}} & \boldsymbol{M}_{\mathrm{pw}} & \boldsymbol{M}_{\mathrm{pc}} \\ \boldsymbol{M}_{\mathrm{wp}} & \boldsymbol{M}_{\mathrm{ww}} & \boldsymbol{M}_{\mathrm{wc}} \\ \boldsymbol{M}_{\mathrm{cp}} & \boldsymbol{M}_{\mathrm{cw}} & \boldsymbol{M}_{\mathrm{dc}} \end{pmatrix} \begin{pmatrix} \boldsymbol{x}_{\mathrm{p}} \\ \boldsymbol{x}_{\mathrm{w}} \\ \boldsymbol{x}_{\mathrm{c}} \end{pmatrix} = \begin{pmatrix} \boldsymbol{R}_{\mathrm{pd}} \boldsymbol{x}_{\mathrm{d}} \\ 0 \\ 0 \end{pmatrix}. \tag{2.79}$$

Using the boundary condition (2.58) and inserting the definitions of the current surface density $\boldsymbol{K}_{\mathrm{p}}$ (2.60) and the normal vector $\boldsymbol{n}_{\mathrm{p}}$ (2.61) into the first boundary term of the Lagrangian (2.54), making a partial integration and using $\boldsymbol{B}_1 = \nabla \times \boldsymbol{A}_1$, leads to

$$\begin{aligned} \int_{S_{\mathrm{p}}} \mathrm{d}f_{\mathrm{p}} \boldsymbol{K}_{\mathrm{p}} \cdot \boldsymbol{A}_1^{vac} &= \int_{S_{\mathrm{p}}} \mathrm{d}f_{\mathrm{p}} \left(\frac{\sqrt{g} \nabla s}{|\boldsymbol{r}_{,v} \times \boldsymbol{r}_{,u}|} \times \nabla \Phi^{\mathrm{p}} \right) \cdot \boldsymbol{A}_1 \\ &= \int_{S_{\mathrm{p}}} \mathrm{d}u \mathrm{d}v \left(-\frac{\partial \Phi^{\mathrm{p}}}{\partial u} A_{1u} + \frac{\partial \Phi^{\mathrm{p}}}{\partial v} A_{1v} \right) \\ &= -\int_{S_{\mathrm{p}}} \mathrm{d}u \mathrm{d}v \Phi^{\mathrm{p}} \left(\frac{\partial A_{1u}}{\partial v} - \frac{\partial A_{1v}}{\partial u} \right) \\ &= -\int_{S_{\mathrm{p}}} \mathrm{d}u \mathrm{d}v \Phi^{\mathrm{p}} \sqrt{g} \nabla s \cdot (\nabla \times \boldsymbol{A}_1) = -\int_{S_{\mathrm{p}}} \mathrm{d}u \mathrm{d}v \Phi^{\mathrm{p}} \sqrt{g} B_1^s. \end{aligned} \tag{2.80}$$

Inserting Φ^{p} (2.62) and the ansatz

$$\sqrt{g} B_1^s = \sum_{m,n} d_{m,n}^{\mathrm{s}} \sin(2\pi(mu + nv)) + d_{m,n}^{\mathrm{c}} \cos(2\pi(mu + nv)) \tag{2.81}$$

into (2.80) and making the variation with respect to Φ^{p}, we obtain

$$-\int_{S_{\mathrm{p}}} \mathrm{d}u \mathrm{d}v \delta \Phi^{\mathrm{p}} \sqrt{g} B_1^s = \boldsymbol{R}_{\mathrm{pd}} \boldsymbol{d} \tag{2.82}$$

with

$$\boldsymbol{d} = \left(\left\{ d_{m,n}^{\mathrm{s}} \right\}, \left\{ d_{m,n}^{\mathrm{c}} \right\} \right), \tag{2.83}$$

and, eventually, we substitute $\boldsymbol{R}_{\mathrm{pd}} \boldsymbol{x}_{\mathbf{d}}$ by $\boldsymbol{R}_{\mathrm{pd}} \boldsymbol{d}$ in (2.79). Because of the linearity of equation system (2.79), no detailed information of the plasma magnetic field perturbation is necessary for its solution. It is sufficient to replace the vector $\boldsymbol{d}$ by a set of $2N_{mn}$[12] vectors describing unit perturbations and solving (2.79) individually for each vector. All components of such a unit vector are zero except one, e.g.

$$\boldsymbol{u} = \left(0, \ldots, 0, u_{m,n}^{\mathrm{s}} = 1, 0, \ldots, 0\right). \tag{2.84}$$

[12] For the definition of N_{mn} see § 3.5.

https://doi.org/10.1017/S0022377826102153 Published online by Cambridge University Press

The solutions of the equation system yield the vacuum magnetic field perturbation

$$\begin{aligned}\boldsymbol{B}_1^{vac} &= \sum_{i=1}^{3} \boldsymbol{B}_{1,i}^{vac} + \sum_{j=1}^{N_c} \boldsymbol{B}_{1,j}^{vac} \\ &= \frac{\mu_0}{4\pi} \sum_{i=1}^{2} \int_{S_i} \mathrm{d}f_i \boldsymbol{K}_i \times \frac{(\boldsymbol{r}-\boldsymbol{r}_i)}{|\boldsymbol{r}-\boldsymbol{r}_i|^3} - \frac{\mu_0}{4\pi} \sum_{t=1}^{N_{w_t}} \boldsymbol{K}_t \times \nabla \int_{S_t} \mathrm{d}f_t \frac{1}{|\boldsymbol{r}-\boldsymbol{r}_t|} \\ &\quad - \frac{\mu_0}{4\pi} \sum_{j}^{N_c} I_j \sum_{t}^{N_j} \boldsymbol{k}_{j,t} \times \nabla \int_{S_{j,t}} \mathrm{d}f_{j,t} \frac{1}{|\boldsymbol{r}-\boldsymbol{r}_{j,t}|}\end{aligned} \tag{2.85}$$

and, with it, the boundary elements (2.48)–(2.53) of matrix $\boldsymbol{A}$ (2.34) as functions of the unit perturbations. The set of unit perturbations matches the set of poloidal and toroidal Fourier harmonics taken into account for the plasma perturbations (2.30). So, the vacuum response to the unit perturbations contains all information of the vacuum needed for the free-boundary solution of the eigenvalue problem (2.34).

2.3.3. Extended free-boundary eigenvalue problem

In the case of resistive conducting structures in the vacuum region, the equation system (2.73)

$$\lambda \begin{pmatrix} -\boldsymbol{R}_{pd} & \boldsymbol{M}_{pp} & \boldsymbol{M}_{pw} & \boldsymbol{M}_{pc} \\ \boldsymbol{0}_{wd} & \boldsymbol{M}_{wp} & \boldsymbol{M}_{ww} & \boldsymbol{M}_{wc} \\ \boldsymbol{0}_{cd} & \boldsymbol{M}_{cp} & \boldsymbol{M}_{cw} & \boldsymbol{M}_{cc} \end{pmatrix} \cdot \begin{pmatrix} \boldsymbol{x}_d \\ \boldsymbol{x}_p \\ \boldsymbol{x}_w \\ \boldsymbol{x}_c \end{pmatrix} = - \begin{pmatrix} \boldsymbol{0}_{pp} & \boldsymbol{0}_{pw} & \boldsymbol{0}_{pc} \\ \boldsymbol{0}_{wp} & \boldsymbol{R}_{ww} & \boldsymbol{0}_{wc} \\ \boldsymbol{0}_{cp} & \boldsymbol{0}_{cw} & \boldsymbol{R}_{cc} \end{pmatrix} \cdot \begin{pmatrix} \boldsymbol{x}_p \\ \boldsymbol{x}_w \\ \boldsymbol{x}_c \end{pmatrix} \tag{2.86}$$

has to be closed with the weak form of the linearised MHD equations (2.34)

$$\lambda \begin{pmatrix} \boldsymbol{B}_{ll} & \boldsymbol{B}_{ld} \\ \boldsymbol{B}_{dl} & \boldsymbol{B}_{dd} \end{pmatrix} \begin{pmatrix} \boldsymbol{x}_l \\ \boldsymbol{x}_d \end{pmatrix} = \begin{pmatrix} \boldsymbol{A}_{ll} & \boldsymbol{A}_{ld} & \boldsymbol{0}_{lp} & \boldsymbol{0}_{lw} & \boldsymbol{0}_{lc} \\ \boldsymbol{A}_{dl} & \boldsymbol{A}_{dd} & \boldsymbol{R}_{dp} & \boldsymbol{R}_{dw} & \boldsymbol{R}_{dc} \end{pmatrix} \begin{pmatrix} \boldsymbol{x}_l \\ \boldsymbol{x}_d \\ \boldsymbol{x}_p \\ \boldsymbol{x}_w \\ \boldsymbol{x}_c \end{pmatrix}. \tag{2.87}$$

Again, the indices l and d name plasma interior and boundary related elements, respectively. The matrices $\boldsymbol{R}_{dp}$, $\boldsymbol{R}_{dw}$ and $\boldsymbol{R}_{dc}$ are obtained by inserting the definition of the magnetic field perturbation (2.85) into the boundary terms (2.48)–(2.53). Combining (2.86) and (2.87) yields the extended eigenvalue problem,

$$\begin{aligned}\lambda \begin{pmatrix} \boldsymbol{B}_{ll} & \boldsymbol{B}_{ld} & \boldsymbol{0}_{lp} & \boldsymbol{0}_{lw} & \boldsymbol{0}_{lc} \\ \boldsymbol{B}_{dl} & \boldsymbol{B}_{dd} & \boldsymbol{0}_{dp} & \boldsymbol{0}_{dw} & \boldsymbol{0}_{dc} \\ \boldsymbol{0}_{pl} & -\boldsymbol{R}_{pd} & \boldsymbol{M}_{pp} & \boldsymbol{M}_{pw} & \boldsymbol{M}_{pc} \\ \boldsymbol{0}_{wl} & \boldsymbol{0}_{wd} & \boldsymbol{M}_{wp} & \boldsymbol{M}_{ww} & \boldsymbol{M}_{wc} \\ \boldsymbol{0}_{cl} & \boldsymbol{0}_{cd} & \boldsymbol{M}_{cp} & \boldsymbol{M}_{cw} & \boldsymbol{M}_{cc} \end{pmatrix} \begin{pmatrix} \boldsymbol{x}_l \\ \boldsymbol{x}_d \\ \boldsymbol{x}_p \\ \boldsymbol{x}_w \\ \boldsymbol{x}_c \end{pmatrix} \\ = \begin{pmatrix} \boldsymbol{A}_{ll} & \boldsymbol{A}_{ld} & \boldsymbol{0}_{lp} & \boldsymbol{0}_{lw} & \boldsymbol{0}_{lc} \\ \boldsymbol{A}_{dl} & \boldsymbol{A}_{dd} & \boldsymbol{R}_{dp} & \boldsymbol{R}_{dw} & \boldsymbol{R}_{dc} \\ \boldsymbol{0}_{pl} & \boldsymbol{0}_{pd} & \boldsymbol{0}_{pp} & \boldsymbol{0}_{pw} & \boldsymbol{0}_{pc} \\ \boldsymbol{0}_{wl} & \boldsymbol{0}_{wd} & \boldsymbol{0}_{wp} & -\boldsymbol{R}_{ww} & \boldsymbol{0}_{wc} \\ \boldsymbol{0}_{cl} & \boldsymbol{0}_{cd} & \boldsymbol{0}_{cp} & \boldsymbol{0}_{cw} & -\boldsymbol{R}_{cc} \end{pmatrix} \begin{pmatrix} \boldsymbol{x}_l \\ \boldsymbol{x}_d \\ \boldsymbol{x}_p \\ \boldsymbol{x}_w \\ \boldsymbol{x}_c \end{pmatrix}\end{aligned} \tag{2.88}$$

https://doi.org/10.1017/S0022377826102153 Published online by Cambridge University Press

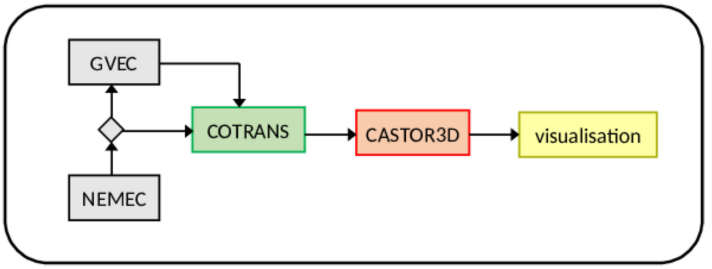


FIGURE 5. The CASTOR3D code and its connections to other codes.

or in abbreviated form

$$\lambda \boldsymbol{B}^{ext}\boldsymbol{x}^{ext} = \boldsymbol{A}^{ext}\boldsymbol{x}^{ext}. \tag{2.89}$$

The capability to solve this extended eigenvalue problem makes the CASTOR3D code a very flexible and powerful numerical tool for linear stability studies of tokamak and stellarator equilibria. A concise description of CASTOR3D will be given in the following section.

3. The CASTOR3D code

The CASTOR3D code is not a stand-alone code. Besides input provided by the user (e.g. numerical parameters, physical quantities and profiles, wall and coil data, etc.), it needs a highly accurate equilibrium input in a special form provided by the COTRANS code. Figure 5 shows the CASTOR3D code and its connections to other codes.

The equilibrium codes NEMEC (NESTOR + VMEC) (Hirshman & Whitson 1983; Hirshman, van Rij & Merkel 1986) and GVEC (Galerkin variational equilibrium code) (Hindenlang *et al*. 2025*a*,*b*) are usually used to compute the ideal plasma equilibrium which serves as input to the COTRANS code. The GVEC code (Hindenlang *et al*. 2025*a*) is a 3-D MHD equilibrium solver that follows the same idea as VMEC (Hirshman & Whitson 1983), that is, finding a set of nested flux surfaces via energy minimisation. A distinct feature of GVEC is its radial discretisation with B-splines, thus providing a smooth high-order representation of the equilibrium solution including the region around the magnetic axis. GVEC yields equilibria with a high numerical accuracy required for a precise stability analysis and is able to accurately transform the equilibrium solutions directly into Boozer coordinates.

The COTRANS code, which is described in more detail in Appendix B, transforms, if necessary, the equilibrium into the desired flux coordinates (NEMEC (Hirshman & Whitson 1983; Hirshman *et al*. 1986), Boozer (Boozer 1982) or 2-D straight field line coordinates (Kerner, Jakoby & Lerbinger 1986; Huysmans *et al*. 1993)) and computes all necessary equilibrium quantities in a Fourier representation suitable for CASTOR3D. That is, the choice of the flux coordinate type is made in the COTRANS code, whereas CASTOR3D uses a general formulation of the flux coordinates.

The best choice of the coordinate type depends on the considered equilibrium and the mode type which shall be investigated. While 2-D straight field line coordinates are restricted to axisymmetric plasma configurations, NEMEC and Boozer coordinates can also be used for 3-D equilibria. In the case of NEMEC or 2-D straight field line coordinates, the s- and u-coordinates are orthogonal to the v-coordinate which is

https://doi.org/10.1017/S0022377826102153 Published online by Cambridge University Press

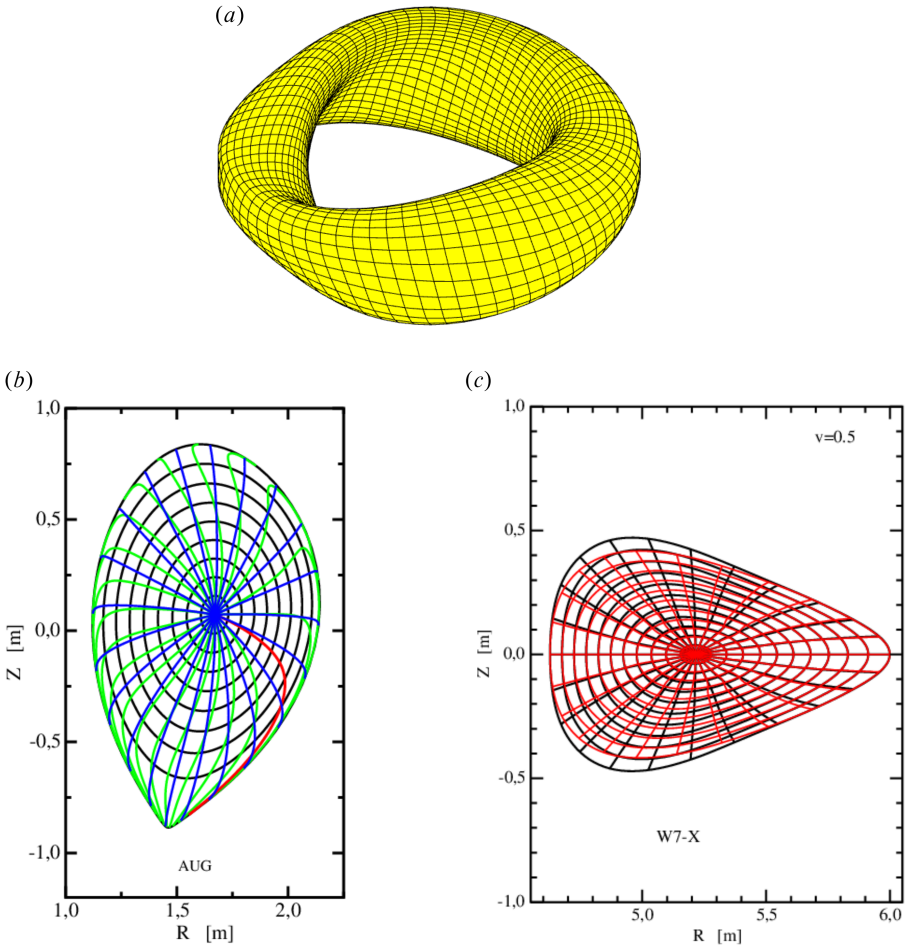


FIGURE 6. Cylindrical (R, φ, Z) and magnetic flux coordinates (s, v, u). (a) The u- and v-coordinate lines in Boozer coordinates on the last flux surface $(s = 1)$ of a QA equilibrium (from Strumberger (2025); licensed under a Creative Commons Attribution licence (CC BY)). (b,c) Toroidal cross-sections for a constant v-coordinate. The flux surfaces and poloidal coordinate lines are illustrated for (b) an AUG equilibrium (blue, NEMEC coordinates; green and red, 2-D straight field line coordinates) and (c) a W7-X equilibrium (black, NEMEC coordinates; red, Boozer coordinates). In (b) and (c) the flux surfaces are equidistant in $\sqrt{\Phi_0/\Phi_0^{tot}}$ with Φ_0 being the toroidal flux and Φ_0^{tot} being its total value.

proportional to φ with $\varphi = ((2\pi)/N_{per})v$ and N_{per} being the number of periods of the equilibrium. The Boozer coordinates, however, are completely non-orthogonal with non-planar $v = \text{const.}$ planes as illustrated by the u, v-grid shown in figure 6(a). Thus, in the case of 3-D equilibria, the NEMEC and Boozer flux surface contour lines differ from each other for a given v-coordinate (see figure 6c). Axisymmetric tokamak equilibria are usually bounded by a separatrix with an upper or lower X-point while, in presence of MP fields, magnetic island chains appear on resonant surfaces. The overlap of neighbouring island chains results in a stochastic region with chaotic field line behaviour (Frerichs *et al*. 2026). Neither a separatrix nor a stochastic region can be represented by Fourier series. Therefore, the equilibrium calculations have to

https://doi.org/10.1017/S0022377826102153 Published online by Cambridge University Press

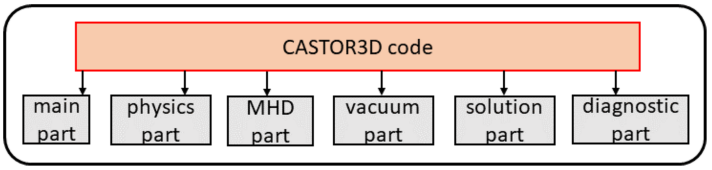


FIGURE 7. The CASTOR3D code structure.

be limited to a closed flux surface located very close, but inside the separatrix or the stochastic boundary region. Usually, in the case of an axisymmetric tokamak equilibrium, a flux surface with normalised poloidal flux $\Psi_{norm} \geqslant 0.999$ is chosen. In the case of 3-D tokamak or stellarator equilibria, free-boundary equilibrium calculations are performed using a total toroidal flux that corresponds to the plasma boundary inside the stochastic region (for details see Strumberger (1997)). Nevertheless, tokamak equilibria have a large safety factor q at this newly defined plasma boundary, which in the case of 2-D straight field line or Boozer coordinates causes a very strong bending of the poloidal coordinate lines in direction of the X-Point location. Figure 6(*b*)[13] illustrates this bending for a typical AUG equilibrium. Because of the usually very flat and low-valued q-profiles, this problem does not arise in stellarators as shown in figure 6(*c*). Here, the u-coordinate lines are almost straight in Boozer coordinates. Especially, Boozer and 2-D straight field line coordinates are advantageous for the description of high-n^*[14] peeling–ballooning modes because NEMEC coordinates would afford too many Fourier harmonics for the description of those localised modes. In the case of low-n^* modes, however, NEMEC coordinates may be the better choice.

The CASTOR3D code is able to produce a variety of output quantities (e.g. growth rate, oscillation frequency, eigenfunctions, perturbed quantities, etc.) which can be visualised by Xmgrace, Python and MATLAB plot software.

Figure 7 shows the six parts of the CASTOR3D code. They are described in more detail in the following subsections.

3.1. *Main part*

The main part of the CASTOR3D code fulfils control tasks, reads the input, writes parts of the output and organises the data exchange between the code parts.

3.2. *Physics part*

The profiles of pressure $p_0(s)$, poloidal current $J_0(s)$, toroidal current $I_0(s)$, poloidal flux $\Psi_0(s)$, toroidal flux $\Phi_0(s)$, rotational transform $\iota_0(s)$ and their derivatives are part of the equilibrium input provided by the COTRANS code. Physical quantities and profiles, such as density, resistivity, etc., either have to be provided by the CASTOR3D user input or are computed with the CASTOR3D code.

3.2.1. Density and temperature profiles

Providing a density profile $n_0(s)$, the temperature profile is obtained from $T_0 = p_0/n_0$. As described in § 2.1.1, we introduced the parameter α_T which allows a more realistic ratio of ion $T_i = \alpha_T T$ and electron temperature $T_e = (1 - \alpha_T)T$.

[13]The AUG equilibrium is cropped at a normalised poloidal flux of $\Psi_{norm} = 0.9995$. The q-value of this flux surface amounts to $q = 7$.

[14]Here n^* is the dominant toroidal harmonic (see § 3.6).

https://doi.org/10.1017/S0022377826102153 Published online by Cambridge University Press

3.2.2. Plasma resistivity

Besides user defined resistivity profiles $\eta_0(s)$, it is also possible to choose between Spitzer (Wesson 1997), Sauter (Sauter *et al*. 1999, 2002) and Redl (Redl *et al*. 2021) resistivity in CASTOR3D. The neoclassical resistivity derived by Sauter *et al*. takes effects due to trapped particles as well as impurities into account. An improved expression for this neoclassical resistivity is given by the resistivity of Redl, which is much more accurate in the high collisionality regime.

3.2.3. Heat conductivity coefficients

We follow Chen, Xu & Lei (2019) in order to determine expressions for the heat conductivity coefficients of the parallel heat flux (2.15). The well-known classical Spitzer–Härm (superscript *SH*) expressions (Spitzer & Härm 1953; Braginskii 1965) for the parallel thermal conductivity coefficients are rigorous in the short-mean-free-path (collisional) regime and assume that the lowest-order particle distribution function is a Maxwellian,

$$\kappa_{\|e}^{SH} = 3.2 n_e v_{th,e}^2 \tau_e, \qquad \kappa_{\|i}^{SH} = 3.9 n_i v_{th,i}^2 \tau_i \tag{3.1}$$

with thermal velocities $v_{th,j} = (T_j/m_j)^{1/2}$ and collision times τ_j $(j = e, i)$. This approximation breaks down and can greatly overestimate the parallel heat flux when the mean-free-path is long compared with the temperature gradient scale length. In a collisionless tokamak plasma, typically, the upper limit to the parallel heat flux is of the order of the free streaming (superscript *FS*) flux

$$\boldsymbol{q}_{\|j}^{FS} \simeq -\kappa_{\|j}^{FS} \boldsymbol{\nabla}_\| T_j \quad \text{with} \quad \kappa_{\|j}^{FS} \simeq n_j v_{th,j} q R_0. \tag{3.2}$$

Here, q is the local safety factor and R_0 the major radius.

In CASTOR3D, the user can choose between Spitzer–Härm expressions, free streaming expressions and combinations of both for the ion and electron thermal conductivities[15] (Chen *et al*. 2019):

$$\kappa_{\|j} = \min\left(\kappa_{\|j}^{FS}, \kappa_{\|j}^{SH}\right) \quad \text{or} \quad \kappa_{\|j} = \left(\frac{1}{\kappa_{\|j}^{FS}} + \frac{1}{\kappa_{\|j}^{SH}}\right)^{-1}. \tag{3.3}$$

3.2.4. Parallel dynamic viscosity coefficient

The parallel dynamic viscosity coefficient $\mu_\|$ (2.7) has to be provided by the user. Rough estimates of $\mu_\|$ are

$$\mu_\| = \begin{cases} 0.96 \dfrac{v_{th,i}^2}{\nu_i} \rho_i & \text{for } \nu_i > k_\| v_{th,i} \\ \kappa_\| \dfrac{v_{th,i}}{k_\|} \rho_i & \text{for } \nu_i < k_\| v_{th,i} \end{cases} \tag{3.4}$$

for a collisional (Braginskii 1965) and a collisionless plasma (Waltz 1988), respectively. The latter expression is used to model the ion Landau damping effect. In (3.4), ν_i is the ion collision frequency, $k_\|$ denotes the parallel wave vector with $k_\| \sim 1/R_0$, ρ_i is the ion mass density and $\kappa_\|$ is a strength parameter (Chu *et al*. 1995).

[15] Here, the parallel heat conductivity, which has been implemented in CASTOR3D quite recently, is only mentioned for completeness. Stability studies taking heat conductivity into account are planned for the future.

https://doi.org/10.1017/S0022377826102153 Published online by Cambridge University Press

3.2.5. Ion diamagnetic drift velocity

Boozer magnetic flux coordinates (s, v, u) (Boozer 1982) have the advantage that in these coordinates the poloidal and toroidal contravariant components of the diamagnetic drift velocity are constant on flux surfaces (Strumberger *et al*. 2023). It is

$$\begin{aligned}\boldsymbol{V}^*_{i0} &= \frac{m_i}{e}\frac{1}{\rho_0}\frac{\boldsymbol{B}_0\times\nabla p_{i0}}{B_0^2} = V^{v*}_{i0}\boldsymbol{r}_{,v} + V^{u*}_{i0}\boldsymbol{r}_{,u}\\ &= \frac{m_i}{e}\frac{1}{\rho_0}\frac{\partial p_{i0}}{\partial s}\left(\frac{I_0}{\Phi_0' J_0+\Psi_0' I_0}\boldsymbol{r}_{,v} - \frac{J_0}{\Phi_0' J_0+\Psi_0' I_0}\boldsymbol{r}_{,u}\right) = \frac{1}{2\pi}\Omega^{i*}_{tor}\boldsymbol{r}_{,v} + \frac{1}{2\pi}\Omega^{i*}_{pol}\boldsymbol{r}_{,u}\end{aligned} \tag{3.5}$$

with the toroidal and poloidal frequencies

$$\Omega^{i*}_{tor}(s) = 2\pi\frac{m_i}{e}\frac{1}{\rho_0}\frac{\partial p_{i0}}{\partial s}\frac{I_0}{\Phi_0' J_0+\Psi_0' I_0} \text{ and } \Omega^{i*}_{pol}(s) = -2\pi\frac{m_i}{e}\frac{1}{\rho_0}\frac{\partial p_{i0}}{\partial s}\frac{J_0}{\Phi_0' J_0+\Psi_0' I_0}. \tag{3.6}$$

Here, Φ_0' and Ψ_0' are the derivatives of the toroidal $\Phi_0(s)$ and poloidal $\Psi_0(s)$ fluxes.

3.2.6. The ExB-velocity

Excluding radial flows which would be generated by non-radial components of the electric field $\boldsymbol{E}_0$, we assume that the electric potential Φ_E is constant on flux surfaces, that is,

$$\boldsymbol{E}_0 = -\frac{\partial\Phi_E}{\partial s}\nabla s = E_s\nabla s \tag{3.7}$$

with E_s being the radial covariant component. Then, analogous to the ion diamagnetic drift velocity (3.5), the ExB-velocity can be expressed in Boozer coordinates by (Strumberger *et al*. 2025)

$$\boldsymbol{V}_{ExB} = \frac{\boldsymbol{B}_0\times\nabla\Phi_E(s)}{B_0^2} = \frac{1}{2\pi}\Omega^{ExB}_{tor}(s)\boldsymbol{r}_{,v} + \frac{1}{2\pi}\Omega^{ExB}_{pol}(s)\boldsymbol{r}_{,u}. \tag{3.8}$$

Assuming $T_{i0}\approx T_{e0}$ and $\hat{\nu}_i/\sqrt{m_i}\approx\hat{\nu}_e/\sqrt{m_e}$ with $\hat{\nu}_i$ and $\hat{\nu}_e$ being the ion and electron collision frequencies normalised to the corresponding particle masses with $m_i \gg m_e$, the well-known ambipolarity condition (Stroth, Manz & Ramisch 2011; Viezzer 2012) simplifies to

$$E_s \approx \frac{m_i}{e}\frac{1}{\rho_0}\frac{\partial p_{i0}}{\partial s}. \tag{3.9}$$

In this case, the ion diamagnetic drift velocity is balanced by the ExB-velocity.

3.2.7. External velocity $\boldsymbol{V}^{ext}$

The general formulation of the velocity

$$\begin{aligned}\boldsymbol{V}^{ext} = &\frac{1}{2\pi}\Omega_{tor}(s)f_{vv}(s,v,u)\boldsymbol{r}_{,v} + \frac{1}{2\pi}\Omega_{pol}(s)f_{vu}(s,v,u)\boldsymbol{r}_{,v}\\ &+ \frac{1}{2\pi}\Omega_{tor}(s)f_{uv}(s,v,u)\boldsymbol{r}_{,u} + \frac{1}{2\pi}\Omega_{pol}(s)f_{uu}(s,v,u)\boldsymbol{r}_{,u}\end{aligned} \tag{3.10}$$

https://doi.org/10.1017/S0022377826102153 Published online by Cambridge University Press

was added to the ion velocity (2.6) because it allows us to express a given velocity in different kinds of flux coordinates.

Using Boozer coordinates, the ion drift velocity (3.5) and/or the ExB-velocity (3.8) can also be expressed in the $\boldsymbol{V}^{ext}$-formulation (3.10) with $f_{vv} = f_{uu} = 1$ and $f_{vu} = f_{uv} = 0$. This possibility allows to test CASTOR3D with respect to code errors concerning the implementation of these velocities.

Driven, for example, by neutral beam injection, tokamak plasmas can quickly rotate in toroidal direction. Using NEMEC or 2-D straight field line coordinates, $\boldsymbol{V}^{ext}$ simply reads

$$\boldsymbol{V}^{ext} = \frac{1}{2\pi}\Omega_{tor}(s)\boldsymbol{r}_{,v}. \tag{3.11}$$

However, if Boozer coordinates are used for a 3-D tokamak equilibrium, this velocity has to be described by toroidal and poloidal components ($f_{vv} \neq 0$ and $f_{uv} \neq 0$) because $\boldsymbol{r}_{,v}$ in Boozer coordinates is not parallel to $\boldsymbol{r}_{,v}$ in NEMEC or 2-D straight field line coordinates. The transformation of the velocity into Boozer coordinates is performed with the COTRANS code.

Analogous to tokamaks, the plasma of a QA stellarator enjoys 'intrinsic ambipolarity' and is free to rotate in the direction of symmetry (Helander & Simakov 2008), which corresponds to the toroidal direction (v-direction) in Boozer coordinates. So, using Boozer coordinates, the externally driven flow can be expressed by (3.10).

3.2.8. Normalisation

The CASTOR3D code needs its input and yields its output in SI units. However, the solution of the eigenvalue problem is performed in normalised quantities. Thus, in the physics part, all input quantities are normalised to radius R_a, magnetic field strength B_a and density ρ_a at the magnetic axis.

3.3. *The MHD part*

The elements of the matrices $\boldsymbol{A}$ and $\boldsymbol{B}$ describing the plasma part of the eigenvalue problem (see § 2.3) are computed in the MHD part of CASTOR3D. For details see Appendix A.

3.4. *Vacuum part*

The elements of the matrices $\boldsymbol{M}_{\rm pp}, \boldsymbol{M}_{\rm pw}, \ldots, \boldsymbol{M}_{\rm cc}$ and $\boldsymbol{R}_{\rm pd}, \boldsymbol{R}_{\rm dp}, \boldsymbol{R}_{\rm dw}, \boldsymbol{R}_{\rm dc}, \boldsymbol{R}_{\rm ww}, \boldsymbol{R}_{\rm cc}$ are computed in the vacuum part. Besides, the vacuum magnetic field perturbation is computed as function of unit perturbations if a free-boundary eigenvalue problem is solved without taking resistive wall structures into account (see § 2.3.2).

3.5. *Solution part*

The various types of general, complex, non-Hermitian, large spars eigenvalue problems described in § (2.3) are solved with the MPI-parallelised Krylov–Schur solver of the SLEPc (scalable library for eigenvalue problem computations) public library (Roman *et al*. 2025). The latter is built on top of the PETSc (portable, extensible toolkit for scientific computation) library (Balay *et al*. 2026).

The matrix structure of the extended eigenvalue problem (2.89) is illustrated in figure 8(*a*). The block-tridiagonal structure of the plasma part results from the local basis of the Hermite polynomials (see Appendix A.1) which couples only neighbouring radial grid points j. In the case of a fixed-boundary eigenvalue problem (2.77) or

https://doi.org/10.1017/S0022377826102153 Published online by Cambridge University Press

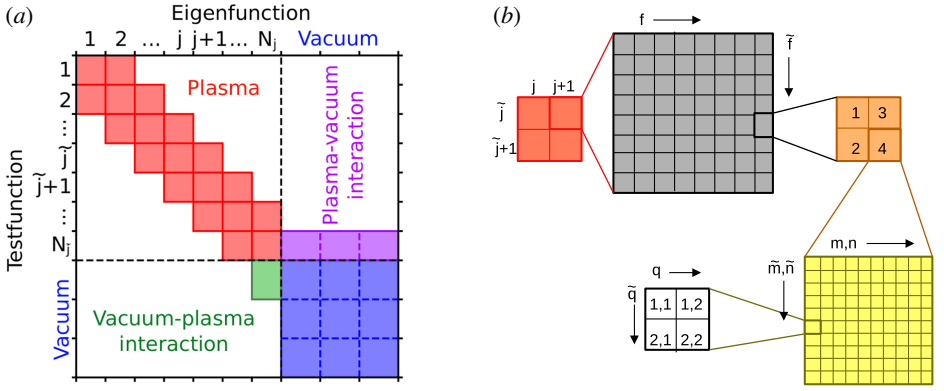


FIGURE 8. (*a*) Structure of the matrices $\boldsymbol{A}^{ext}$ and $\boldsymbol{B}^{ext}$, respectively. The colours indicate the block-tridiagonal plasma part (red), the vacuum part (blue), the plasma–vacuum interaction (purple, only in matrix $\boldsymbol{A}^{ext}$) and the vacuum–plasma interaction (green, only in matrix $\boldsymbol{B}^{ext}$) (figure reproduced from Puchmayr (2023)). (*b*) Substructure of a block of the plasma part. The grey 8×8 submatrix represents the perturbed quantities with $f, \tilde{f} = \hat{\rho}, \hat{v}^s, \hat{v}^u, \hat{v}^v, \hat{T}, \hat{A}_s, \hat{A}_u, \hat{A}_v$. The orange 2×2 submatrix results from the two orthogonal parts of the ansatz for the perturbed quantities and the two test functions. The poloidal and toroidal Fourier harmonics yield the yellow $N_{mn} \times N_{mn}$ submatrix and, finally, the white 2×2 submatrix results from the two Hermite polynomials at each grid point ($q, \tilde{q} = 1, 2$).

a free-boundary eigenvalue problem where the boundary elements of matrix $\boldsymbol{A}$ are expressed as functions of unit perturbations of the vacuum (see § 2.3.2), the matrices $\boldsymbol{A}^{ext}$ and $\boldsymbol{B}^{ext}$ reduce to the block-tridiagonal plasma part. Then, the remaining matrix $\boldsymbol{B}$ is self-adjoint and positive definite, but $\boldsymbol{A}$ is always non-symmetric (Kerner *et al*. 1998). The matrix $\boldsymbol{B}^{ext}$ of the extended eigenvalue problem (2.89), however, is non-symmetric because of the submatrix $\boldsymbol{R}_{\rm pd}$ which describes the vacuum–plasma interaction (green block in figure 8*a*). Especially, in the case of 3-D equilibria and/or the presence of multiply connected wall structures represented by a vast amount of triangles, the dimensions of the $\boldsymbol{A}^{ext}$ and $\boldsymbol{B}^{ext}$ matrices can become huge.

Considering N_j radial grid point, $N_f = 8$ perturbed quantities, N_n toroidal harmonics, N_m^n poloidal harmonics for a given n and $N_q = 2$ orthogonal Hermite polynomials, the dimensions of the plasma part matrices $\boldsymbol{A}$ and $\boldsymbol{B}$ amount to $N = 2N_j N_f N_{mn} N_q$ with $N_{mn} = \sum_n N_m^n$. Here, the factor 2 represents the two sub-blocks arising due to the two orthogonal parts of $\hat{w}_f$ (2.30) and the two types of test functions ((2.36) and (2.37)), respectively. They are necessary to describe the two orthogonal solutions with possibly different eigenvalues of a 3-D eigenvalue problem. The memory required for the factorisation of a generally non-Hermitian matrix roughly scales with the number of non-zero matrix elements (Puchmayr 2023):

$$\text{Memory} \sim N_j (N_{mn})^2. \tag{3.12}$$

Fortunately, depending on the mode type which shall be investigated, the substructure of the plasma part illustrated in figure 8(*b*) offers various possibilities to reduce the matrix size.

Puchmayr *et al*. (2023) and Strumberger *et al*. (2025) showed that the solution of the full large eigenvalue problem is only needed for modes where the $c_{f,j,q}^{m,n}$ and $\check{c}_{f,j,q}^{m,n}$ parts (2.30) are strongly coupled and the eigenvalues of the two corresponding

https://doi.org/10.1017/S0022377826102153 Published online by Cambridge University Press

solutions are different. Since the coupling between the two parts decreases with increasing n, the ansatz $\hat{w}_f$ (2.30) and the components of z^* ((2.36) and (2.37)) can be reduced to

$$\hat{w}_f(s, v, u) = \sum_{m,n,j,q} c^{m,n}_{f,j,q} h^j_{f,q}(s) \mathrm{e}^{2\pi \mathrm{i}(mu+nv)} = \hat{w}_{f,\mathrm{c}}(s, v, u) \tag{3.13}$$

and

$$\hat{z}^{*\mathrm{s},\tilde{m},\tilde{n}}_{\tilde{f},\tilde{j},\tilde{q}}(s, v, u) = \hat{t}_{\tilde{f}} h^{\tilde{j}}_{\tilde{f},\tilde{q}}(s) \frac{1}{2\mathrm{i}} \left(\mathrm{e}^{2\pi \mathrm{i}(\tilde{m}u+\tilde{n}v)} - \mathrm{e}^{-2\pi \mathrm{i}(\tilde{m}u+\tilde{n}v)} \right) \tag{3.14}$$

for instabilities to which only higher n-harmonics contribute. Then, in figure 8(a) the orange submatrix reduces to block 1, that is, the matrix dimension N of the plasma part reduces by a factor of two. We call the large eigenvalue problem a 'full' and the smaller one a 'reduced' eigenvalue problem. In the case of stellarator-symmetric equilibria[16] the Fourier representations of the R, φ, Z-coordinates and the perturbed quantities subdivide into two groups with either even or odd parity (Schwab 1993). The ideal CAS3D code (Nührenberg 1996; Nührenberg 2016) is able to exploit the stellarator symmetry and to separate the eigenvalue problem into sine- and cosine-type solutions. Yet, in the case of non-stellarator symmetric equilibria, it always has to take both types into account while the reduced eigenvalue problem of the CASTOR3D code works for axisymmetric equilibria and high-n^* instabilities of 3-D equilibria with and without stellarator symmetry. Usually, idealised tokamak plasmas are axisymmetric, but not up–down symmetric and hence not stellarator symmetric.

In 2-D straight field line coordinates or Boozer coordinates, the Fourier harmonics of high-n ballooning modes are strongly radially localised and peaked at their resonant surfaces. Figure 9(a) shows the harmonics of the radial displacement for an $n = 40$ ballooning mode of an axisymmetric tokamak equilibrium. It illustrates the high radial resolution and the large number of poloidal harmonics needed for the stability calculation. Using a non-equidistant radial grid with high resolution at the location of the mode and a rough grid in regions without or little mode activity reduces the number of radial grid points N_j and hence the matrix dimension of the plasma part. Furthermore, if the mode is located in the plasma centre or close to the plasma boundary, it is possible to crop the boundary or the core region of the radial grid, respectively, in order to reduce the matrix size (Puchmayr 2023).

Using 2-D straight field line or Boozer coordinates, instabilities consist mainly of harmonics which are close to the resonant harmonic

$$m_{res}(s) = nq(s). \tag{3.15}$$

Thus, for a given toroidal harmonic n, a natural choice for the poloidal harmonic spectrum at a certain radial location s is given by

$$m_{res}(s) - \Delta m \leqslant m(s) \leqslant m_{res}(s) + \Delta m \tag{3.16}$$

[16]Considering cylindrical coordinates, stellarator-symmetric equilibria posses some up–down symmetric toroidal planes (e.g. at $\varphi_{ud} = 0, (\pi/N_{per}), (2\pi/N_{per})$, etc. with N_{per} being the number of periods). Then, for example, the magnetic field components at coordinate point $P = (R, \varphi, Z)$ are related to the stellarator-symmetric point $P' = (R, -\varphi, -Z)$ by $B_R(P) = -B_R(P')$, $B_\varphi(P) = B_\varphi(P')$ and $B_Z(P) = B_Z(P')$. It has to be noted that non-up–down symmetric axisymmetric equilibria are not stellarator-symmetric.

https://doi.org/10.1017/S0022377826102153 Published online by Cambridge University Press

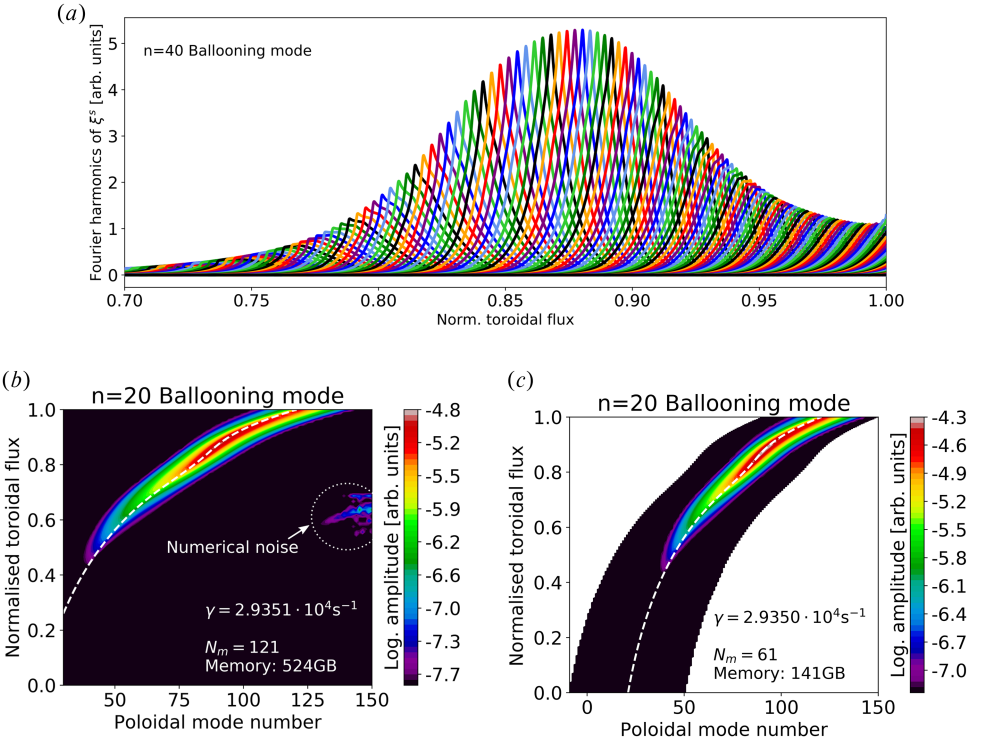


FIGURE 9. (*a*) Fourier harmonics of the radial displacement for an $n = 40$ ballooning mode in straight field line coordinates. Various colours are used in order to improve the visibility of the individual harmonics. (*b,c*) Logarithmic amplitude of the Fourier harmonics for an $n = 20$ ballooning mode calculated with (*b*) the constant and (*c*) the s-dependent spectrum of poloidal harmonics. In the latter only harmonics in the filled (non-white) area are used for the ansatz (2.30). The dashed white lines indicate the resonant poloidal harmonics. (Figures reproduced from Puchmayr (2023).)

where the range of poloidal mode numbers Δm takes the coupling of the poloidal harmonics into account. Instead of using a constant m-range for a given toroidal harmonic, the s-dependent m-range can strongly reduce the number of Fourier harmonics as shown for a $n = 20$ ballooning mode in figures 9(*b*) and 9(*c*). There, the results obtained with a constant and a s-dependent m-range are compared. While Fourier decompositions and growth rates are the same, only half the poloidal harmonics and a quarter of the memory are required with the optimised Fourier spectrum. In addition, the optimised version omits numerical noise by excluding harmonics that should have vanishing contribution to the Fourier decomposition (see figure 9*b*).

Finally, a possible periodicity of 3-D tokamak and stellarator equilibria reduces the number of toroidal harmonics that have to be taken into account. As explained in detail in Nührenberg (1996), the symmetry connected with the N_{per} periods of an equilibrium implies the existence of $1 + [N_{per}/2]$ independent mode families. For example, the fivefold symmetry of W7-X implies the existence of three mode families:

mode family 0, $n = 0, 5, 10, 15, 20, 25, \ldots$;
mode family 1, $n = 1, 4, 6, 9, 11, 14, \ldots$;
mode family 2, $n = 2, 3, 7, 8, 12, 13, \ldots$.

https://doi.org/10.1017/S0022377826102153 Published online by Cambridge University Press

Since only the toroidal harmonics of a mode family yield non-vanishing coupling terms, the stability properties of each mode family can be separately investigated (e.g. see Strumberger *et al*. 2020).

The discussed methods which reduce the size of the eigenvalue problem decrease not only the required amount of memory but also the computational time. The time varies between seconds and several hours depending on the problem size.

3.6. *Diagnostic part*

The solution of an eigenvalue problem yields one or several eigenvalues λ (2.17) and the corresponding eigenfunctions which consist of the plasma part (2.35) and various vacuum parts (2.74)–(2.76). In order to determine the mode type, we concentrate on the plasma part.

3.6.1. Determination of the mode type

Multiplying the components of the eigenvector (2.35) with the associated Hermite polynomials, we obtain the Fourier spectra

$$\hat{w}^{m,n}_{f,c}(s) = \sum_{j,q} c^{m,n}_{f,j,q} h^{j}_{f,q}(s) \quad \text{and} \quad \hat{w}^{m,n}_{f,\check{c}}(s) = \sum_{j,q} \check{c}^{m,n}_{f,j,q} h^{j}_{f,q}(s) \tag{3.17}$$

of the perturbations. These spectra reveal important information about location and structure of a mode. Usually, we consider the real and/or imaginary parts of the radial velocity perturbation vicariously for all perturbed quantities, that is, $\mathrm{Re}(\hat{v}^{s}_{m,n}(s)) = \mathrm{Re}(\hat{w}^{m,n}_{\hat{v}^{s},c}(s))$, $\mathrm{Im}(\hat{v}^{s}_{m,n}(s)) = \mathrm{Im}(\hat{w}^{m,n}_{\hat{v}^{s},c}(s))$, $\mathrm{Re}(\hat{\tilde{v}}^{s}_{m,n}(s)) = \mathrm{Re}(\hat{w}^{m,n}_{v^{s},\check{c}}(s))$ and $\mathrm{Im}(\hat{\tilde{v}}^{s}_{m,n}(s)) = \mathrm{Im}(\hat{w}^{m,n}_{v^{s},\check{c}}(s))$. While in the case of axisymmetric configurations the modes can be easily characterised by their toroidal mode number n, several n-harmonics couple together in 3-D plasmas. Therefore, we introduced the dominant toroidal harmonic n^{*} to name the modes (Strumberger & Günter 2019). In order to determine n^{*}, we compute the following four functions:

$$f_{\mathrm{Re}}(n) = \sum_{m} \int \left(\mathrm{Re}\left(\hat{v}^{s}_{m,n}(s)\right)\right)^{2} \mathrm{d}s, \qquad \tilde{f}_{\mathrm{Re}}(n) = \sum_{m} \int \left(\mathrm{Re}\left(\hat{\tilde{v}}^{s}_{m,n}(s)\right)\right)^{2} \mathrm{d}s, \tag{3.18}$$

$$f_{\mathrm{Im}}(n) = \sum_{m} \int \left(\mathrm{Im}\left(\hat{v}^{s}_{m,n}(s)\right)\right)^{2} \mathrm{d}s, \qquad \tilde{f}_{\mathrm{Im}}(n) = \sum_{m} \int \left(\mathrm{Im}\left(\hat{\tilde{v}}^{s}_{m,n}(s)\right)\right)^{2} \mathrm{d}s \tag{3.19}$$

and look for their maxima.

Figure 10(*a*) shows the Fourier spectrum of the radial velocity perturbation of an external kink mode of a QA equilibrium with a parallel viscosity of $\mu_{\parallel} = 3$ kg ms^{-1}. Since, both, the $n = 1$ (green) and $n = 5$ (blue) harmonics contribute strongly to the mode, n^{*} cannot be determined from this figure. In figure 10(*b*), however, the functions (3.17) indicate that $n = 1$ is the dominant harmonic in the case of $\mu_{\parallel} = 3$ kg ms^{-1}. Since, it is $\hat{v}^{s}_{m,n}(s) = \hat{\tilde{v}}^{s}_{m,n}(s)$ in figure 10(*a*), this $n^{*} = 1$ mode is a cosine-type mode, while sine-type modes are characterised by $\hat{v}^{s}_{m,n}(s) = -\hat{\tilde{v}}^{s}_{m,n}(s)$ (see figure 26).

Besides the Fourier spectra, the diagnostic part of the CASTOR3D code also yields the mode structure in real space (e.g. see figures 12*c* and 12*d*, 15*b*–*d* and 17*a* and 17*b*).

https://doi.org/10.1017/S0022377826102153 Published online by Cambridge University Press

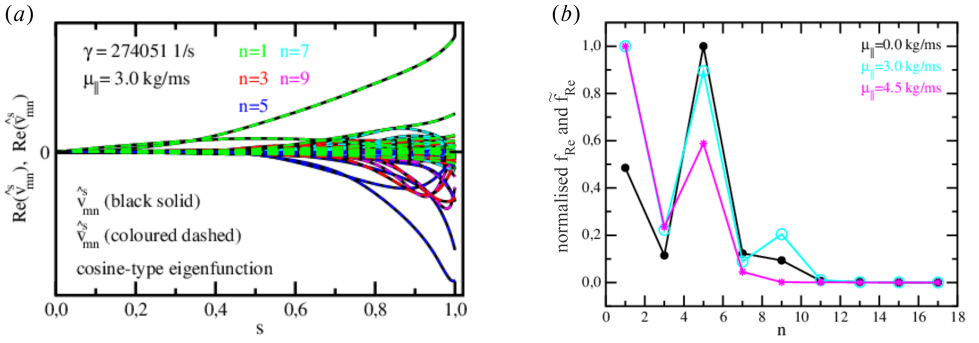


FIGURE 10. Cosine-type external kink modes of a QA equilibrium. (*a*) Real parts of the eigenfunction Fourier spectrum for the radial velocity perturbation of the $n^* = 1$ mode. (*b*) Contributions of the toroidal Fourier harmonics (f_{Re} (solid lines), $\tilde{f}_{\mathrm{Re}}$ (symbols)) to the cosine-type mode for various values of the parallel viscosity coefficient $\mu_\parallel$ (from Strumberger *et al.* (2025); licensed under a Creative Commons Attribution licence (CC BY)).

3.6.2. Analysis of the energetic drives of the modes

The energy functional of ideal MHD was extended to the regime of finite resistivity and transformed into an intuitive form (Puchmayr *et al.* 2022) that separates pressure-gradient drive, current-density drive and stabilising phenomena analogously to the ideal version of the functional derived by Greene and Johnson (Greene & Johnson 1968). The resulting resistive energy functional is not in the form of a solvable eigenvalue problem, but is intended to analyse the energetic composition of eigenfunctions which were calculated in advance by solving the MHD eigenvalue problem (2.34) or the extended eigenvalue problem (2.89). The functional was decomposed into energy contributions related to the physical mechanisms which drive or stabilise the instabilities. The decomposition is based on the linearised resistive MHD equations, excluding equilibrium flows and any extended MHD effects,

$$\rho_0\lambda^2\boldsymbol{\xi} = \nabla(\boldsymbol{\xi}\cdot\nabla p_0) + \nabla(p_0\Gamma(\nabla\cdot\boldsymbol{\xi})) + \frac{1}{\mu_0}(\nabla\times\boldsymbol{B}_0)\times\boldsymbol{B}_1 + \frac{1}{\mu_0}(\nabla\times\boldsymbol{B}_1)\times\boldsymbol{B}_0, \tag{3.20}$$

$$\boldsymbol{B}_1 = \nabla\times(\boldsymbol{\xi}\times\boldsymbol{B}_0) - \lambda^{-1}\nabla\times\left(\frac{\eta}{\mu_0}\nabla\times\boldsymbol{B}_1\right), \tag{3.21}$$

where $\boldsymbol{\xi} = \lambda^{-1}\boldsymbol{v}_1$ is the displacement. The initial form of the resulting energetic decomposition is similar to the energy functional of Bernstein *et al.* (1958),

$$-\lambda^2\int \rho_0|\boldsymbol{\xi}|^2\mathrm{dV} = 2\delta W = 2\delta W_V + 2\delta W_B \tag{3.22}$$

with the volume energy contributions δW_V and boundary contributions δW_B. The left-hand side of (3.22) is related to the kinetic energy of the instability, while the right-hand side $2\delta W = 2\delta W_V + 2\delta W_B$ describes the change of the potential energy caused by the perturbation of the equilibrium.

The derivation of the intuitive form of the resistive energy functional is described in detail in Puchmayr *et al.* (2022). Here, we only present the intuitive form of the

https://doi.org/10.1017/S0022377826102153 Published online by Cambridge University Press

volume energy contribution. It reads for resistive MHD,

$$
\begin{aligned}
2\delta W_V = & \underbrace{\int \frac{|\boldsymbol{B}_{1,\perp}|^2}{\mu_0}\mathrm{d}V}_{\delta W_{\mathrm{SHA}}} + \underbrace{\int \frac{\boldsymbol{B}_0^2}{\mu_0}\left|\nabla\cdot\boldsymbol{\xi}_\perp + 2(\boldsymbol{\xi}_\perp\cdot\boldsymbol{\kappa}) + \frac{1}{B_0^2}\boldsymbol{B}_0\cdot\boldsymbol{B}_R\right|^2\mathrm{d}V}_{\delta W_{\mathrm{CPA}}} \\
& + \underbrace{\Gamma\int p_0|\nabla\cdot\boldsymbol{\xi}|^2\mathrm{d}V}_{\delta W_{\mathrm{SND}}} + \underbrace{\frac{1}{\mu_0^2\lambda^*}\int \eta|\nabla\times\boldsymbol{B}_1|^2\mathrm{d}V}_{\delta W_{\mathrm{RCD}}} - \underbrace{\int \frac{j_{0,\parallel}}{|\boldsymbol{B}_0|}(\boldsymbol{\xi}_\perp^*\times\boldsymbol{B}_0)\cdot\boldsymbol{B}_{1,\perp}\mathrm{d}V}_{\delta W_{\mathrm{CUR}}} \\
& - \underbrace{\int 2(\boldsymbol{\xi}_\perp\cdot\nabla p_0)(\boldsymbol{\xi}_\perp^*\cdot\boldsymbol{\kappa})\mathrm{d}V}_{\delta W_{\mathrm{DP}}} - \underbrace{\int \frac{1}{B_0^2}(\boldsymbol{\xi}_\parallel^*\times\nabla p_0)\cdot(\boldsymbol{B}_0\times\boldsymbol{B}_R)\mathrm{d}V}_{\delta W_{\mathrm{RD},\parallel}} \\
& - \underbrace{\int \frac{1}{B_0^2}(\boldsymbol{\xi}_\perp\cdot\nabla p_0)(\boldsymbol{B}_0\cdot\boldsymbol{B}_R^*)\mathrm{d}V}_{\delta W_{\mathrm{RD},\perp}}
\end{aligned}
\tag{3.23}
$$

with the self-induced ohmic field $\boldsymbol{B}_R = \lambda^{-1}\nabla\times(\eta\boldsymbol{j}_1)$ and the equilibrium curvature vector $\boldsymbol{\kappa} = (\boldsymbol{b}\cdot\nabla)\boldsymbol{b}$ with $\boldsymbol{b} = \boldsymbol{B}_0/|\boldsymbol{B}_0|$. There are four stabilising contributions to the volume energy which are related to perpendicular magnetic perturbations (shear Alfvén waves) δW_{SHA}, parallel magnetocompressional perturbations (compressional Alfvén waves) δW_{CPA}, adiabatic compression (sound waves) δW_{SND} and resistive current diffusion δW_{RCD}. The destabilising terms are the parallel current-density drive δW_{CUR}, the field-line-curvature-dependent pressure-gradient δW_{DP} drive and two resistive corrections to the pressure-gradient drive. The latter two account for the effect of resistive diffusion on the work done by the induced magnetic perturbation that is generated by parallel $\delta W_{RD,\parallel}$ and perpendicular $\delta W_{RD,\perp}$ compression of the plasma, respectively. It should be noted that the resistive correction to the relation between perpendicular compression and its induced magnetic perturbation also appears in the stabilising energy of magnetocompressional perturbations δW_{CPA}. In order to obtain energetic contributions which are independent of the arbitrary linear amplitude of the perturbation, it is natural to normalise the energy terms by

$$
\delta W_{\mathrm{norm}} \equiv \int \rho_0|\boldsymbol{\xi}|^2\mathrm{d}V. \tag{3.24}
$$

Concerning the boundary contributions δW_B, it should be mentioned that no additional surface or vacuum energy contributions have to be considered in the case of finite resistivity.

The terms of the resistive energy functional were implemented in the CASTOR3D code. The energetic decomposition contributes to the physical understanding of the perturbations (see § 4.3) and allows to distinguish current-density and pressure-gradient driven instabilities (see § 4.1.2).

4. Stability studies

In the following, we give an overview of CASTOR3D stability studies performed for various 2-D and 3-D test equilibria as well as AUG and W7-X discharges.

https://doi.org/10.1017/S0022377826102153 Published online by Cambridge University Press

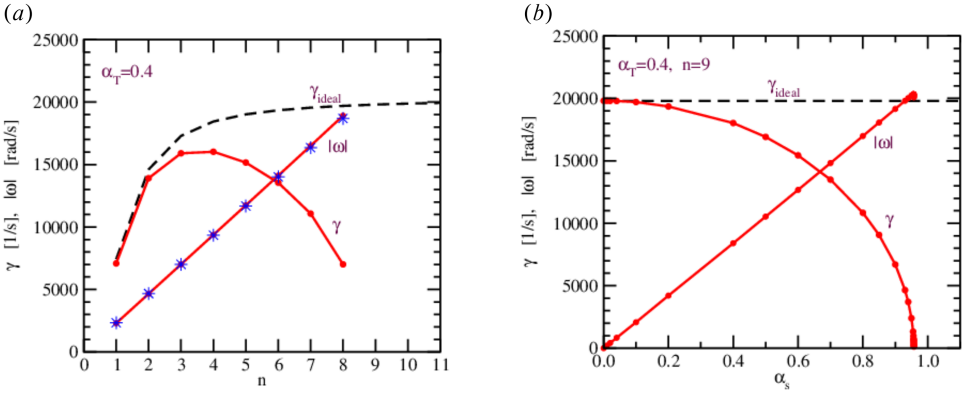


FIGURE 11. Growth rate γ and absolute value of the oscillation frequency $|\omega|$ as function of (a) the toroidal mode number n and (b) the scaling parameter α_s (see § 2.1.1). The black dashed line represents the ideal growth rate γ_{ideal} obtained without taking the diamagnetic drift effects into account. (a) The blue stars mark the absolute value of half of the ion diamagnetic drift frequency $|\omega_i^*|/2$ (4.2). (From Strumberger *et al*. (2023); licensed under a Creative Commons Attribution licence (CC BY).)

4.1. *Internal kink and interchange modes*

Using the CASTOR3D code, stability studies taking diamagnetic drift effects into account were performed for 2-D and 3-D test equilibria with circular cross-section, aspect ratio $A = 1.6$, pressure profile $p(s) = p_a(1 - 2s^2 + s^4)$, slightly monotonously increasing safety factor profile $q(s)$ (magnetic axis, $q_a = 0.99$; plasma boundary, $q_b = 1.59$) (Strumberger *et al*. 2023) and equilibrium flow velocity $\boldsymbol{V}_0 = 0$, that is, it was assumed that the contributions to the ion velocity (2.6) were either zero or cancelled. The square root of the normalised toroidal flux served as radial coordinate s. These equilibria were unstable with respect to low- and medium-n internal kink and interchange modes.

4.1.1. Ideal modes

The considered axisymmetric, high-β equilibrium (volume averaged plasma beta: $\langle\beta\rangle = 2.97$ %) was ideal unstable. Figure 11 illustrates the strong stabilising impact and the oscillation frequency mainly caused by the gyroviscosity. Because of the high plasma-β, the contribution of the electron diamagnetic drift effect was negligibly small as shown in Strumberger *et al*. (2023). We used $\alpha_T = 0.4$, that is, $p_i = 0.4p$ and $p_e = 0.6p$. In good agreement with the results of the MINERVA-DI code and the dispersion relation

$$\gamma + \mathrm{i}\omega = \mathrm{i}\frac{|\omega_i^*|}{2} \pm \sqrt{\gamma_{ideal}^2 - \left(\frac{\omega_i^*}{2}\right)^2} \tag{4.1}$$

presented by Aiba (2016), the modes became stabilised when the absolute value of the oscillation frequency $|\omega|$ of the mode exceeded the ideal growth rate, $|\omega| \gtrapprox \gamma_{ideal}$. The modes were stable for $n > 8$ as shown in figure 11. In the case of simple equilibria where mainly one poloidal harmonic m and one toroidal harmonic n contribute to the Fourier spectrum of the mode, the ion diamagnetic drift frequency $\omega_i^* = \boldsymbol{V}_i^* \cdot \boldsymbol{k}$ ($\boldsymbol{k}$ = wave number vector) can be approximated by $\boldsymbol{k} = -\mathrm{i}((\nabla f)/f)$ with function

https://doi.org/10.1017/S0022377826102153 Published online by Cambridge University Press

$f = f_0(s)\exp(2\pi \mathrm{i}(mu - nv))$. The latter describes the perturbation caused by the leading (m, n)-Fourier harmonic. Expressing $\boldsymbol{V}_i^*$ in Boozer coordinates (3.5), we obtained

$$\omega_i^*(s) = 2\pi(\mathrm{m}V_i^{*u} - \mathrm{n}V_i^{*v}) \tag{4.2}$$

for the ion diamagnetic drift frequency. In figure 11(*a*) the blue stars mark $(|\omega_i^*|/2)$ calculated with the analytic expression (4.2) at the rational $q = 1$ flux surface. These values agree very well with the oscillation frequencies resulting from the solutions of the eigenvalue problem.

Besides the axisymmetric equilibrium, we also investigated, for the first time, diamagnetic drift effects in an equivalent one-periodic, 3-D equilibrium with helical core (Strumberger *et al*. 2023). This equilibrium was the result of a 3-D fixed-boundary NEMEC equilibrium calculation using an axisymmetric, circular plasma boundary (Strumberger & Günter 2017). Neglecting the pressure terms in Ohm's law (2.16), the results obtained for ideal kink and interchange modes confirmed the growing stabilising diamagnetic drift effect with increasing toroidal mode number (which is the dominant toroidal harmonic n^*). Furthermore, the oscillation frequencies of the modes corresponded in good approximation to $(\omega_i^*/2)$. However, additionally to these similarities with the axisymmetric equilibrium, 3-D specific effects were found: sufficiently strong diamagnetic drift effects are needed (i) to cause a degeneration of otherwise non-degenerate growth rates and (ii) to let the mode oscillate (see also § 4.3). (iii) Diamagnetic drift effects change the mode structure as shown in figure 12. The figure illustrates the changes of the composition of the Fourier spectrum and the mode location for the $n^* = 6$ mode. Here, we only show the radial velocity perturbation of the cosine-type function because the sine-type function yielded no new information. The components related with the complex and complex conjugate e-functions (3.17) of the Fourier series are equal (figure 12*a*) without diamagnetic drift effects. However, including diamagnetic drift effects, either the complex or complex conjugate components strongly dominate the Fourier spectrum (figure 12*b*). Here, it should be mentioned that not only drift effects lead to such a decoupling, but any kind of plasma flow (Puchmayr *et al*. 2023; Strumberger *et al*. 2025). Furthermore, besides the reduction of the growth rate and the decoupling of the the complex and complex conjugate parts, the number of contributing toroidal harmonics is reduced. This leads to a more uniformly distributed mode structure in the real space as shown in figures 12(*c*) and 12(*d*). Here, the coupling of the poloidal harmonics played only a minor role for the mode structure because of the very flat q-profile and the circular plasma boundary.

4.1.2. Resistive modes

In order to study the diamagnetic effects on resistive modes, the same axisymmetric plasma configuration was used as for the ideal modes, but with a much lower plasma-β of $\langle\beta\rangle = 0.97\,\%$ (Strumberger *et al*. 2023). This equilibrium was unstable with respect to internal resistive modes located at the $q = 1$ flux surface. Their slow growth rates approximately scaled with $\eta^{1/3}$ which is typical for resistive kink and interchange modes. The analysis of the resistive energy functional (§ 3.6.2) prevailed the pressure-gradient driven character of these modes. Figure 13(*a*) shows the relative current-density drive $\delta W_{CUR}/(\delta W_{CUR} + \delta W_{DP})$ as function of the toroidal mode number. It adds up to 3.5 % for $n = 1$ and $\eta = 1 \times 10^{-7}$ Ωm and strongly decreases with increasing n. Although the relative current-density drive is nearly independent

https://doi.org/10.1017/S0022377826102153 Published online by Cambridge University Press

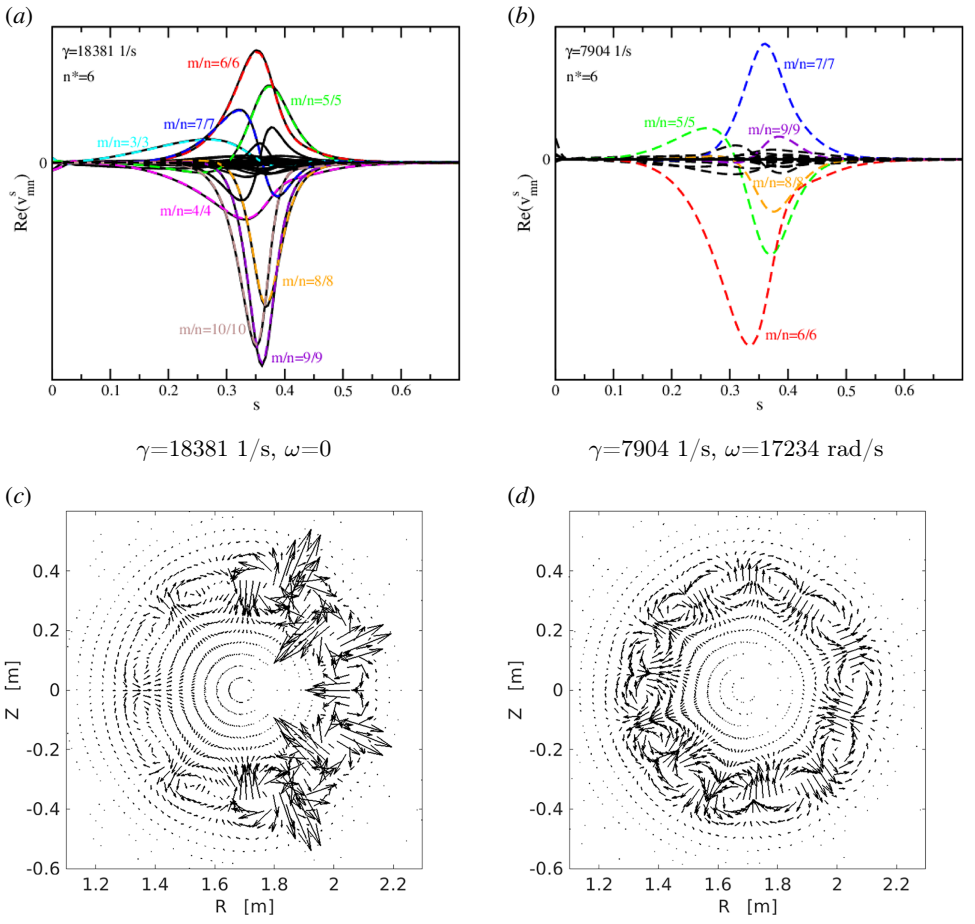


FIGURE 12. (*a,b*) Fourier spectra of the real part of the radial velocity perturbation, and (*c,d*) mode structures of the $n^* = 6$ mode (*a,c*) without and (*b,d*) with ion diamagnetic drift effect. In (*a*) and (*b*), the solid and dashed lines denote the Fourier spectra of the radial velocity perturbation related with the complex and complex conjugate e-functions. The largest contributions are marked by their poloidal and toroidal harmonics m/n. In (*c*) and (*d*), the vectors characterise the velocity perturbation in the R–Z-plane at toroidal angle $\varphi = 0^{\mathrm{o}}$ and time $t = 0$. (From Strumberger *et al.* (2023); licensed under a Creative Commons Attribution licence (CC BY).)

of the resistivity, the perturbation and the corresponding energy densities are broadened with increasing resistivity (see figures 13*b* and 13*d*). For increasing mode numbers, however, the modes become more and more localised at the $\iota = 1$ flux surface (see figure 13*d*). While the integrated current-density drive δW_{CUR} (3.23) remains small because of the cancellation of stabilising and destabilising contributions in different radial regions of the plasma (see figures 13*c* and 13*d*), the pressure-gradient drive δW_{DP} (3.23) strongly grows with increasing n.

Figures 14(*a*) and 14(*b*) show the growth rates and oscillation frequencies as functions of the parameter α_T for various n-modes. They include the limiting cases of cold ions ($\alpha_T = 0$) and cold electrons ($\alpha_T = 1$). In the case of cold ions, only the electron diamagnetic drift remains that is described by the parallel electron pressure-gradient term in the extended Ohm's law (2.16), while, in the case of cold electrons,

https://doi.org/10.1017/S0022377826102153 Published online by Cambridge University Press

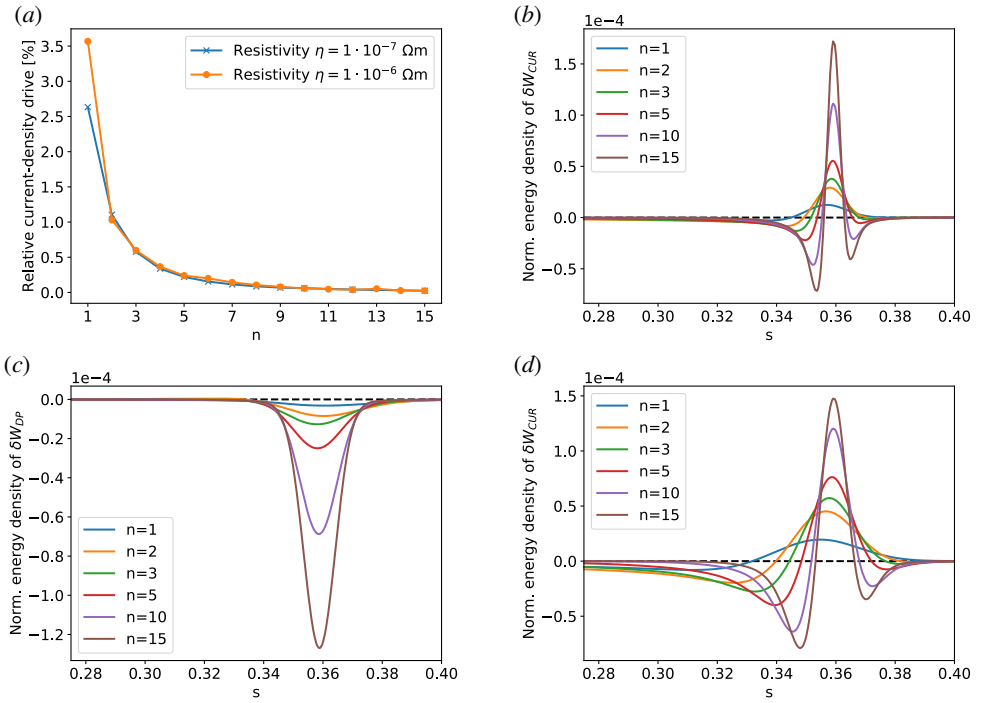


FIGURE 13. Energetic decomposition of the resistive internal perturbations of the considered low-β equilibrium: (*a*) relative current-density drive as function of the toroidal mode number for resistivities of $\eta = 10^{-7}$ Ωm (blue) and $\eta = 10^{-6}$ Ωm (orange). Normalised energy densities corresponding to (*b,d*) the current-density and (*c*) the pressure-gradient drives as functions of the square root of the normalised toroidal flux for resistivities of (*b*) $\eta = 10^{-7}$ Ωm and (*c,d*) $\eta = 10^{-6}$ Ωm. (From Strumberger *et al*. (2023); licensed under a Creative Commons Attribution licence (CC BY).)

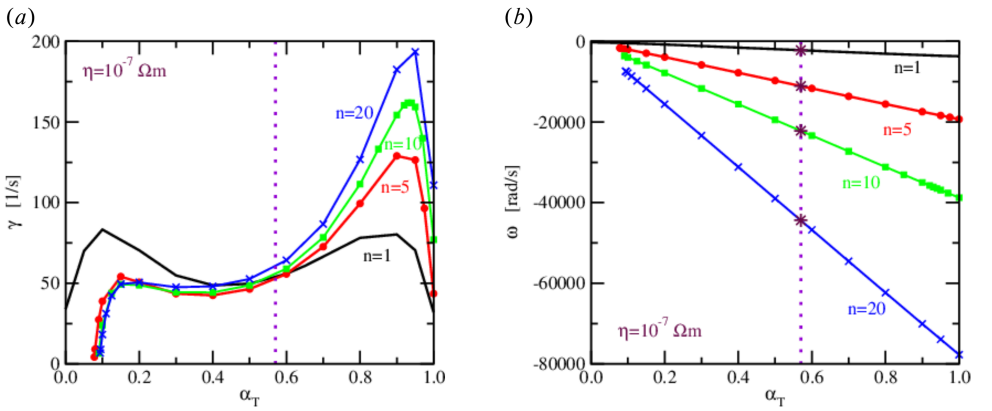


FIGURE 14. (*a*) Growth rates and (*b*) oscillation frequencies as functions of parameter α_T for various n-harmonics. The dotted vertical lines mark the α_T-values for which the considered resistivity value corresponds to the approximated Spitzer resistivity. The stars denote ω_i^*. (From Strumberger *et al*. (2023); licensed under a Creative Commons Attribution licence (CC BY).)

https://doi.org/10.1017/S0022377826102153 Published online by Cambridge University Press

only the ion diamagnetic drift influences the stability via the gyroviscosity term in the momentum equation (2.9) and the ion pressure-gradient term in (2.16). All combinations of ion and electron diamagnetic drift effects have a large stabilising effect (Strumberger *et al*. 2023).

The oscillation frequencies of the resistive modes scale linearly with α_T as shown in figure 14(*b*). Computing the ion diamagnetic drift frequency (4.2) for the toroidal mode numbers and a chosen α_T-parameter (indicated by the dotted lines in the figures 14*a* and 14*b*), it turned out that these frequencies agree very well with the oscillation frequencies resulting from the solution of the eigenvalue problem, that is, $\omega \approx \omega_i^*$. In the case of ideal modes, however, it is $\omega \approx \omega_i^*/2$ as shown in § 4.1.1.

4.2. *Double tearing and internal resistive kink modes*

Strumberger *et al*. (2020), we presented linear stability studies of DTMs and resistive internal kink modes for a set of W7-X type stellarator equilibria with electron cyclotron current drive. The external cocurrent drive led to an increase of the rotational transform $\iota = 1/q$ and the formation of one or two $\iota = 1$ rational flux surfaces (Wolf *et al*. 2017). Using the CASTOR3D code, we studied the dependence of the growth rates on the plasma resistivity, the parallel viscosity and the shape of the rotational transform profile.

Using a modified Spitzer profile for the plasma resistivity with $\eta_a = 1 \times 10^{-7}$ Ωm[17] and taking no parallel viscosity into account, we computed the growth rates of $n^* = 1, 2, \ldots, 8$ DTMs as function of the radial distance Δs of the two $\iota = 1$ rational flux surfaces. As shown in figure 15(*a*), the n^*-type of the most unstable mode decreases with growing distance between the $\iota = 1$ flux surfaces. While the $n^* = 6$ DTM is the most unstable mode for $\Delta s = 0.078$, the $n^* = 1$ mode is most unstable for $\Delta s \geqslant 0.17$. The latter is also the most unstable mode in the case of equilibria with only one $\iota = 1$ flux surface. Figure 15(*b–d*) illustrate the gradual change from an asymmetric coupled $n^* = 1$ DTM[18] with a small internal kink contribution to a resistive internal kink mode. In the case of figure 15(*d*), a rotational transform profile with only one $\iota = 1$ surface was used.

There is experimental evidence that $n^* = 1$ perturbations are involved in the observed sawtooth-like oscillations followed by a thermal quench in W7-X (Zanini *et al*. 2020). The CASTOR3D code is a linear code and, therefore, cannot describe sawtooth oscillations. But, it describes the 3-D geometry of Wendelstein 7-X correctly, and it showed that the $n^* = 1$ resistive kink mode is the most unstable mode in the case of either a large distance between the $\iota = 1$ flux surfaces, or a single $\iota = 1$ surface. Further insight into the relationship between resistive kink mode stability and electron temperature crashes was obtained from performing nonlinear resistive stability studies with the TM1 code, which assumes axisymmetric, high aspect ratio equilibria with cylindrical cross-section (Yu *et al*. 2020). There, fast crashes of the electron temperature were found. Depending on the distance between the two $\iota = 1$ surfaces and the maximum ι-value, full and partial crashes were observed. In agreement with the experimental observation, the internal kink mode led to a fast radial displacement of the hot core and a full crash of the temperature in approximately

[17]At the magnetic axis, the resistivity would amount to $\eta_a \approx 1 - 5 \times 10^{-9}$ Ωm for electron temperatures of 3–7 keV (Wolf *et al*. 2017). Since such small resistivity values result in mode structures below the gyroradius scale (Strumberger *et al*. 2020), we used $\eta_a \gtrsim 10^{-8}$ Ωm.

[18]Strumberger *et al*. (2020); we called the symmetric-coupled DTM type A DTM and the asymmetric-coupled one type B DTM.

https://doi.org/10.1017/S0022377826102153 Published online by Cambridge University Press

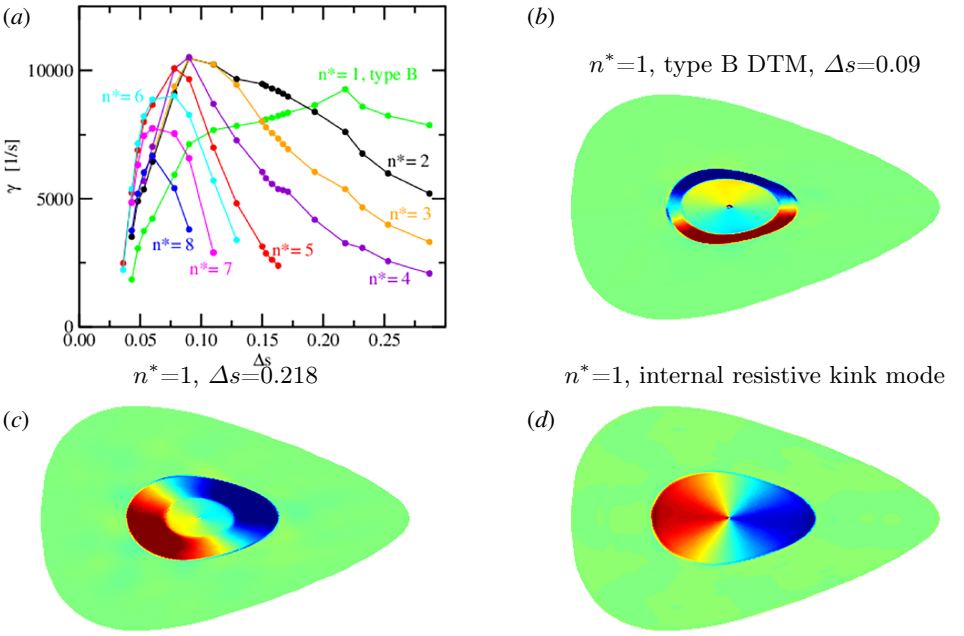


FIGURE 15. (*a*) Growth rates of the $n^* = 1, 2, \ldots, 8$ DTMs as function of Δs. (*b–d*) Structures of $n^* = 1$ mode types for various ι-profiles represented by the radial velocity perturbation (blue = inward to red = outward shift) at the triangular cross-section of W7-X. (All figures reproduced with permission from Nucl. Fusion vol. 60, 2020, p. 106013 and EUROfusion. Copyright EURATOM 2020.)

20–30 μs if the distance between the $\iota = 1$ surfaces was large enough. For smaller distances, partial crashes of the central temperature were found. That is, the hot core only temporally moved outwards. In summary, the experimental observations together with the numerical results obtained for 3-D linear stability studies and two-fluid, resistive, nonlinear computations assuming a simplified geometry support the picture of low-n^* resistive modes causing sawtooth oscillations followed by a thermal crash.

Wang *et al*. (2025) also applied their stellarator version of the nonlinear CLT code, called CLT-fx, to a W7-X equilibrium with electron cyclotron current drive and two $\iota = 1$ surfaces. They determined the growth rate of the linear phase as function of the plasma resistivity and compared their results with 'the $\eta^{1/3}$-scaling of the internal kink mode' obtained with the CASTOR3D code in Strumberger *et al*. (2020). First of all, no such scaling for an internal kink mode was given in Strumberger *et al*. (2020) because the growth rates obtained for the $n^* = 1$ single resistive internal kink mode did not fit in good approximation the 1/3-scaling in the considered resistivity range (see figure 10*b* in Strumberger *et al*. (2020)). However, we found a 1/3-scaling for the asymmetric-coupled $n^* = 1$ DTM. In contrast to the latter, Wang *et al*. did not obtain the $\eta^{1/3}$ DTM scaling, but observed a very weak dependence of the linear growth rate on the resistivity that became negative for the highest considered resistivity values. In order to explain their result, they argued: 'We think this is mainly due to the strong mutual interaction between the inner and outer kink modes, which leads to that the linear growth rate weakly depend on the resistivity'. The point of the matter is that the CLT-fx and CASTOR3D computations were performed

https://doi.org/10.1017/S0022377826102153 Published online by Cambridge University Press

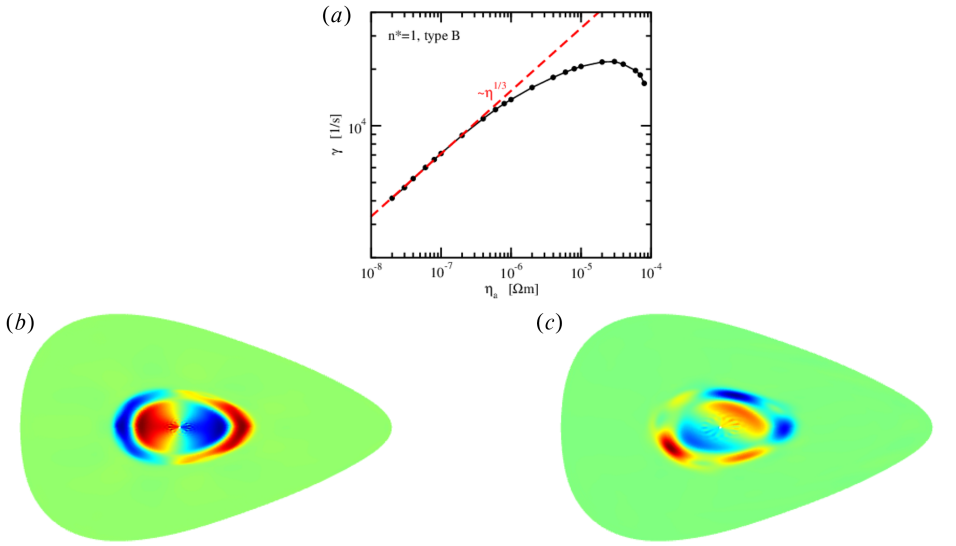


FIGURE 16. (*a*) Growth rate of the asymmetric-coupled $n^* = 1$ DTM (type B mode) as function of the resistivity η_a (this figure contains data published in Strumberger *et al*. (2020) with permission of Nucl. Fusion vol. 60, 2020, p. 106013 and EUROfusion; copyright EURATOM 2020). Structures of asymmetric-coupled $n^* = 1$ DTMs for (*b*) $\eta_a = 6 \times 10^{-6}$ Ωm and (*c*) $\eta_a = 6 \times 10^{-5}$ Ωm represented by the radial velocity perturbation (blue = inward to red = outward shift) at a triangular cross-section of W7-X.

for different rotational transform profiles and completely different ranges of the plasma resistivity. They used a resistivity range of $1 \times 10^{-6} \leqslant \eta \leqslant 1 \times 10^{-4}$ Ωm, while the CASTOR3D calculations were performed for $1 \times 10^{-8} \leqslant \eta \leqslant 1 \times 10^{-6}$ Ωm. The latter exhibited the DTM scaling only in the range of $2 \times 10^{-8} < \eta \lesssim 2 \times 10^{-7}$ Ωm. In figure 16(*a*), we increased the resistivity further to the CLT-fx-range and obtained for these unrealistically high resistivity values (Zhou, Aleynikova & Ferraro 2023) the same behaviour as Wang *et al*. namely, the growth rate flattens and, eventually, decreases. Moreover, the corresponding mode structures presented for $\eta = 1 \times 10^{-7}$ Ωm (figure 15*b*), 6×10^{-6} Ωm (figure 16*b*) and 6×10^{-5} Ωm (figure 16*c*) support the explanation of Wang *et al*., that we cited earlier. In the case of low resistivity ($\eta_a = 1 \times 10^{-7}$ Ωm), the mode structure corresponds to an $n^* = 1$ DTM with small internal kink contribution. With increasing resistivity the contribution of the internal kink increases and the growth rate flattens. Finally, the growth rate decreases while the $n^* = 1$ structure of the mode decays.

4.3. *Locked modes*

The eigenfunctions of an axisymmetric plasma are proportional to a single toroidal harmonic, so that the multiplication of an eigenfunction by an arbitrary complex prefactor results in an equivalent eigenfunction corresponding to the same eigenvalue as the original eigenfunction. That is, the growth rate is independent of the solution phase that corresponds to a shift of the perturbation in toroidal direction. This implies that there exists no preferred mode position and the mode (e.g. a tearing mode) can rotate freely and uniformly with the plasma in toroidal direction. However, it has been observed that in the presence of static external error fields the

https://doi.org/10.1017/S0022377826102153 Published online by Cambridge University Press

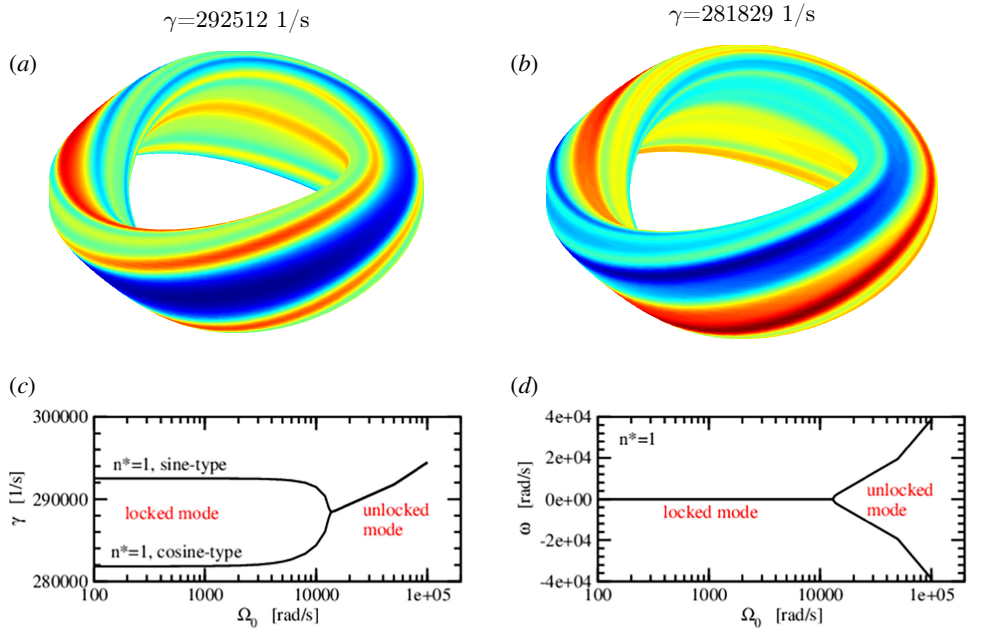


FIGURE 17. (*a*) Sine- and (*b*) cosine-type $n^* = 1$ mode locations represented by the radial velocity perturbation (blue = inward to red = outward shift) on the plasma boundary of a QA equilibrium. (*c*) Growth rates and (*d*) oscillation frequencies of the modes as functions of the externally driven toroidal flow frequency at the magnetic axis. (Reproduced with permission from Nucl. Fusion vol. 59, 2019, p. 106008 and EUROfusion. Copyright EURATOM 2019. In (*c*) and (*d*) only the data of the $n^* = 1$ mode are reprinted.)

mode rotation becomes non-uniform and its rotation frequency is reduced. The rotation even stops completely and the mode becomes locked if the MP field is strong enough (Nave & Wesson 1990; Hender *et al*. 1992; La Haye *et al*. 1992).

In 3-D tokamak or stellarator equilibria, plasma modes can be locked to specific locations because of the 3-D plasma geometry that leads to the coupling of several toroidal harmonics. As already explained in § 2.1.3, the solution of a 3-D linear stability eigenvalue problem yields two orthogonal eigenvalues that may be different. Investigating an ideal external kink unstable, QA equilibrium, two slightly different eigenvalues were found for the low-n^* external kink modes (Strumberger & Günter 2019). Figures 17(*a*) and 17(*b*) show the two possible locations of the $n^* = 1$ external kink mode. The two mode locations correspond to slightly different growth rates. Driving a toroidal flow in symmetry direction[19] of the QA configuration showed that in the case of a mode with non-degenerate eigenvalues a minimum plasma rotation frequency, the so-called threshold frequency Ω_{thres}, is required to unlock these modes. Figures 17(*c*) and 17(*d*) illustrate the two $n^* = 1$ growth rates and oscillations frequencies as functions of the toroidal rotation frequency[20] of the plasma. Below $\Omega_0 \leqslant \Omega_{\text{thres}} \approx 13\,600$ rad s^{-1} the two growth rates are different and the modes are locked. Then, the two growth rates meet and the mode starts to oscillate for $\Omega_0 > \Omega_{\text{thres}}$. If such a strictly locked mode[21] is forced to rotate with the plasma, its

[19]The symmetry direction of a QA equilibrium corresponds to the toroidal direction in Boozer coordinates.
[20]Strumberger & Günter (2019); we used the toroidal rotation profile $\Omega(s) = \Omega_0(1 - 0.7s^2)$.
[21]For the definition of strictly looked modes see in the following, and Puchmayr *et al*. (2023).

https://doi.org/10.1017/S0022377826102153 Published online by Cambridge University Press

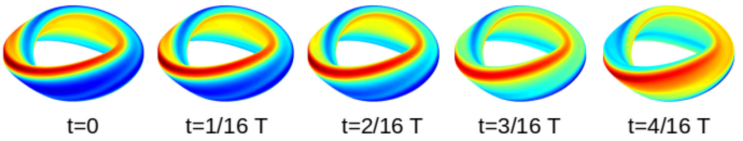


FIGURE 18. Oscillation of the $n^* = 1$ mode with $\omega < 0$ represented by the location of the radial velocity perturbation (blue = inward to red = outward shift). Shown are five equidistant time steps within 1/4 oscillation cycle. (Modified reproduction with permission from Nucl. Fusion vol. 59, 2019, p. 106008 and EUROfusion. Copyright EURATOM 2019.)

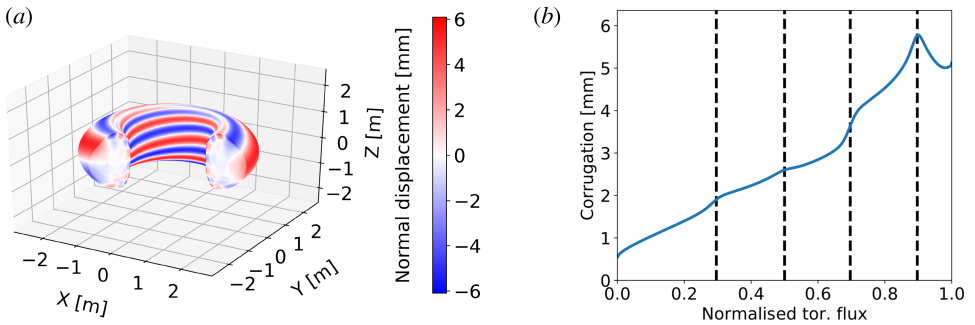


FIGURE 19. (*a*) Corrugation (normal displacement) of the 3-D equilibrium for the numerical test case. (*b*) Maximum values of the corrugation on every flux surface as a function of the normalised toroidal flux s. The dashed lines mark the resonant flux surfaces with respect to the $N_{per} = 2$ MP field. (From Puchmayr *et al*. (2023); licensed under a Creative Commons Attribution 4.0 licence (CC BY).)

rotation is non-uniform. Figure 18 illustrates such a non-uniform rotation for the $n^* = 1$ mode with negative oscillation frequency. Here, the mode structure changes most between $t = 3/16T$ and $t = 4/16T$ with T being the oscillation period. It should be mentioned that the solution with positive oscillation frequency describes the identical non-uniform rotation, but with a phase shift in the oscillation cycle (see figure 16 in Strumberger & Günter (2019)). Besides, in Strumberger & Günter (2019), we showed that each mode type has its individual threshold frequency that is correlated to the difference of the non-degenerated growth rates $\Delta\gamma$ obtained in the case of a non-rotating plasma. The larger $\Delta\gamma$, the higher Ω_{thres}. With increasing n^*, the two growth rates degenerate ($\Delta\gamma = 0$) and Ω_{thres} becomes zero. That is, high-n^* modes oscillate for any toroidal rotation frequency. The computations presented in Strumberger & Günter (2019) were, to our knowledge, the first 3-D linear stability studies taking an externally driven toroidal flow into account. In the meantime, similar studies were made for gyroviscosity, ion drift velocity and ExB-velocity. They all can unlock strictly locked modes (Strumberger *et al*. 2023, 2025).

In (Puchmayr *et al*. 2023), the CASTOR3D code was used to investigate in more detail helical localisation and mode locking of edge-localised ideal MHD instabilities in rotating and flow-free magnetically perturbed tokamak plasmas. Applying an external two-periodic perturbation field to an axisymmetric tokamak test equilibrium, a 3-D tokamak equilibrium with $N_{per} = 2$ periodicity was produced that allowed to investigate instabilities of any mode number. Figure 19(*a*) shows the

https://doi.org/10.1017/S0022377826102153 Published online by Cambridge University Press

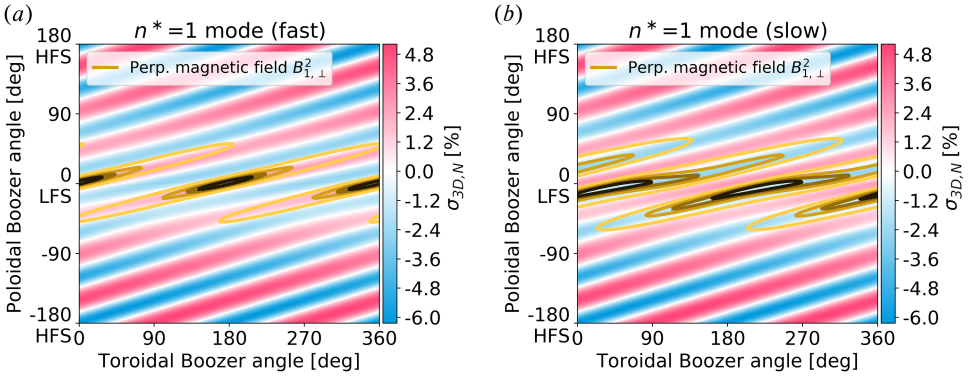


FIGURE 20. (*a*) Fast and (*b*) slow growing $n^* = 1$ modes at the most unstable flux surface. Background: normalised non-axisymmetric component of the parallel equilibrium current density $\sigma_{3D,N}$. Orange/brown lines: normalised perpendicular magnetic perturbation $\mathrm{Re}(B^2_{1,\perp})$ of the $n^* = 1$ mode, darker colour indicates a larger value of $\mathrm{Re}(B^2_{1,\perp})$. (From Puchmayr *et al.* (2023); licensed under a Creative Commons Attribution 4.0 licence (CC BY).)

corrugation of the plasma boundary, and figure 19(*b*) illustrates the maximum corrugation as function of the normalised toroidal flux caused by the $N_{per} = 2$ MP field. This displacement from the corresponding axisymmetric flux surface is very small (<1 cm) in comparison with the 3-D geometry of a stellarator. Nevertheless, it leads to toroidal mode-coupling, non-degenerate growth rates and mode locking.

In order to systematically analyse the helical/toroidal localisation of the modes, the helical localisation of the eigenfunctions were evaluated close to the most unstable flux surface (Puchmayr *et al.* 2023). The latter is determined by the minimum of the potential energy density corresponding to the dominating drive, which is δW_{CUR} (3.23) in the case of current-density driven instabilities and δW_{DP} (3.23) in the case of pressure-gradient driven instabilities. If there was no clearly dominating drive, the helical localisation was evaluated with respect to both energetic drives. For this evaluation, for example, the normalised square of the perpendicular magnetic field perturbation $\mathrm{Re}(\boldsymbol{B}_{1,\perp}e^{\mathrm{i}\varphi})^2$ was defined. Being normalised with respect to the square of the arbitrary amplitude of the eigenfunction, it represents the spatial structure/location of the mode while being independent of the arbitrary amplitude and sign of the eigenfunction. We denote a mode as strictly locked mode if $\mathrm{Re}(\boldsymbol{B}_{1,\perp}e^{\mathrm{i}\varphi})^2$ is completely independent of the solution phase φ.[22] Figure 20 shows the localisation/structure of $\mathrm{Re}(\boldsymbol{B}_{1,\perp})^2$ relative to the normalised non-axisymmetric part $\sigma_{3D,N}$ of the parallel equilibrium current density $\sigma(v, u) = \boldsymbol{j}_0 \cdot \boldsymbol{B}_0/B_0^2$ at the most unstable flux surface. It is

$$\sigma_{3D,N}(v, u) = (\sigma(v, u) - \sigma_{av}(u))/\Delta\sigma_{av}(u) \tag{4.3}$$

with $\sigma(u)_{av} = \langle\sigma(v, u)\rangle_v$ being the average of $\sigma(v, u)$ over the toroidal coordinate v for every poloidal coordinate u and $\Delta\sigma_{av} = \pm[\max\{\sigma_{av}\} - \min\{\sigma_{av}\}]$ being the variation of the axisymmetric parallel equilibrium current-density σ_{av} along the poloidal direction.[23] The two strictly locked $n^* = 1$ modes are located at different helical

[22]Note that the periodicity of the squared quantities is twice the periodicity of the corresponding mode, e.g. the energy densities and squared eigenvectors of an $n^* = 1$ mode have a periodicity of 2.

[23]The sign of $\Delta\sigma_{av}$ is chosen such that $\sigma_{3D,N} > 0$ stands for an augmented current density.

https://doi.org/10.1017/S0022377826102153 Published online by Cambridge University Press

positions, but at locations with maximum $\sigma_{3D,N}$. Since the modes are current driven, these locations also maximise their current drive (see Puchmayr *et al*. 2023). The faster growing $n^* = 1$ mode perfectly aligns with the regions of maximum $\sigma_{3D,N}$ (figure 20*a*) in contrast to the slower growing $n^* = 1$ mode which is shifted by $\delta v = \pi/2$ (figure 20*b*).

If the precise location of the eigenfunction is not fixed, but depends on the solution phase φ, the mode is quasilocked. That is, the location is bound to an envelope $E = \max_\varphi\{\mathrm{Re}(\boldsymbol{B}_{1,\perp}e^{\mathrm{i}\varphi})^2\}$ of periodicity N_{per} as illustrated in figures 21(*a*) and 21(*b*). There, the location of the perpendicular magnetic perturbation $\mathrm{Re}(\boldsymbol{B}_{1,\perp}e^{\mathrm{i}\varphi})^2$ at $\varphi = 0$ of the $n^* = 15$ mode as well as the corresponding envelope are shown. In order to determine the envelope, it was necessary to evaluate the eigenfunction at a range of solution phase angles φ. As expected, close to the most unstable flux surface, the envelope of the $n^* = 15$ eigenfunction is aligned with the maximum equilibrium current-density perturbation (see figure 21*c*). Quasilocked modes have degenerate eigenvalues in a flow-free 3-D plasma and immediately start rotation for any flow, that is, $\Omega_{\mathrm{thres}} = 0$.

Summing up the results, helically localised instabilities can be separated into two classes: quasilocked and strictly locked. In a flow-free 3-D plasma, the localisation of quasilocked modes is determined by an envelope, while their precise location under the envelope is arbitrary. Strictly locked modes, however, can only occur at a single helical position. They are forced to rotate for $\Omega_0 > \Omega_{\mathrm{thres}}$. Since these instabilities naturally want to stay at a fixed location, they rotate irregularly/non-uniform, like being pushed through a bottleneck as illustrated in figure 21(*d*). The irregularity of the rotation decreases with both increasing plasma flow and decreasing non-degeneracy of the instabilities in a flow-free plasma.

4.4. *Edge localised and external modes*

While former 3-D CASTOR3D stability calculations were restricted to low toroidal mode numbers (Strumberger & Günter 2019; Strumberger *et al*. 2020), now also stability studies for high-n^* edge localised and external modes in 3-D tokamak (Puchmayr *et al*. 2023, 2024) and stellarator configurations (Strumberger *et al*. 2025) are possible because of increasing memory and computing power, substantial improvement of the performance of the CASTOR3D code (Puchmayr 2023) (see also § 3.5), and, last but not least, using high fidelity equilibrium solutions computed with the GVEC code (Hindenlang *et al*. 2025*a*). We will start with investigating the ELM stability limit in 2-D and 3-D tokamak plasmas taking the ion diamagnetic drift effect into account.

4.4.1. The ELMs in 2-D and 3-D AUG tokamak plasmas

Type I ELMs limit the pressure gradient and lead to significant energy and particle losses in tokamak plasmas. In order to avoid severe damage in future fusion devices (e.g. ITER (Loarte *et al*. 2003)), they have to be suppressed or, at least, mitigated. The application of non-axisymmetric MP fields in various experiments (Evans *et al*. 2004; Nazikian *et al*. 2015; Suttrop *et al*. 2018) led to a mitigation or even suppression of ELMs because of an enhanced transport which reduces the pedestal density and pressure gradient (Kirk *et al*. 2011; Suttrop *et al*. 2018). Since the onset of Type I ELMs is very well described by the growth of edge-localised peeling–ballooning modes (Snyder *et al*. 2002; Wilson *et al*. 2006), a predictive linear stability analysis of ELMs is possible.

https://doi.org/10.1017/S0022377826102153 Published online by Cambridge University Press

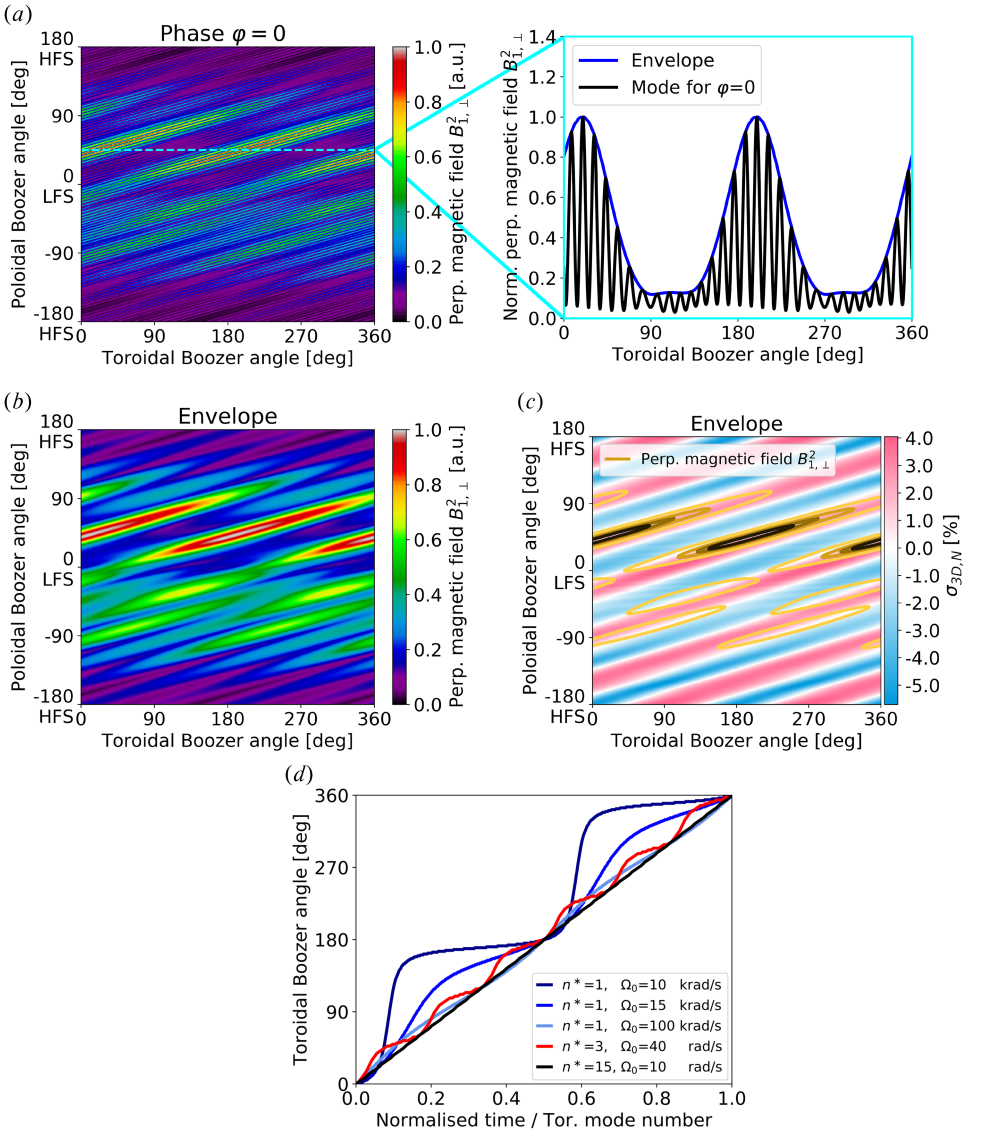


FIGURE 21. (*a*) Normalised perpendicular magnetic perturbation $\mathrm{Re}(\boldsymbol{B}_{1,\perp}e^{\mathrm{i}\varphi})^2$ of the $n^* = 15$ mode at $\varphi = 0$ and (*b*) its envelope $E = \max_\varphi\{\mathrm{Re}(\boldsymbol{B}_{1,\perp}e^{\mathrm{i}\varphi})^2\}$. (*c*) Background: normalised non-axisymmetric component of the parallel equilibrium current density $\sigma_{3D,N}$. Orange/brown lines: envelope E of the $n^* = 15$ mode, darker colour indicates a larger value of the envelope. (*d*) Relative toroidal position of the minimum of the normalised perpendicular magnetic perturbation for different mode numbers n^* over a full rotation cycle of the mode around the torus $\omega t \in [0, 2\pi\, n^*]$. The plasma rotation was taken at values above the critical rotation threshold for each n^*. (From Puchmayr *et al.* (2023); licensed under a creative commons attribution 4.0 licence (CC BY).)

Puchmayr (2023) and Puchmayr *et al.* (2024), the impact of symmetry-breaking induced by MP fields on the MHD stability limit was analysed for low-n kink-peeling mode up to high-n peeling–ballooning mode limited regimes considering, for the first time, ion diamagnetic drift effects in realistic non-axisymmetric (3-D) tokamak

https://doi.org/10.1017/S0022377826102153 Published online by Cambridge University Press

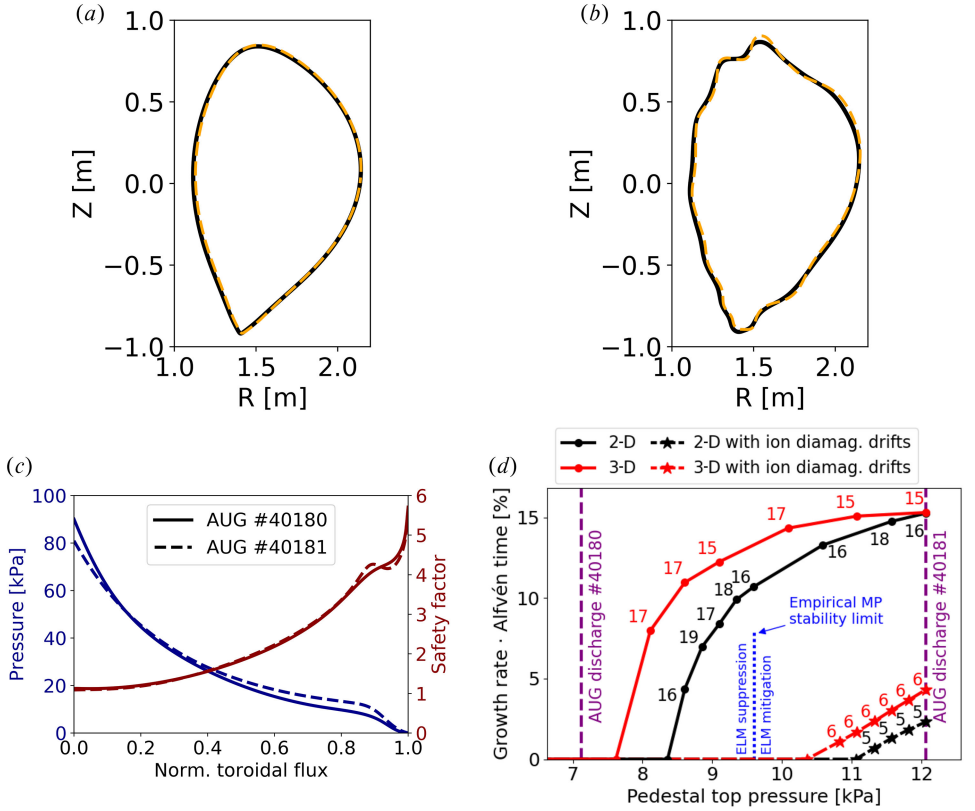


FIGURE 22. Toroidal cross-sections (*a*) for the axisymmetric and (*b*) magnetically perturbed equilibria of the AUG discharges #40180 (solid, black) and #40181 (dashed, orange) as well as (*c*) pressure and safety factor profiles. For visibility, the corrugation in (*b*) is amplified by a factor of 2.5. (*d*) Growth rates for a range of equilibria between AUG #40180 and AUG #40181 with and without ion diamagnetic drift effects. The numbers annotating the data points refer to the toroidal harmonic n^* of the most unstable instability. The dotted blue line indicates the empirical stability limit from Suttrop *et al*. (2018) assuming equal ion and electron pressures. (From Puchmayr *et al*. (2024); licensed under a Creative Commons Attribution 4.0 licence (CC BY).)

geometry. The application of MP fields leads to a corrugation of the equilibrium flux surfaces (Chapman *et al*. 2012; Willensdorfer *et al*. 2019). Figures 22(*a*) and 22(*b*) show the axisymmetric and the corrugated 3-D plasma boundaries of the AUG discharges #40180 (ELM suppression) and #40181 (ELM mitigation).[24] The maximum corrugation amounts to 7 mm for the ELM suppression and 13 mm for the ELM mitigation case at the low-field side. Their pressure and safety factor profiles are illustrated in figure 22(*c*). In order to analyse the transition from the ELM mitigation to the ELM suppression case, a range of equilibria with increasing pedestal top pressure was created inbetween these two cases. Figure 22(*d*) shows the normalised

[24]As NEMEC input served highly accurate equilibrium reconstructions of these AUG discharges performed with the CLISTE interpretive equilibrium code (McCarthy, Martin & Schneider 1999; Mc Carthy & the ASDEX Upgrade Team 2012).

https://doi.org/10.1017/S0022377826102153 Published online by Cambridge University Press

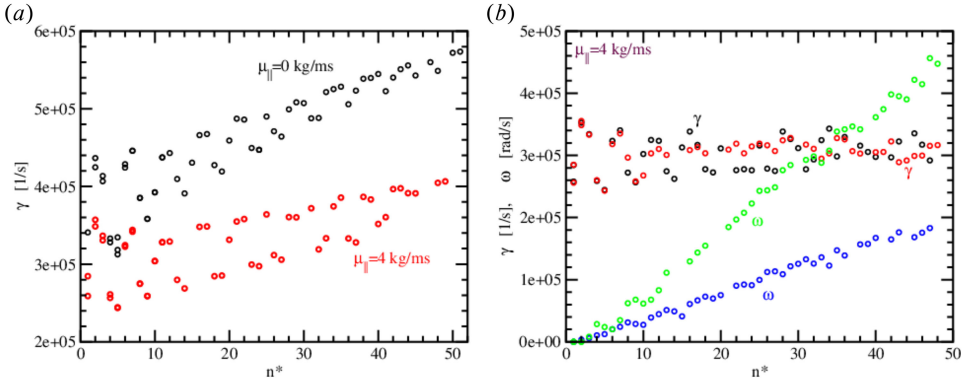


FIGURE 23. (*a*) Growth rates as functions of n^* without (black circles) and with (red circles) taking parallel viscosity into account. (*b*) Growth rates and oscillation frequencies as functions of n^* taking parallel and gyroviscosity into account. The results with and without additional ion diamagnetic drift and ExB-velocities are marked by red/green and black/blue circles, respectively. (From Strumberger *et al*. (2025); licensed under a Creative Commons Attribution licence (CC BY).)

growth rate as function of the pedestal top pressure for axisymmetric and 3-D equilibria with and without diamagnetic drift effects. The figure illustrates the decrease of the critical pedestal top pressure caused by the symmetry-breaking effect of the applied MP fields. In contrast to the experimental observations, the 2-D and 3-D numerical results predict highly unstable ballooning modes with $n^* = 15-19$ if no ion diamagnetic drift effect is taken into account. Inclusion of this effect leads to a considerable stabilisation and a reduction of the toroidal mode number to $n^* = 5$ or 6. Here, the peeling–ballooning modes are suppressed below the empirical MP stability limit and the finite growth rates correspond to mitigated peeling–ballooning modes. These results demonstrate the importance of 3-D stability studies and the inclusion of diamagnetic drift effects.

4.4.2. External kink and peeling–ballooning modes in a QA stellarator

In § 4.3, we described low-n^* locked modes in a two-periodic QA equilibrium and the effect of an external flow on these modes. Strumberger *et al*. (2025), the investigations of the same equilibrium were extended from low-n^* external kink modes to high-n^* peeling–ballooning modes. In addition to parallel viscosity and an external toroidal flow in symmetry direction, gyroviscosity, ion diamagnetic drift velocity and ExB-velocity were also considered in this work. The growth rates as function of the dominant toroidal mode number n^* are illustrated in figure 23(*a,b*). Figure 23(*a*) compares the growth rates obtained without and with a parallel viscosity of $\mu_\parallel = 4$ kg ms^{-1}.[25] The parallel viscosity has a stabilising effect which increases with n^*. The high-n^* peeling–ballooning modes are clearly less unstable if parallel viscosity is included. Nevertheless, the high-n^* peeling–ballooning modes are still the most unstable modes.

Assuming that there is no external flow drive and that the ambipolarity condition (3.9) holds ($\boldsymbol{V}_{ExB} = -\boldsymbol{V}^*_{i0}$), all terms containing $\boldsymbol{V}_0$ disappear in the linearised MHD

[25]The value of $\mu_\parallel$ was estimated using (3.4) for a collisionless plasma.

https://doi.org/10.1017/S0022377826102153 Published online by Cambridge University Press

equations (2.18–2.21), and the momentum equation (2.19) reads

$$\rho_0\lambda \boldsymbol{V}_1 = -\frac{1}{m_i}\boldsymbol{\nabla}(\rho_0 T_1) - \frac{1}{m_i}\boldsymbol{\nabla}(T_0\rho_1) + \rho_0(\boldsymbol{V}_{i0}^{*}\cdot\boldsymbol{\nabla})\boldsymbol{V}_1 + \mu_{||}\Delta_{||}\boldsymbol{V}_1 + \frac{1}{\mu_0}(\boldsymbol{\nabla}\times(\boldsymbol{\nabla}\times\boldsymbol{A}_1))\times(\boldsymbol{\nabla}\times\boldsymbol{A}_0) + \frac{1}{\mu_0}(\boldsymbol{\nabla}\times(\boldsymbol{\nabla}\times\boldsymbol{A}_0))\times(\boldsymbol{\nabla}\times\boldsymbol{A}_1). \tag{4.4}$$

While the parallel viscosity only reduces the growth rate, but does not cause mode oscillations, the gyroviscosity leads to oscillations. Figure 23(*b*) compares growth rates and oscillation frequencies obtained without and with including ion diamagnetic drift and ExB-velocities additionally to parallel and gyroviscosity. Here, the ion diamagnetic drift velocity and the ExB-velocity increase the oscillation frequency by more than a factor of 2, but they have a negligible effect on the growth rate. However, all effects together stabilise the high-n^* peeling–ballooning modes so much that the $n^*=2$ external kink mode becomes the most unstable mode. Analogous to the external flow, gyroviscosity, drift and ExB-velocity are able to unlock modes (Strumberger *et al*. 2025) and can lead to overstable modes as will be described in § 4.5.2.

Interesting is also the combination of external flow, gyroviscosity, ion diamagnetic drift velocity and ExB-velocity. In Strumberger *et al*. (2025), we considered a toroidal velocity, $\boldsymbol{V}_{tor}^{ext}=(1/(2\pi))\Omega_{tor}^{ext}(s)\boldsymbol{r}_{,v}$, externally driven in the symmetry direction v (Boozer toroidal coordinate). We assumed $\Omega_{tor}^{ext}(s)=\Omega_0^{ext}(1-0.8s^4)$ with $-25\,000\leqslant\Omega_0^{ext}\leqslant 25\,000$ rad s^{-1}. Figure 24(*a–d*) show growth rates and oscillation frequencies of $n^*=2$, 3 and 7 external kink modes and $n^*=22$ and 47 peeling–ballooning modes as functions of the externally driven flow frequency Ω_0^{ext}. Depending on the sign of Ω_0^{ext}, the additional external drive increases or decreases the damping effects caused by gyroviscosity, ion diamagnetic drift velocity and ExB-velocity and also changes the oscillation frequencies of the modes. The growth rate decreases if the chosen flow direction leads to an increase of the oscillation frequency of the mode and *vice versa*. This behaviour is in good agreement with the results obtained by Aiba (2016). Using the MINERVA-DI code, he investigated axisymmetric equilibria with circular cross-section. Yet, an additional effect appears in the case of the considered 3-D equilibria. Appropriate external flow compensates the oscillation frequencies caused by gyroviscosity, diamagnetic drift velocity and ExB-velocity and, therefore, locks the low-n^* modes. While the oscillation frequencies become zero, the growth rates split into two values.

Finally, the presented results show that direction and magnitude of the external flow may decide whether a low-n^* external kink or a high-n^* peeling–ballooning mode will be the most unstable mode. In figure 24(*c*), the black stars mark the growth rates of the $n^*=2$ mode for $\Omega_0^{ext}=-25\,000$ rad s^{-1} and 25 000 rad s^{-1}, respectively. Here, the growth rate of the $n^*=22$ mode has almost reached the value of the $n^*=2$ mode for $\Omega_0^{ext}=-25\,000$ rad s^{-1}. That is, a sufficiently fast external flow in negative v-direction is able to compensate the stabilising effects of gyroviscosity, ion diamagnetic velocity and ExB-velocity on the high-n^* peeling–ballooning modes and to make them to the most unstable modes of the considered equilibrium, while the growth rates of low-n^* modes are only weakly affected by the flows (see figures 23*b* and 24*a*).

https://doi.org/10.1017/S0022377826102153 Published online by Cambridge University Press

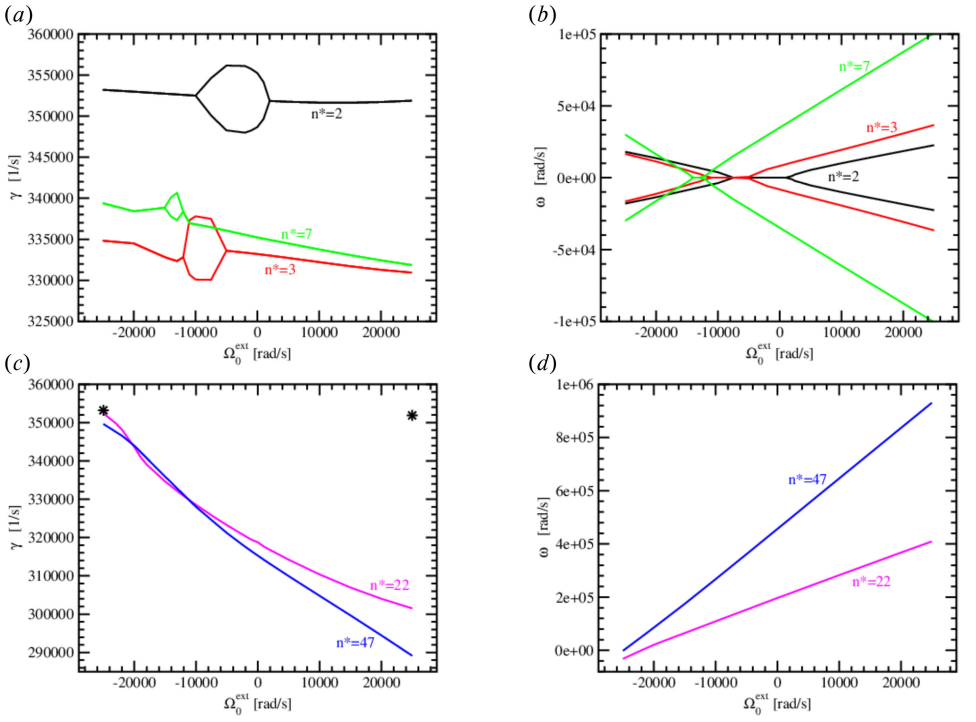


FIGURE 24. (*a,c*) Growth rates and (*b,d*) oscillation frequencies of (*a,b*) $n^* = 2$, 3 and 7 external kink modes, and (*c,d*) $n^* = 22$ and 47 peeling–ballooning modes as functions of the externally driven toroidal flow frequency Ω_0^{ext} taking parallel viscosity ($\mu_{||} = 4$ kg ms^{-1}), gyroviscosity, ion diamagnetic drift velocity and ExB-velocity into account. The solutions were obtained solving (*a,b*) the full eigenvalue problem and (*c,d*) the reduced eigenvalue problem. (*c*) The two black stars located in the left- and right-hand corners mark the growth rates of the $n^* = 2$ mode. (From Strumberger *et al*. (2025); licensed under a Creative Commons Attribution licence (CC BY).)

4.5. *Overstable modes*

Since the CASTOR3D code solves a complex eigenvalue problem with eigenvalue $\lambda = \gamma + \mathrm{i}\omega$ (2.17), it is able to find overstable modes. Such modes simultaneously oscillate and grow exponentially. However, in contrast to modes where the oscillation frequency describes their rotation caused by a finite plasma flow (e.g. externally driven flows, ExB-velocity or drift effects), the frequency of overstable modes results from the oscillation between two mode structures.

4.5.1. Axisymmetric equilibria

In axisymmetric equilibria, an overstable mode can occur if, at least, two unstable modes of the same *n*-type exist and their growth rates overlap within certain ranges of plasma parameters. When the growth rates as functions of a single parameter (e.g. pressure gradient (Kerner *et al*. 1986), resistivity (Huysmans *et al*. 1993), etc.) become the same, an overstable oscillating mode evolves. We will illustrate this process for an example of DTMs. These modes appear in the case of reversed shear *q*-profiles (e.g. Günter *et al*. 2000). Mostly, the two tearing modes forming around the positions of equal *q*-values couple asymmetrically, but a symmetric coupling is also possible (Otto & Birk 1992).

https://doi.org/10.1017/S0022377826102153 Published online by Cambridge University Press

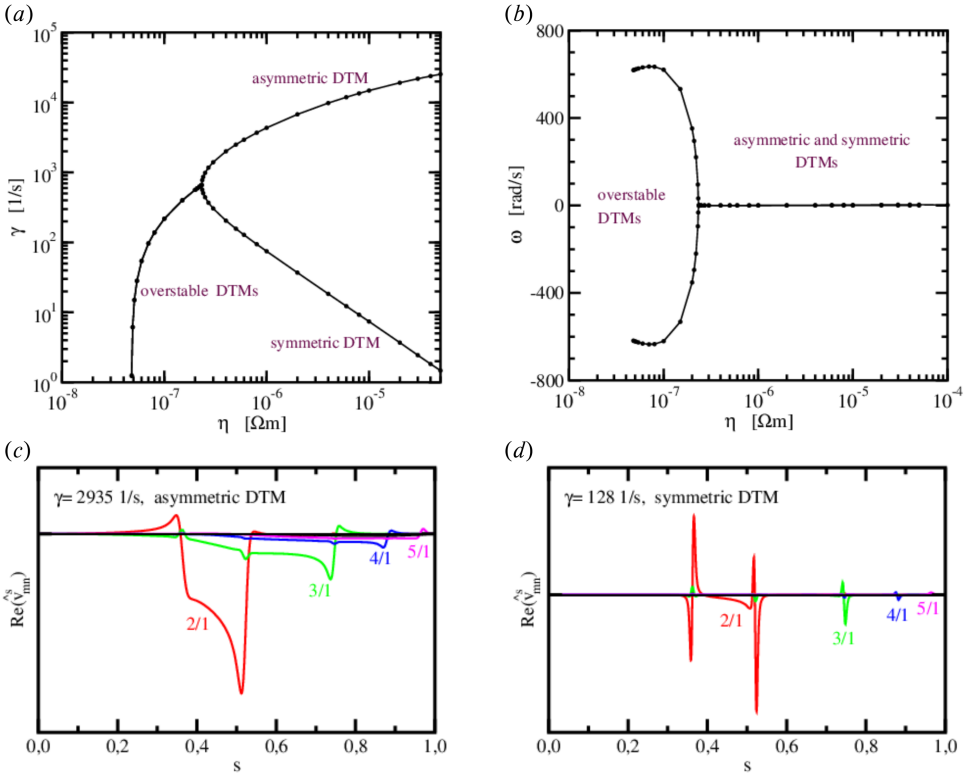


FIGURE 25. Double tearing modes of an AUG-type equilibrium. (*a*) Growth rates and (*b*) oscillation frequencies as functions of the resistivity. (*c,d*) Real parts of the eigenfunction Fourier spectra of the radial velocity perturbation for (*c*) an asymmetric- and (*d*) a symmetric-coupled DTM for $\eta = 6 \times 10^{-7}$ Ωm.

Figures 25(*a*) and 25(*b*) show the growth rates and oscillation frequencies in dependence of the plasma resistivity for 2/1 DTMs of an AUG-type equilibrium. The two $q = 2$ surfaces being located at $s_1 = 0.36$ and $s_2 = 0.52$ have a distance of $\Delta s = 0.16$. While the growth rate of the asymmetric DTM becomes smaller with decreasing resistivity, the growth rate of the symmetric DTM increases. When the growth rates of both modes come close, an oscillating overstable mode forms. Then, the eigenvalue problem yields two overstable solutions with $\gamma_1 = \gamma_2$ and $\omega_1 = -\omega_2$. Both solutions describe the same mode with the opposite signs of the frequencies indicating a phase shift in the oscillation cycle. Figures 25(*c*) and 25(*d*) illustrate the eigenfunction Fourier spectra of the radial velocity perturbations of the asymmetric- and the symmetric-coupled DTM for $\eta = 6 \times 10^{-7}$ Ωm.

4.5.2. The 3-D equilibria

In contrast to axisymmetric equilibria, overstable modes can also evolve if the growth rates of different n^*-type modes of the same mode family overlap within a certain parameter range because the toroidal harmonics are coupled in 3-D equilibria. Investigating the growth rates of internal resistive modes (Strumberger *et al*. 2020) and ideal external modes (Strumberger *et al*. 2025) as functions of resistivity, viscosity and plasma flows, several overstable modes between various n^*-types were

https://doi.org/10.1017/S0022377826102153 Published online by Cambridge University Press

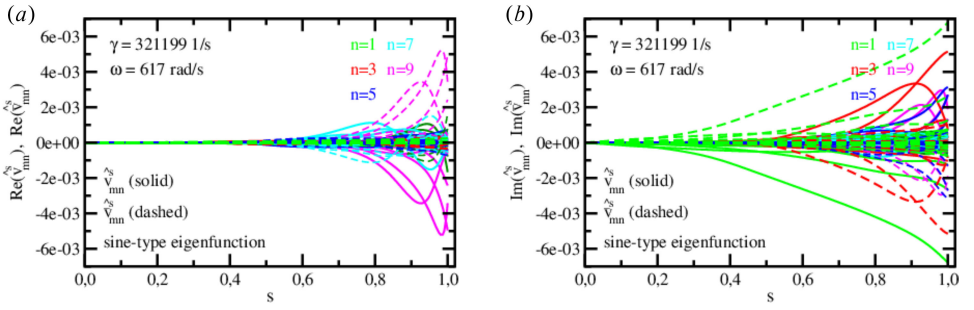


FIGURE 26. Overstable $n^* = 1 \leftrightarrow n^* = 9$ external kink mode of a QA equilibrium: (*a*) real and (*b*) imaginary part of the eigenfunction Fourier spectrum for the radial velocity perturbation of the sine-type overstable mode (parallel viscosity: $\mu_{||} = 1.1$ kg ms^{-1}). (From Strumberger *et al.* (2025); licensed under a Creative Commons Attribution licence (CC BY).)

found. Considering the QA equilibrium discussed in Strumberger & Günter (2019) and Strumberger *et al.* (2025), figure 26 illustrates the oscillation of an overstable $n^* = 1 \leftrightarrow n^* = 9$ external kink mode that appeared within a certain range of the parallel viscosity. Here, the real part of the Fourier spectrum shows an $n^* = 9$ structure, while the imaginary part of the Fourier spectrum corresponds to an $n^* = 1$ mode. That is, the overstable mode oscillates between these two structures.

4.6. *Resistive wall modes*

External modes often limit the achievable plasma-β of magnetically confined fusion plasmas because these modes are too fast to be controlled by an active feedback system. For quite some time, it is well known that conducting walls have a stabilising effect on those modes depending on mode type and wall distance (Freidberg *et al.* 1975; Wesson 1978). While an ideal wall could perhaps stabilise such a mode completely, a realistic resistive wall only reduces the growth rate down to the resistive time scale of the wall

$$\tau_w = \mu_0 \sigma_w d_w r_w \tag{4.5}$$

with σ_w being the specific conductivity, d_w and r_w being width and distance of the wall and μ_0 being the vacuum permeability. The growth rate of such a resistive wall mode may be slow enough to be stabilised by an active feedback system and/or plasma rotation (see Chu & Okabayashi (2010) and references quoted therein). Codes studying the active feedback-stabilisation of resistive wall modes are, for example, CarMa (Portone *et al.* 2008) and CarMa-D (Bonotto *et al.* 2020), NMA (Chu *et al.* 2003), VALEN (Bialek *et al.* 2001) and STARWALL/OPTIM (Sempf *et al.* 2009). The STARWALL/OPTIM code is able to handle 3-D equilibria, while CarMa-D is not restricted to resistive time scales.

Feedback-stabilisation is not included in the CASTOR3D code. But, it is able to handle 3-D equilibria and, because of solving the extended eigenvalue problem (2.89), it is not restricted to resistive time scales. This enables the calculation of growth rates in the range of very rapid modes down to slow resistive wall modes and to take into account resistivity, flow, viscosity, drift effects and heat conductivity. In order to test the code, we performed benchmark studies between CASTOR3D, STARWALL and an analytical model (Strumberger *et al.* 2014*a*).

https://doi.org/10.1017/S0022377826102153 Published online by Cambridge University Press

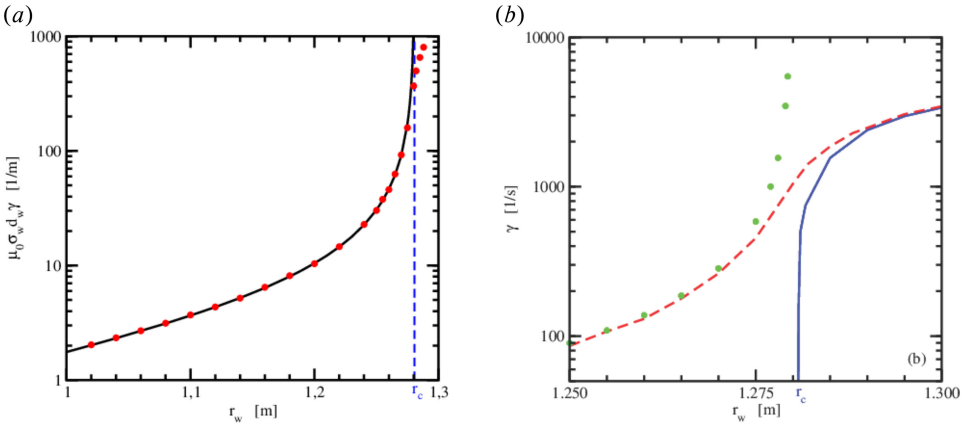


FIGURE 27. Comparison of the normalised CASTOR3D growth rate (red dots/dashed line) with (*a*) the analytical growth rate (black line) and (*b*) the STARWALL growth rate (green dots) as functions of the distance of the resistive wall. The dashed blue vertical line in (*a*) marks the critical radius r_c while in (*b*) the growth rate as function of the ideal wall distance is indicated by the blue solid line. (From Strumberger *et al*. (2014*a*); licensed under a Creative Commons Attribution 3.0 licence (CC BY).)

Fitzpatrick & Yu (1998) derived an analytical expression for the normalised growth rate

$$\bar{\gamma} = \gamma \tau_w = \frac{2m}{(r_c/r_w)^{2m} - 1} \tag{4.6}$$

of a resistive wall mode. For this purpose, they approximated the plasma as a cylinder with radius a. In (4.6), m denotes the poloidal mode number of the unstable mode, r_w is the wall distance and r_c names the critical radius with $r_w = r_c$ corresponding to the ideal stability boundary.

As described in Strumberger *et al*. (2014*a*), we used a circular-shaped, axisymmetric plasma equilibrium with high aspect ratio, $A = 10$, and negligibly low plasma-β to simulate the plasma cylinder. Moreover, we used the same q-profile as in Fitzpatrick & Yu (1998) with $q_a = 1.3$ and $q_b = 2.9$ being the values of the safety factor at the magnetic axis and the plasma boundary. The considered equilibrium is unstable with respect to an $m = 3, n = 1$ ideal external kink mode. Surrounding the plasma with an ideal conducting wall with circular cross-section and variable radius, the CASTOR3D calculations delivered a critical radius of $r_c = 1.28073$ m at which the ideal wall stabilises the mode. Inserting this value into the analytical formula (4.6) yielded the growth rate as function of the wall distance illustrated by the black curve in figure 27(*a*). Very close, but still within this radius, the analytical growth rate rapidly increases because the analytical function (4.6) diverges for $r_w = r_c$. In figure 27(*a*), the red filled circles mark the CASTOR3D growth rates which excellently agree with the analytical results for $r_w < r_c$. Unlike the analytical solution, the CASTOR3D growth rates stay finite for $r_w \geqslant r_c$ because here the increase of the growth rate is limited by the plasma inertia. With further growing wall distance, the growth rate converges against the no-wall limit as shown in figure 27(*b*). Here, the dashed red line marks the CASTOR3D growth rate while the STARWALL results are indicated by the green filled circles. In the case of low growth rates,

https://doi.org/10.1017/S0022377826102153 Published online by Cambridge University Press

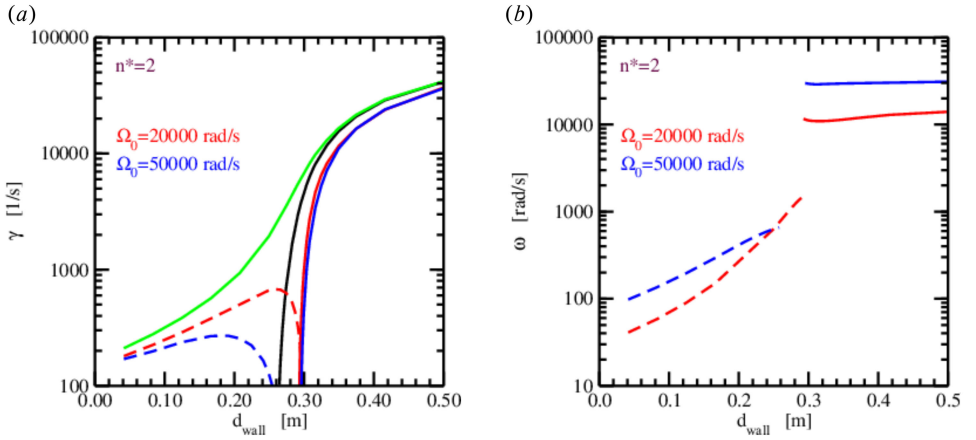


FIGURE 28. For the QA equilibrium, (*a*) growth rates and (*b*) oscillation frequencies of the $n^* = 2$ mode as functions of the wall distance d_w are shown. The growth rates are obtained for an ideal closed wall (black), a resistive closed wall (green), and a resistive closed wall in combination with plasma flow (red, $\Omega_0 = 200\,000$ rad s^{-1}; blue, $\Omega_0 = 50\,000$ rad s^{-1}). The solid red and blue curves mark the plasma modes while the dashed curves denote the resistive wall modes. (Reproduced with permission from Nucl. Fusion vol. 59, 2019, p. 106008 and EUROfusion. Copyright EURATOM 2019.)

CASTOR3D and STARWALL results agree very well. Yet, higher growth rates of the latter diverge because STARWALL neglects the plasma inertia.

Bondeson & Ward (1994) showed that a resistive wall in combination with plasma rotation may stabilise external kink modes in tokamaks. Considering a two-periodic, high-β, rotating, QA equilibrium surrounded by a closed resistive wall, we verified that the same holds for stellarators (Strumberger & Günter 2019). We computed growth rate and oscillation frequency of an $n^* = 2$ ideal external kink mode as functions of the plasma–wall distance of a thin ($\delta_w = 0.5$ cm), closed copper ($\sigma_w = 56 \times 10^6$ S m^{-1}) wall. The wall distance d_{wall} was measured at the outer midplane of the $\varphi = 0^o$ cross-sections of the QA equilibrium. The computations were performed for various cases: (i) ideal wall, no plasma rotation; (ii) resistive wall, no rotation; (iii) resistive wall, plasma rotation $\Omega_0 = 20\,000$ rad s^{-1}; (iv) resistive wall, plasma rotation $\Omega_0 = 50\,000$ rad s^{-1}. A parallel ion viscosity of $\mu_{||} = 50$ kg ms^{-1} was taken into account and we used $\Omega(s) = \Omega_0(1 - 0.7s^2)$ as toroidal rotation profile.

As illustrated in figure 28, growth rates and oscillation frequencies showed the expected behaviour. The ideal wall stabilises the $n^* = 2$ mode at a certain distance, while the mode remains unstable for all distances in the case of a resistive wall. Taking plasma rotation into account, two mode branches exist (as described for tokamaks in Bondeson & Ward (1994)): (i) the growth rate of the so-called plasma mode decreases with shrinking wall distance while it strongly oscillates; (ii) the growth rate of the resistive wall mode finally decreases with growing wall distance while the oscillation frequency of this mode is small. Furthermore, a narrow stability window arises for a toroidal plasma rotation frequency of $\Omega_0 = 50\,000$ rad s^{-1}.

4.7. *Vertical instability*

Elongated axisymmetric equilibria are vertically unstable. Implementing appropriate resistive wall structures, the growth rate of such a vertical instability can be

https://doi.org/10.1017/S0022377826102153 Published online by Cambridge University Press

reduced. At best, the growth rate becomes small enough, so that a fast feedback system is able to control the plasma position. In AUG, the PSL (see figure 2) and two fast control coils (1 ms response time) located nearby the plasma control the vertical position of the plasma (Mertens, Raupp & Treutterer 2003). Currents induced in the PSL may slow down the time constant of the vertical motion to $\sim$80 ms, so that an active feedback control acting on the two fast position control coils can stabilise the plasma position.

Using the CASTOR3D code, the vertical instability of an AUG equilibrium (#39655) is investigated at $t = 3.05$, 3.06 and 3.07 s.[26] For a correct treatment of the $m = 0, n = 0$ harmonic (Lüst & Martensen 1960; Merkel & Strumberger 2015), 16 toroidal field coils are taken into account as passive conductor structures.[27] These coils allow for a net-poloidal current in the vacuum region that originates from this kind of perturbation. However, they have no stabilising effect because of their large distance to the plasma. The $m = 0, n = 0$ harmonic has no noteworthy contribution to the growth rate of the vertical instability, but its contribution to the poloidal velocity perturbation is essential to obtain the correct mode structure (Strumberger & Günter 2019). Figure 29(*a–c*) show the mode structures of an elliptically shaped test equilibrium (Strumberger & Günter 2017) and the AUG equilibrium at $t = 3.05$ s and $t = 3.07$ s. The three vector plots illustrate the velocity perturbations. The mode structure of the elliptically shaped plasma represents very well the shift of a rigid body. Yet, the situation is slightly different for the AUG equilibria. Here, the plasma is also shifted as a whole, but length and direction of the vectors show small deviations. It should be noted that the direction of the vectors gives no information whether the plasma is moving upward or downward because in linear MHD the multiplication of an eigenfunction by an arbitrary complex number results in an equivalent eigenfunction corresponding to the same eigenvalue as the original eigenfunction. However, the location of the reconstructed equilibrium in figure 29(*c*) indicates a downward movement of the plasma which corresponds to the main direction given by mode structure shown in figure 29(*b*). The upper and lower parts of the PSL marked by the bars in figures 29(*b*) and 29(*c*) have a width of $d_{PSL} = 9$ cm and are made of copper with a specific conductivity of $\sigma = 56.2 \times 10^6$ S m^{-1}. Varying the width and with it the conductivity $G = \sigma d$, the growth rates shown in figure 29(*d*) are obtained. Here, the vertical dashed line marks the full width of the PSL. At $t = 3.05$ s the growth rate of the vertical instability is reduced to $\gamma = 20\,\mathrm{s}^{-1}$ for $d = 4$ cm.[28] At $t = 3.06$ s, however, even a PSL with an effective full width would reduce the growth rate only to $\gamma = 76\,\mathrm{s}^{-1}$ and at $t = 3.07$ s the vertical instability can no longer be appreciably stabilised by the PSL. The increase of the growth rate at these time steps agrees very well with the experimental observation and corresponding nonlinear stability studies performed with the JOREK code where the discharge ended with a hot vertical displacement event (Schwarz *et al.* 2023).

The thin wall approximation used in the vacuum part of the CASTOR3D code corresponds to a situation in which the skin depth

$$d_{skin} = \sqrt{\frac{2}{\mu_0 \sigma_w \gamma}} \tag{4.7}$$

[26]The equilibrium reconstruction of the discharge was performed with the CLISTE code.

[27]Here, the shapes of the AUG toroidal field coils are used.

[28]At this point the numerical limit of CASTOR3D was reached.

https://doi.org/10.1017/S0022377826102153 Published online by Cambridge University Press

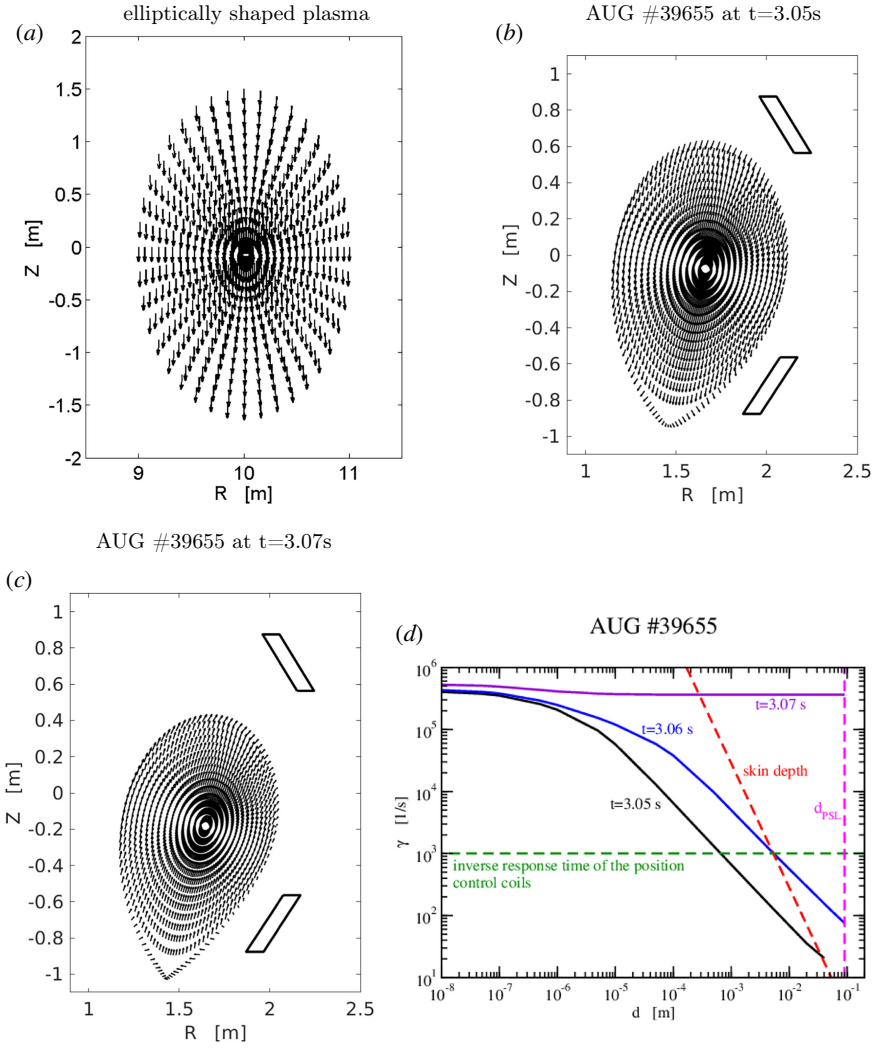


FIGURE 29. Mode structures of vertical instabilities of (*a*) an elliptically shaped plasma with high aspect ratio (reproduced with permission from Nucl. Fusion vol. 57, 2017, p. 016032 and EUROfusion; copyright 2016 EURATOM) and (*b,c*) AUG discharge #39655. The vectors illustrate the velocity perturbation. The bars indicate the positions of the upper and lower parts of the PSL. (*d*) Growth rates as functions of the width of the PSL.

is much greater than the wall thickness d_w (Wesson 1997; Sehmer *et al*. 2016). In figure 29(*d*) the red dashed line indicates the skin depth related with the growth rate of the vertical instability. Its intersection points with the growth rate curves give a rough estimate how far the growth rates can be reduced by the PSL. For more accurate studies the finite width of the PSL would have to be taken into account by coupling CASTOR3D with the CARIDDI code (Albanese & Rubinacci 1988, 1997). Yet, CASTOR3D is a fast tool that can help to identify equilibria which cannot be stabilised by the PSL to growth rates well below the feedback stabilisation limit. That is, when new tokamak equilibria are designed, CASTOR3D can be used

https://doi.org/10.1017/S0022377826102153 Published online by Cambridge University Press

to sort out equilibria that would definitely be terminated by a vertical displacement event (Vanovac *et al*. 2026).

5. Summary and outlook

This review article summarises the theoretical fundamentals and the structure of the CASTOR3D code. Several numerical improvements of the code, increased computer power and highly accurate equilibria provided by the GVEC code enable highly resolved extended linear MHD stability studies for 2-D and 3-D magnetically confined plasma equilibria. The code takes into account plasma resistivity, parallel viscosity, ion and electron diamagnetic drift effects, parallel heat conductivity, ExB-velocity and externally driven flows. The combination of MHD and vacuum equations to an extended eigenvalue problem allows free-boundary stability studies in the presence of resistive wall and coil structures without neglecting the plasma inertia.

Various examples are presented for the versatile application possibilities of CASTOR3D ranging from simple axisymmetric equilibria to 3-D tokamak and stellarator equilibria and from low-n^* internal kink and DTMs up to high-n^* peeling–ballooning modes. Overstable modes arising in 2-D and 3-D configurations are compared and locked modes are investigated. The stabilising effect of resistive walls is studied for an axisymmetric test equilibrium and a QA equilibrium. Finally, investigating the vertical instability of an AUG discharge illustrates the possibility to identify highly vertically unstable equilibria.

In the past, mostly the ideal instability of stellarators was studied, while the investigation of plasma flow, resistivity, viscosity, etc., was usually limited to axisymmetric plasma configurations. CASTOR3D, however, provides a numerical tool that enables the extension of these numerical studies to 3-D tokamak and stellarator-type configurations.

Recently, the parallel heat conductivity (see § 3.2.3) has been implemented in CASTOR3D. Corresponding studies are in work and will be published in the near future.

Future research will focus on a broader validation of the newly implemented equilibrium flow and electron diamagnetic drift models through systematic comparisons of simulations with experimental observations of MHD modes in tokamaks and stellarators. Further extensions of the underlying MHD model, such as the inclusion of further two-fluid effects or runaway-electron physics, will enhance the physical fidelity of future stability studies. In addition, exploiting advanced preconditioned iterative eigensolvers, together with the increasing availability of GPU-based HPC architectures, is expected to substantially improve the computational performance and efficiency of CASTOR3D.

Acknowledgements

Editor Paolo Ricci thanks the referees for their advice in evaluating this article.

Funding

This work has been carried out within the framework of the EUROfusion Consortium, funded by the European Union via the Euratom Research and Training Programme (grant agreement no. 101052200 - EUROfusion). Views and opinions expressed are, however, those of the author(s) only and do not necessarily reflect

https://doi.org/10.1017/S0022377826102153 Published online by Cambridge University Press

those of the European Union or the European Commission. Neither the European Union nor the European Commission can be held responsible for them.

Declaration of interests

The authors report no conflict of interest.

Appendix A. Details of the weak formulation

A.1 *Hermite polynomials*

The radial dependence of the perturbed quantities (2.30) and the test functions (2.36, 2.37) is expressed by quadratic and cubic Hermite polynomials, respectively (Kerner *et al*. 1998)). The Hermite polynomials, illustrated in figure 30, read on an interval $s_j \leqslant s \leqslant s_{j+1}$:

quadratic Hermite polynomials,

$$h_{j,1} = 0, \qquad h_{j,2} = \frac{2(s-s_m)(s-s_{j+1})}{(s_{j+1}-s_j)^2},$$

$$h_{j+1,1} = \frac{4(s-s_j)(s_{j+1}-s)}{(s_{j+1}-s_j)^2}, \qquad h_{j+1,2} = \frac{2(s-s_m)(s-s_j)}{(s_{j+1}-s_j)^2} \tag{A1}$$

with $s_m = 0.5(s_{j+1}+s_j)$;

cubic Hermite polynomials,

$$H_{j,1} = 3\frac{(s_{j+1}-s)^2}{(s_{j+1}-s_j)^2} - 2\frac{(s_{j+1}-s)^3}{(s_{j+1}-s_j)^3}, \qquad H_{j,2} = (s-s_j)\frac{(s-s_{j+1})^2}{(s_{j+1}-s_j)^2},$$

$$H_{j+1,1} = 3\frac{(s-s_j)^2}{(s_{j+1}-s_j)^2} - 2\frac{(s-s_j)^3}{(s_{j+1}-s_j)^3}, \qquad H_{j+1,2} = (s-s_{j+1})\frac{(s-s_j)^2}{(s_{j+1}-s_j)^2}; \tag{A2}$$

first derivatives of the cubic Hermite polynomials,

$$H'_{j,1} = \frac{-6}{(s_{j+1}-s_j)}\left(\frac{(s_{j+1}-s)}{(s_{j+1}-s_j)} - \frac{(s_{j+1}-s)^2}{(s_{j+1}-s_j)^2}\right),$$

$$H'_{j+1,1} = \frac{6}{(s_{j+1}-s_j)}\left(\frac{(s-s_j)}{(s_{j+1}-s_j)} - \frac{(s-s_j)^2}{(s_{j+1}-s_j)^2}\right),$$

$$H'_{j,2} = \frac{(s-s_{j+1})^2}{(s_{j+1}-s_j)^2} + \frac{2(s-s_j)(s-s_{j+1})}{(s_{j+1}-s_j)^2},$$

$$H'_{j+1,2} = \frac{(s-s_j)^2}{(s_{j+1}-s_j)^2} + \frac{2(s-s_{j+1})(s-s_j)}{(s_{j+1}-s_j)^2}. \tag{A3}$$

As already mentioned, the matrices $\boldsymbol{A}$ and $\boldsymbol{B}$ in (2.34) have a block-tridiagonal structure because of the local basis of the Hermite polynomials. Due to this basis, only neighbouring radial grid points couple together. That is, a single block connects two neighbouring radial coordinate points. The overlapping elements (diagonal elements) are superpositions of the neighbouring blocks and the total dimension of a block is $N_B = 2 \times 2N_f N_{mn} N_q$.

https://doi.org/10.1017/S0022377826102153 Published online by Cambridge University Press

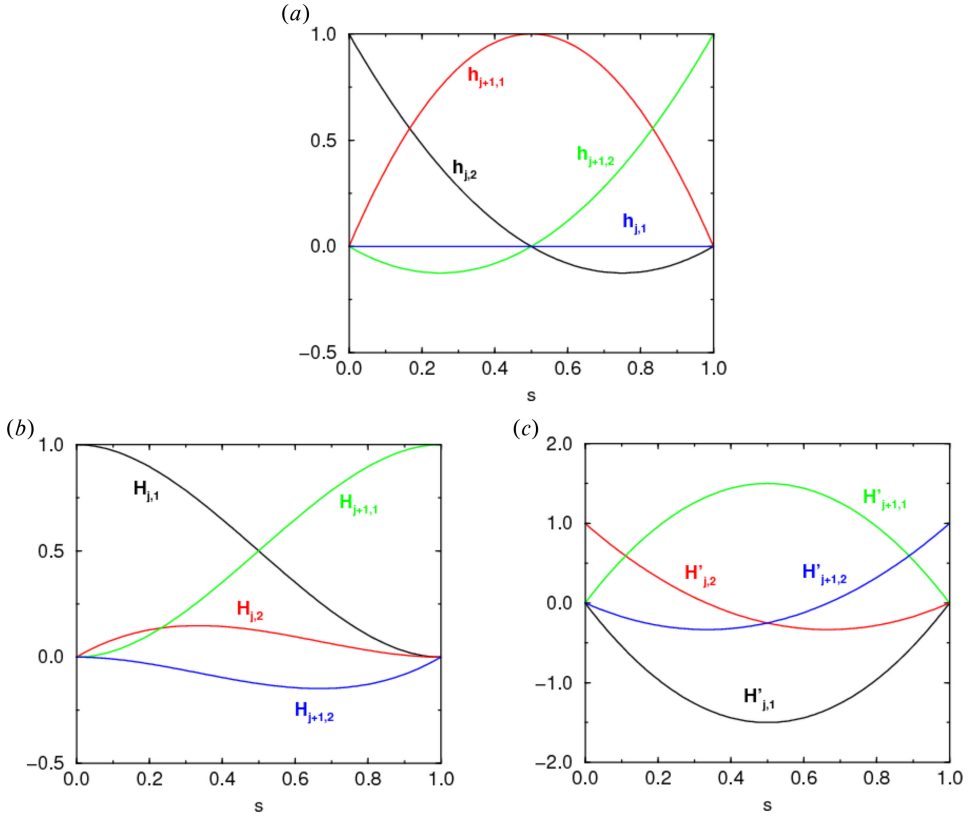


FIGURE 30. (*a*) Quadratic Hermite polynomials, (*b*) cubic Hermite polynomials and (*c*) first derivatives of the cubic Hermite polynomials on an interval $s_j \leqslant s \leqslant s_{j+1}$.

A.2 *Computation of the matrix elements*

In the following, we describe vicariously the computation of elements of matrix $\boldsymbol{B}$. Using the test function $\hat{z}^{*s,\tilde{m},\tilde{n}}_{\tilde{f},\tilde{j},\tilde{q}}$ (2.36) and a component $\hat{w}_f$ (2.30) of the symbolic vector $\boldsymbol{w}$ (2.29), the inner product (2.33) yields

$$\int \mathrm{d}V \hat{z}^{*s,\tilde{m},\tilde{n}}_{\tilde{f},\tilde{j},\tilde{q}}(s,v,u) L_{\tilde{f},f}(s,v,u) \hat{w}_f(s,v,u)$$

$$= \int \mathrm{d}s \int \mathrm{d}u \int \mathrm{d}v \left[h^{\tilde{j}}_{\tilde{f},\tilde{q}}(s) \frac{1}{2\mathrm{i}} \left(\mathrm{e}^{2\pi \mathrm{i}(\tilde{m}u+\tilde{n}v)} - \mathrm{e}^{-2\pi \mathrm{i}(\tilde{m}u+\tilde{n}v)} \right) \underbrace{\sqrt{g} \hat{t}_{\tilde{f}} L_{\tilde{f},f}}_{EQ_{\tilde{f},f}(s,v,u)} \right.$$

$$\left. \sum_{m,n,j,q} \left(c^{m,n}_{f,j,q} h^{j}_{f,q}(s) \mathrm{e}^{2\pi \mathrm{i}(mu+nv)} + \breve{c}^{m,n}_{f,j,q} h^{j}_{f,q}(s) \mathrm{e}^{-2\pi \mathrm{i}(mu+nv)} \right) \right]. \tag{A4}$$

In the case of 3-D equilibria, the equilibrium quantities are functions of s, u and v and their Fourier representation reads

$$EQ_{\tilde{f},f}(s,v,u) = \sum_{k,l} eq^{k,l}_{\tilde{f},f}(s) \mathrm{e}^{2\pi \mathrm{i}(ku+lv)} + eq^{*k,l}_{\tilde{f},f}(s) \mathrm{e}^{-2\pi \mathrm{i}(ku+lv)} \tag{A5}$$

https://doi.org/10.1017/S0022377826102153 Published online by Cambridge University Press

with the complex $eq^{k,l}_{\tilde{f},f}$ and complex conjugate $eq^{*k,l}_{\tilde{f},f}$ coefficients. Inserting the Fourier representation (A5) into (A4), we obtain

$$
\begin{aligned}
&\int ds\, h^{\tilde{j}}_{\tilde{f},\tilde{q}}(s) \sum_{j,q} h^{j}_{f,q}(s) \sum_{m,n} \int \mathrm{d}u \int \mathrm{d}v \sum_{k,l} \Bigg[\\
&\quad \frac{1}{2\mathrm{i}} eq^{k,l}_{\tilde{f},f}(s) \mathrm{e}^{2\pi\mathrm{i}(\tilde{m}u+\tilde{n}v)} \mathrm{e}^{2\pi\mathrm{i}(ku+lv)} \mathrm{e}^{2\pi\mathrm{i}(mu+nv)} \qquad (k=-\tilde{m}-m,\ l=-\tilde{n}-n) \\
&- \frac{1}{2\mathrm{i}} eq^{k,l}_{\tilde{f},f}(s) \mathrm{e}^{-2\pi\mathrm{i}(\tilde{m}u+\tilde{n}v)} \mathrm{e}^{2\pi\mathrm{i}(ku+lv)} \mathrm{e}^{2\pi\mathrm{i}(mu+nv)} \qquad (k=\tilde{m}-m,\ l=\tilde{n}-n) \\
&+ \frac{1}{2\mathrm{i}} eq^{*k,l}_{\tilde{f},f}(s) \mathrm{e}^{2\pi\mathrm{i}(\tilde{m}u+\tilde{n}v)} \mathrm{e}^{-2\pi\mathrm{i}(ku+lv)} \mathrm{e}^{2\pi\mathrm{i}(mu+nv)} \qquad (k=\tilde{m}+m,\ l=\tilde{n}+n) \\
&- \frac{1}{2\mathrm{i}} eq^{*k,l}_{\tilde{f},f}(s) \mathrm{e}^{-2\pi\mathrm{i}(\tilde{m}u+\tilde{n}v)} \mathrm{e}^{-2\pi\mathrm{i}(ku+lv)} \mathrm{e}^{2\pi\mathrm{i}(mu+nv)} \qquad (k=-\tilde{m}+m,\ l=-\tilde{n}+n) \\
&\quad \Bigg] c^{m,n}_{f,j,q} \\
&+ \int ds h^{\tilde{j}}_{\tilde{f},\tilde{q}}(s) \sum_{j,q} h^{j}_{f,q}(s) \sum_{m,n} \int \mathrm{d}u \int \mathrm{d}v \sum_{k,l} \Bigg[\\
&\quad \frac{1}{2\mathrm{i}} eq^{k,l}_{\tilde{f},f}(s) \mathrm{e}^{2\pi\mathrm{i}(\tilde{m}u+\tilde{n}v)} \mathrm{e}^{2\pi\mathrm{i}(ku+lv)} \mathrm{e}^{-2\pi\mathrm{i}(mu+nv)} \qquad (k=-\tilde{m}+m,\ l=-\tilde{n}+n) \\
&- \frac{1}{2\mathrm{i}} eq^{k,l}_{\tilde{f},f}(s) \mathrm{e}^{-2\pi\mathrm{i}(\tilde{m}u+\tilde{n}v)} \mathrm{e}^{2\pi\mathrm{i}(ku+lv)} \mathrm{e}^{-2\pi\mathrm{i}(mu+nv)} \qquad (k=\tilde{m}+m,\ l=\tilde{n}+n) \\
&+ \frac{1}{2\mathrm{i}} eq^{*k,l}_{\tilde{f},f}(s) \mathrm{e}^{2\pi\mathrm{i}(\tilde{m}u+\tilde{n}v)} \mathrm{e}^{-2\pi\mathrm{i}(ku+lv)} \mathrm{e}^{-2\pi\mathrm{i}(mu+nv)} \qquad (k=\tilde{m}-m,\ l=\tilde{n}-n) \\
&- \frac{1}{2\mathrm{i}} eq^{*k,l}_{\tilde{f},f}(s) \mathrm{e}^{-2\pi\mathrm{i}(\tilde{m}u+\tilde{n}v)} \mathrm{e}^{-2\pi\mathrm{i}(ku+lv)} \mathrm{e}^{-2\pi\mathrm{i}(mu+nv)} \qquad (k=-\tilde{m}-m,\ l=-\tilde{n}-n) \\
&\quad \Bigg] \check{c}^{m,n}_{f,j,q} \\
&= \sum_{j,m,n,q} B^{1,1,\tilde{m},m,\tilde{n},n}_{\tilde{f},f,\tilde{j},j,\tilde{q},q} c^{m,n}_{f,j,q} + B^{1,2,\tilde{m},m,\tilde{n},n}_{\tilde{f},f,\tilde{j},j,\tilde{q},q} \check{c}^{m,n}_{f,j,q}
\end{aligned}
\tag{A6}
$$

and, analogously, for the test function $\hat{z}^{*\mathrm{c},\tilde{m},\tilde{n}}_{\tilde{f},\tilde{j},\tilde{q}}$ (2.37)

$$
\int \mathrm{d}V \hat{z}^{*\mathrm{c},\tilde{m},\tilde{n}}_{\tilde{f},\tilde{j},\tilde{q}}(s,v,u) L_{\tilde{f},f}(s,v,u) \hat{w}_f(s,v,u) = \sum_{j,m,n,q} B^{2,1,\tilde{m},m,\tilde{n},n}_{\tilde{f},f,\tilde{j},j,\tilde{q},q} c^{m,n}_{f,j,q} + B^{2,2,\tilde{m},m,\tilde{n},n}_{\tilde{f},f,\tilde{j},j,\tilde{q},q} \check{c}^{m,n}_{f,j,q}. \tag{A7}
$$

The integration over the poloidal and toroidal coordinates in combination with the summation $\sum_{k,l}$ only yields non-vanishing contributions if $\tilde{m}, m, k$ and $\tilde{n}, n, l$ fulfil the conditions given on the right side of (A6). Using the weighting coefficients $g_1 = 0.173927422568727$, $g_2 = 0.326072577431273$, $g_3 = 0.326072577431273$ and $g_4 = 0.173927422568727$, the radial integral within an interval of two neighbouring

https://doi.org/10.1017/S0022377826102153 Published online by Cambridge University Press

radial grid points $s_{j'} \leqslant s \leqslant s_{j'+1}$ is numerically integrated at four special radial grid points

$$s_1 = s_m - \text{facs1} \times \mathrm{d}s, \quad s_2 = s_m - \text{facs2} \times \mathrm{d}s,$$
$$s_3 = s_m + \text{facs2} \times \mathrm{d}s, \quad s_4 = s_m + \text{facs1} \times \mathrm{d}s \tag{A8}$$

with $s_m = 0.5(s_{j'} + s_{j'+1})$, $\mathrm{d}s = (s_{j'+1} - s_{j'})$ and the factors facs1 = 0.430568155797026 and facs2 = 0.169990521792428, that is,

$$\int_{s_{j'}}^{s_{j'+1}} \mathrm{d}s\, h^{\tilde{j}}_{\tilde{f},\tilde{q}}(s) eq^{k,l}_{\tilde{f},f}(s) h^{j}_{\tilde{f},\tilde{q}}(s) = \sum_{i=1}^{4} h^{\tilde{j}}_{\tilde{f},\tilde{q}}(s_i) eq^{k,l}_{\tilde{f},f}(s_i) h^{j}_{f,q}(s_i) \times g_i \tag{A9}$$

with $\tilde{j} \in [j', j'+1]$ and $j \in [j', j'+1]$.

Appendix B. The COTRANS code

The COTRANS (coordinate transformation) code connects the equilibrium codes NEMEC and GVEC with the CASTOR3D code (see figure 5). The code executes the following tasks:

(i) it reads the equilibrium input;

(ii) it transforms the equilibrium coordinates into the flux coordinate type desired for the CASTOR3D stability studies (Strumberger *et al*. 2005), that is, equilibrium flux coordinates (NEMEC coordinates), 2-D straight field line coordinates (only in the case of axisymmetric equilibria) or Boozer coordinates. Besides, it is possible to choose between the following radial coordinate types

$$s = \frac{\Phi_0}{\Phi_0^{tot}}, \quad s = \sqrt{\frac{\Phi_0}{\Phi_0^{tot}}}, \quad s = \frac{\Psi_0 - \Psi_0^a}{\Psi_0^b - \Psi_0^a}, \quad \text{or} \quad s = \sqrt{\frac{\Psi_0 - \Psi_0^a}{\Psi_0^b - \Psi_0^a}} \tag{B1}$$

with toroidal flux Φ, its total value Φ_{tot}. poloidal flux Ψ and its axis Ψ_a and boundary values Ψ_b, respectively;

(iii) it creates the radial grid (equidistant or non-equidistant) which shall be used in the CASTOR3D code and, within each grid interval, it determines the four radial grid points (A8) used for the radial integration (A9). The user can choose between a user-defined non-equidistant grid and several automatically created non-equidistant grids depending on the instabilities of interest;

(iv) at every radial integration point, it computes all combinations of equilibrium quantities needed by the CASTOR3D code and converts them into their Fourier representation (A5);

(v) it writes the equilibrium input file for CASTOR3D.

The code is MPI and OMP parallelised and uses a fast Fourier transformation technique which enables the quick processing of highly resolved 3-D equilibria.

The separation into COTRANS and CASTOR3D was necessary because the computations performed with the COTRANS code, even though it is highly optimised, can still be very time- and memory-consuming, and, usually, one COTRANS run provides the input for many CASTOR3D runs.

https://doi.org/10.1017/S0022377826102153 Published online by Cambridge University Press

REFERENCES

AIBA, N. 2016 Impact of ion diamagnetic drift on ideal ballooning mode stability in rotating tokamak plasmas. *Plasma Phys. Control. Fusion* **58**, 045020.

ALBANESE, R. & RUBINACCI, G. 1988 Integral formulation for 3d eddy-current computation using edge elementes. *IEE Proc., Part A: Phys. Sci., Meas. Instrum., Manage. Educ. Rev.* **135**, 457.

ALBANESE, R. & RUBINACCI, G. 1997 Finite element methods for the solution of 3D eddy current problems. *Adv. Imaging Electron Phys.* **102**, 1.

ANDERSON, D.V., COOPER, W.A., GRUBER, R., MERAZZI, S. & SCHWENN, U. 1990 Methods for the efficient calculation of the (MHD) magnetohydrodynamic stability properties of magnetically confined fusion plasmas. *Intl J. Supercomput. Appl.* **4**, 34.

BALAY, S. *et al.* 2026 PETSc/TAO Users Manual. Anl-21/39 rev v3.24.4-507-g0b8bdde92eb4. Argonne National Laboratory.

BARLOW, I. *et al.* 2001 The error field correction coils on the JET machine. *Fusion Engng Des.* **58–59**, 189–193.

BERNARD, L.C., HELTON, F.J. & MOORE, R.W. 1981 GATO: an MHD stability code for axisymmetric plasmas with internal separatrices. *Comput. Phys. Commun.* **24**, 377.

BERNSTEIN, I.B., FRIEMAN, E.A., KRUSKAL, M.D. & KULSRUD, R.M. 1958 An energy principle for hydromagnetic stability problems. *Proc. R. Soc. Lond. A* **244**, 17.

BIALEK, J., BOOZER, A.H., MAUEL, M.E. & NAVRATIL, G.A. 2001 Modeling of active control of external magnetohydrodynamic instabilities. *Phys. Plasmas* **8**, 2170–2180.

BONDESON, A. & WARD, D.J. 1994 Stabilization of external modes in tokamaks by resistive walls and plasma rotation. *Phys. Rev. Lett.* **72**, 2709.

BONOTTO, M., LIU, Y.Q., VILLONE, F., PIGATTO, L. & BETTINI, P. 2020 Expanded capabilities of the CarMa code in modeling resistive wall mode dynamics with 3-D conductors. *Plasma Phys. Control. Fusion* **62**, 045016.

BOOZER, A.H. 1982 Establishment of magnetic coordinates for a given magnetic field. *Phys. Fluids* **25**, 520.

BRAGINSKII, S.I. 1965 Transport processes in a plasma. In *Reviews of Plasma Physics* (ed. M.A. Leontovich), vol. I, p. 205. Consultants Bureau.

BUTTERY, R.J. *et al.* 1999 Error field mode studies on JET, COMPASS-D and DIII-D, and implications for ITER. *Nucl. Fusion* **39**, 1827.

CHANG, Z. & CALLEN, J.D. 1992*a* Generalized gyroviscous force and its effect on the momentum balance equation. *Phys. Fluids B: Plasma Phys.* **4**, 1766.

CHANG, Z. & CALLEN, J.D. 1992*b* Unified fluid/kinetic description of plasma microinstabilities. Part 1: basic equations in a sheared slab geometry. *Phys. Fluids B: Plasma Phys.* **4**, 1167.

CHAPMAN, I. *et al.* 2012 Three-dimensional corrugation of the plasma edge when magnetic perturbations are applied for edge-localized mode control in MAST. *Plasma Phys. Control. Fusion* **54**, 105013.

CHAPMAN, I.T., SHARAPOV, S.E., HUYSMANS, G.T.A. & MIKHAILOVSKII, A.B. 2006 Modelling the effect of toroidal plasma rotation on drift-magnetohydrodynamic modes in tokamaks. *Phys. Plasmas* **13**, 062511.

CHEN, J.G., XU, X.Q. & LEI, Y.A. 2019 Extension of Landau-fluid closure to weakly collisional plasma regime. *Comput. Phys. Commun.* **236**, 128.

CHU, M.S., CHANCE, M.S., GLASSER, A.H. & OKABAYASHI, M. 2003 Normal mode approach to modelling of feedback stabilization of the resistive wall mode. *Nucl. Fusion* **43**, 441.

CHU, M.S., GREENE, J.M., JENSEN, T.H., MILLER, R.L., BONDESON, A., JOHNSON, R.W. & MAUEL, M.E. 1995 Effect of toroidal plasma flow and flow shear on global magnetohyrdodynamic MHD modes. *Phys. Plasmas* **2**, 2236.

CHU, M.S. & OKABAYASHI, M. 2010 Stabilization of the external kink and the resistive wall mode. *Plasma Phys. Control. Fusion* **52**, 123001.

DEGTYAREV, L., MARTYNOV, A., MEDVEDEV, S., TROYON, F., VILLARD, L. & GRUBER, R. 1997 The KINX ideal MHD stability code for axisymmetric plasmas with separatrix. *Comput. Phys. Commun.* **103**, 10.

EVANS, T.E. *et al.* 2004 Suppression of large edge-localized modes in high-confinement DIII-D plasmas with a stochastic magnetic boundary. *Phys. Rev. Lett.* **92**, 235003.

https://doi.org/10.1017/S0022377826102153 Published online by Cambridge University Press

FITZPATRICK, R. & YU, E.P. 1998 Optimal design of feedback coils for the control of external modes in tokamaks. *Phys. Plasmas* **5**, 2340.

FREIDBERG, J.P., GOEDBLOED, J.P., GROSSMANN, W. & HAAS, F.A. 1975 Stability of kink modes in high-beta tokamaks. In *Proc. 5th Intl Conf. Plasma Physics and Controlled Nuclear Fusion Research, 1974, Tokyo* (ed. International Atomic Energy Agency), vol. 1, p. 505. IAEA.

FRERICHS, H., VAN BLARCUM, J., COTE, T., KIM, S.K., LIU, Y.Q. & YANG, S.M. 2026 Comparison of plasma response models for RMP effects on the divertor and scrape-off layer in KSTAR. *Nucl. Fusion* **66**, 076005.

FU, G.Y., COOPER, W.A., GRUBER, R., SCHWENN, U. & ANDERSON, D.V. 1992 Fully three-dimensional ideal magnetohydrodynamic stability analysis of low-*n* modes and Mercier modes in stellarators. *Phys. Fluids B: Plasma Phys.* **4**, 1401–1411.

GLASSER, A.H. 2025 The DCON3D code for the ideal MHD stability of stellarator equilibria with nested flux surfaces. *Phys. Plasmas* **32**, 082504.

GOODMAN, A.G., CAMACHO MATA, K., HENNEBERG, S.A., JORGE, R., LANDREMAN, M., PLUNK, G.G., SMITH, H.M., MACKENBACH, R.J.J., BEIDLER, C.D. & HELANDER, P. 2023 Constructing precisely quasi-isodynamic magnetic fields. *J. Plasma Phys.* **89**, 905890504.

GREENE, J.M. & JOHNSON, J.L. 1968 Interchange instabilities in ideal hydromagnetic theory. *Plasma Phys.* **10**, 729.

GRIMM, R.C., DEWAR, R.L. & MANICKAM, J. 1983 Ideal MHD stability calculations in axisymmetric toroidal coordinate systems. *J. Comput. Phys.* **49**, 94–117.

GRIMM, R.C., GREENE, J.M. & JOHNSON, J.L. 1976 Computation of the magnetohydrodynamic spectrum in axisymmetric toroidal confinement systems. In *Controlled Fusion* (ed. J. KILLEEN), vol. 16, pp. 253–280. Elsevier.

GRUBER, R., TROYON, F., BERGER, D., BERNARD, L.C., ROUSSET, S., SCHREIBER, R., KERNER, W., SCHEIDER, W. & ROBERTS, K.V. 1981 ERATO stability code. *Comput. Phys. Commun.* **21**, 323–371.

GÜNTER, S., SCHADE, S., MARASCHEK, M., PINCHES, S.D., STRUMBERGER, E., WOLF, R., YU, Q. & the ASDEX Upgrade Team 2000 MHD phenomena in reversed shear discharged on ASDEX Upgrade. *Nucl. Fusion* **40**, 1541.

HANEY, S.W. & FREIDBERG, J.P. 1989 Variational methods for studying tokamak stability in the presence of a thin resistive wall. *Phys. Fluids B* **1**, 1637.

HELANDER, P. & SIMAKOV, A.N. 2008 Intrinsic ambipolarity and rotation in stellarators. *Phys. Rev. Lett.* **101**, 145003.

HENDER, T.C. *et al.* 1992 Effect of resonant magnetic perturbations on COMPASS-C tokamak discharges. *Nucl. Fusion* **32**, 2091.

HENNEBERG, S.A., DREVLAK, M., NÜHRENBERG, C., BEIDLER, C.D., TURKIN, Y., LOIZU, J. & HELANDER, P. 2019 Properties of a new quasi-axisymmetric configuration. *Nucl. Fusion* **59**, 026014.

HINDENLANG, F., BABIN, R., MAJ, O., RIBEIRO, T., KOEBERL, R., MUIR, D., PLUNK, G. & SONNENDRÜCKER, E. 2025*a* GVEC: a flexible 3D MHD equilibrium solver. *Zenodo*. https://doi.org/10.5281/zenodo.15026781.

HINDENLANG, F., PLUNK, G.G. & MAJ, O. 2025*b* Computing MHD equilibria of stellarators with a flexible coordinate frame. *Plasma Phys. Control. Fusion* **67**, 045002.

HIRSHMAN, S.P., VAN RIJ, W.I. & MERKEL, P. 1986 Three-dimensional free boundary calculations using a spectral Greens's function method. *Comput. Phys. Commun.* **43**, 143.

HIRSHMAN, S.P. & WHITSON, J.C. 1983 Steepest-descent moment method for three-dimensional magnetohydrodynamic equilibria. *Phys. Fluids* **26**, 3553–3568.

HUYSMANS, G.T.A. 1991 External resistive modes in tokamak. *PhD thesis*, Vrije Universiteit Amsterdam.

HUYSMANS, G.T.A., GOEDBLOED, J.P. & KERNER, W. 1993 Free boundary resistive modes in tokamaks. *Phys. Fluids B: Plasma Phys.* **5**, 1545.

HUYSMANS, G.T.A., SHARAPOV, S.E., MIKHAILOVSKII, A.B. & KERNER, W. 2001 Modeling of diamagnetic stabilization of ideal magnetohydrodynamic instabilities associated with the transport barrier. *Phys. Plasmas* **8**, 4292.

https://doi.org/10.1017/S0022377826102153 Published online by Cambridge University Press

KERNER, W., GOEDBLOED, J.P., HUYSMANS, G.T.A., POEDTS, S. & SCHWARZ, E. 1998 CASTOR: normal-mode analysis of resistive MHD plasmas. *J. Comput. Phys.* **142**, 271.

KERNER, W., JAKOBY, A. & LERBINGER, K. 1986 Finite-element semi-discretization of linearized compressible and resistive MHD. *J. Comput. Phys.* **66**, 332.

KERNER, W., POEDTS, S., GOEDBLOED, J.P., HUYSMANS, G.T.A., KEEGAN, B. & SCHWARZ, E. 1991 Computing the damping and destabilisation of global Alfvén waves in tokamaks. In *18th EPS Conf. on Contr. Fusion and Plasma Phys., ECA* (ed. P. Bachmann & D.C. Robinson), vol. 15 Part IV, p. 89. European Physical Society.

KIRK, A. *et al.* 2011 Magnetic perturbation experiments on MAST L- and H-mode plasmas using internal coils. *Plasma Phys. Control. Fusion* **53**, 065011.

LA HAYE, R.J., FITZPARTRICK, R., HENDER, T.C., MORRIS, A.W., SCOVILLE, J.T. & TODD, T.N. 1992 Critical error fields for locked mode instability in tokamaks. *Phys. Fluids B: Plasma Phys.* **4**, 2098.

LIANG, Y. *et al.* 2007 Active control of type-I edge-localized modes with $n = 1$ perturbation fields in the JET tokamak. *Phys. Rev. Lett.* **98**, 265004.

LION, J. *et al.* 2025 Stellaris: a high-field quasi-isodynamic stellarator for a prototypical fusion power plant. *Fusion Engng Des.* **214**, 114868.

LIU, Y.Q., BONDESON, A., FRANSSON, C.M., LENNARTSON, B. & BREITHOLTZ, C. 2000 Feedback stabilization of nonaxisymmetric resistive wall modes in tokamaks. I. Electromagnetic model. *Phys. Plasmas* **7**, 3681.

LIU, Y., CHU, M.S., CHAPMAN, I.T. & HENDER, T.C. 2008 Toroidal self-consistent modeling of drift kinetic effects on the resistive wall mode. *Phys. Plasmas* **15**, 112503.

LOARTE, A. *et al.* 2003 Characteristics of type I ELM energy and particle losses in existing devices and their extrapolation to ITER. *Plasma Phys. Control. Fusion* **45**, 1549.

LÜST, R. & MARTENSEN, E. 1960 Zur Mehrwertigkeit des skalaren magnetischen potentials beim hydromagnetischen stabilitätsproblem eines plasmas. *Z. Naturforschung* **15a**, 706.

MC CARTHY, P.J. & the ASDEX Upgrade Team. 2012 Identification of edge-localized moments of the current density profile in a tokamak equilibrium from external magnetic measurements. *Plasma Phys. Control. Fusion* **54**, 015010.

MCCARTHY, P.J., MARTIN, P. & SCHNEIDER, W. 1999 The CLISTE interpretive equilibrium code. Laboratory Report IPP. 5/85, Max-Planck-Institut für Plasmaphysik.

MERKEL, P. & STRUMBERGER, E. 2015 Linear MHD stability studies with the STARWALL code. arXiv:1508.04911.

MERTENS, V., RAUPP, G. & TREUTTERER, W. 2003 Chapter 3: plasma control in ASDEX Upgrade. *Fusion Sci. Technol.* **44**, 593.

MOEN, T.E. & SUZUKI, Y. 2023 The effects of anisotropic pressure on plasma displacement and its deviation from flux surfaces. *Nucl. Fusion* **63**, 126002.

NAVE, M.F.F. & WESSON, J.A. 1990 Mode locking in tokamaks. *Nucl. Fusion* **30**, 2575.

NAZIKIAN, R. *et al.* 2015 Pedestal bifurcation and resonant field penetration at the threshold of edge-localized mode suppression in the DIII-D tokamak. *Phys. Rev. Lett.* **114**, 105002.

NIKULSIN, N., RAMASAMY, R., HOELZL, M., HINDENLANG, F., STRUMBERGER, E., LACKNER, K., GÜNTER, S. & the JOREK Team. 2022 JOREK3D: an extension of the JOREK nonlinear MHD code to stellarators. *Phys. Plasmas* **29**, 063901.

NÜHRENBERG, C. 1996 Global ideal magnetohydrodynamic stability analysis for the configurational space of Wendelstein 7–X. *Phys. Plasmas* **3**, 2401–2410.

NÜHRENBERG, C. 2016 Free-boundary ideal MHD stability of W7-X divertor equilibria. *Nucl. Fusion* **56**, 076010.

NÜHRENBERG, C. 2021 Ideal magnetohydrodynamic stability in stellarators with subsonic equilibrium flow. *Plasma Phys. Control. Fusion* **63**, 125035.

NÜHRENBERG, J., LOTZ, W. & GORI, S. 1994 Quasi-axisymmetric tokamaks. In *Theory of Fusion Plasmas, ISPP-15*, Proc. Joint Varenna-Lausanne Intl Workshop, Varenna, Italy (ed. E. Sindoni, F. Troyon & J. Vaclavik), p. 3. Società Italiana di Fisica.

NÜHRENBERG, J. & ZILLE, R. 1988 Quasi-helically symmetric toroidal stellarators. *Phys. Lett. A* **129**, 113–117.

https://doi.org/10.1017/S0022377826102153 Published online by Cambridge University Press

OKABAYASHI, M. *et al.* 2005 Control of the resistive wall mode with internal coils in the DIII–D tokamak. *Nucl. Fusion* **45**, 1715.

OTTO, A. & BIRK, G.T. 1992 Resistive instability of periodic current sheets. *Phys. Fluids B: Plasma Phys.* **4**, 3811–3813.

PAMELA, S.J.P., BHOLE, A., HUIJSMANS, G.T.A., NKONGA, B., HOELZL, M., KREBS, I. & STRUMBERGER, E. 2020 Extended full-MHD simulation of non-linear instabilities in tokamak plasmas. *Phys. Plasmas* **27**, 102510.

PATIL, S.A. & SOVINEC, C.R. 2024 Benchmarking of NIMSTELL for tearing modes in stellarators and preconditioner improvements. *Bull. Am. Phys. Soc* **66**, PP12.00002.

PIRON, L. *et al.* 2023 On the use of error field correction coils in JET. *Fusion Engng Des.* **197**, 114069.

PIRON, L., KIRK, A., LIU, Y.Q., CUNNINGHAM, G., CARR, M., GOWLAND, R., KATRAMADOS, I. & MARTIN, R. 2020 Error field correction strategies in preparation to MAST-U operation. *Fusion Engng Des.* **161**, 111932.

PORTONE, A., VILLONE, F., LIU, Y., ALBANESE, R. & RUBINACCI, G. 2008 Linearly perturbed MHD equilibria and 3D eddy current coupling via the control surface method. *Plasma Phys. Control. Fusion* **50**, 085004.

PUCHMAYR, J. 2023 Magnetohydrodynamic stability analysis of non-axisymmetric tokamak plasmas using the linear visco-resistive stability code CASTOR3D. *PhD thesis*, Fakultät für Physik der Ludwig-Maximilians-Universität München.

PUCHMAYR, J., DUNNE, M. & STRUMBERGER, E. 2022 An intuitive form of the energy functional for resistive plasma perturbations. *J. Plasma Phys.* **88**, 905880512.

PUCHMAYR, J., DUNNE, M., STRUMBERGER, E., WILLENSDORFER, M., ZOHM, H., HINDENLANG, F. & the ASDEX Upgrade Team 2023 Helical mode localization and mode locking of ideal MHD instabilities in magnetically perturbed tokamak plasmas. *Nucl. Fusion* **63**, 086008.

PUCHMAYR, J., DUNNE, M., STRUMBERGER, E., WILLENSDORFER, M., ZOHM, H., HINDENLANG, F. & the ASDEX Upgrade Team 2024 Effect of symmetry-breaking on the MHD edge stability limit of tokamak plasmas. *Nucl. Fusion* **64**, 086013.

RAMASAMY, R., ALEYNIKOVA, K., NIKULSIN, N., HINDENLANG, F., HOLOD, I., STRUMBERGER, E., HOELZL, M. & the JOREK Team 2024 Nonlinear MHD modeling of soft beta limits in W7-AS. *Nucl. Fusion* **64**, 086030.

REDL, A., ANGIONI, C., BELLI, E., SAUTER, O., the ASDEX Upgrade Team & the EUROfusion MST1 Team 2021 A new set of analytical formulae for the computation of the bootstrap current and the neoclassical conductivity in tokamaks. *Phys. Plasmas* **28**, 022502.

RICE, J.E. 2016 Experimental observations of driven and intrinsic rotation in tokamak plasmas. *Plasma Phys. Control. Fusion* **58**, 083001.

ROMAN, J.E., CAMPOS, C., DALCIN, L., ROMERO, E. & TOMÁS, A. 2025 Slepc users manual. Technical Report DSIC-II/24/02, Universidad Politècnica de València.

SAUTER, O., ANGIONI, C. & LIN-LIU, Y.R. 1999 Neoclassical conductivity and bootstrap current formulas for general axisymmetric equilibria and arbitrary collisionality regime. *Phys. Plasmas* **6**, 2834.

SAUTER, O., ANGIONI, C. & LIN-LIU, Y.R. 2002 Erratum: 'Neoclassical conductivity and bootstrap current formulas for general axisymmetric equilibria and arbitrary collisionality regime' [Phys. Plasmas 6, 2834 (1999)]'. *Plasmas, Phys. Plasmas* **9**, 5140.

SCHNACK, D.D., BARNES, D.C., BRENNAN, D.P., HEGNA, C.C., HELD, E., KIM, C.C., KRUGER, S.E., PANKIN, A.Y. & SOVINEC, C.R. 2006 Computational modeling of fully ionized magnetized plasmas using the fluid approximation. *Phys. Plasmas* **13**, 058103.

SCHWAB, C. 1993 Ideal magnetohydrodynamics: global mode analysis of three-dimensional plasma configurations. *Phys. Fluids B* **5**, 3195.

SCHWARZ, N. *et al.* 2023 Experiments and non-linear MHD simulations of hot vertical displacement events in ASDEX Upgrade. *Plasma Phys. Control. Fusion* **65**, 054003.

SEHMER, T., LACKNER, K., STRUMBERGER, E., FABLE, E., KARDAUN, O., MCCARTHY, P. & the ASDEX Ugrade Team 2016 Growth of axisymmetric instabilities in ASDEX Upgrade. *Fusion Sci. Technol.* **70**, 73.

https://doi.org/10.1017/S0022377826102153 Published online by Cambridge University Press

SEMPF, M., MERKEL, P., STRUMBERGER, E., TICHMANN, C. & GÜNTER, S. 2009 Robust control of resistive wall modes using pseudospectra. *New J. Phys.* **11**, 053015.

SHAFRANOV, V.D. & ZAKHAROV, L.E. 1972 Use of the virtual-casing principle in calculating the containing magnetic field in toroidal plasma systems. *Nucl. Fusion* **12**, 599.

SNYDER, P.B., WILSON, H.R., FERRON, J.R., LAO, L.L., LEONARD, A.W., OSBORNE, T.H., TURNBULL, A.D., MOSSESSIAN, D., MURAKAMI, M. & XU, X.Q. 2002 Edge localized modes and the pedestal: a model based on coupled peeling–ballooning modes. *Phys. Plasmas* **9**, 2037–2043.

SPITZER, L. & HÄRM, R. 1953 Transport phenomena in a completely ionized gas. *Phys. Rev.* **89**, 977.

SPONG, D.A., HIRSHMAN, S.P., LYON, J.F., BERRY, L.A. & STRICKLER, D.J. 2005 Recent advances in quasi-poloidal stellarator physics issues. *Nucl. Fusion* **45**, 918.

STROTH, U., MANZ, P. & RAMISCH, M. 2011 On the interaction of turbulence and flows in toroidal plasmas. *Plasma Phys. Control. Fusion* **53**, 024006.

STRUMBERGER, E. 1997 Finite-β magnetic field line tracing for Helias configurations. *Nucl. Fusion* **37**, 19.

STRUMBERGER, E. & GÜNTER, S. 2017 CASTOR3D: linear stability studies for 2D and 3D tokamak equilibria. *Nucl. Fusion* **57**, 016032.

STRUMBERGER, E. & GÜNTER, S. 2019 Linear stability studies for a quasi-axisymmetric stellarator configuration including effects of parallel viscosity, plasma flow, and resistive walls. *Nucl. Fusion* **59**, 106008.

STRUMBERGER, E., GÜNTER, S., LACKNER, K. & PUCHMAYR, J. 2023 CASTOR3D: linear magnetohydodynamics and diamagnetic drift effects. *J. Plasma Phys.* **89**, 905890309.

STRUMBERGER, E., GÜNTER, S., MERKEL, P., RIONDATO, S. & SCHWARZ, E. 2005 Numerical MHD stability studies: toroidal rotation, viscosity, resistive walls and current holes. *Nucl. Fusion* **45**, 1156.

STRUMBERGER, E., GÜNTER, S., MERKEL, P. & TICHMANN, C. 2014*a* Linear stability studies including resistive wall effects with the CASTOR/STARWALL code. *J. Phys. Conf. Ser.* **561**, 012016.

STRUMBERGER, E., GÜNTER, S. & TICHMANN, C. 2014*b* MHD instabilities in 3D tokamaks. *Nucl. Fusion* **54**, 064019.

STRUMBERGER, E., GÜNTER, S. & the Wendelstein 7-X Team 2020 Linear, resistive stability studies for Wendelstein 7-X-type equilibria with current drive. *Nucl. Fusion* **60**, 106013.

STRUMBERGER, E., PUCHMAYR, J. & HINDENLANG, F. 2025 Linear stability studies for a quasi-axisymmetric equilibrium including plasma flow, drift and viscosity effects. *J. Plasma Phys.* **91**, E157.

SUTTROP, W. *et al.* 2011 First observation of edge localized modes mitigation with resonant and nonresonant magnetic perturbations in ASDEX Upgrade. *Phys. Rev. Lett.* **106**, 225004.

SUTTROP, W. *et al.* 2018 Experimental conditions to suppress edge localised modes by magnetic perturbations in the ASDEX Upgrade tokamak. *Nucl. Fusion* **58**, 096031.

VANOVAC, B. *et al.* 2026 ELM suppression and confinement in NT experiments with stronger shaping in ASDEX Upgrade. *Nucl. Fusion* (submitted).

VIEZZER, E. 2012 Radial electric field studies in the plasma edge of ASDEX Upgrade. *PhD thesis*, Fakultät für Physik der Ludwig-Maximilians-Universität München.

WALTZ, R.E. 1988 Three-dimensional global numerical simulation of ion temperature gradient mode turbulence. *Phys. Fluids* **31**, 1962–1967.

WANG, J., ZHOU, Y., DUAN, J.M., MA, Z.W. & ZHANG, W. 2025 CLT-fx: non-axisymmetric flexible mesh finite difference scheme for stellarator MHD simulations. *Comput. Phys. Commun.* **316**, 109776.

WARMER, F. *et al.* 2024 Overview of European efforts and advances in Stellarator power plant studies. *Fusion Engng Des.* **202**, 114386.

WESSON, J.A. 1978 Hydromagnetic stability of tokamaks. *Nucl. Fusion* **18**, 87.

WESSON, J. 1997 Plasma physics. In *Tokamaks*, International Series of Monographs on Physics, 2nd edn, chap. 2. Clarendon Press.

WILLENSDORFER, M. *et al.* 2019 Dynamics of ideal modes and subsequent ELM crashes in 3D tokamak geometry from external magnetic perturbations. *Plasma Phys. Control. Fusion* **61**, 014019.

https://doi.org/10.1017/S0022377826102153 Published online by Cambridge University Press

WILSON, H.R., COWLEY, S.C., KIRK, A. & SNYDER, P.B. 2006 Magneto-hydrodynamic stability of the H-mode transport barrier as a model for edge localized modes: an overview. *Plasma Phys. Control. Fusion* **48**, A71.

WILSON, H.R., SNYDER, P.B., HUYSMANS, G.T.A. & MILLER, R.L. 2002 Numerical studies of edge localized instabilities in tokamaks. *Phys. Plasmas* **9**, 1277.

WOLF, R.C. *et al.* 2017 Major results from the first plasma campaign of the Wendelstein 7-X stellarator. *Nucl. Fusion* **57**, 102020.

YU, Q. *et al.* 2020 Numerical modeling of the electron temperature crashes observed in Wendelstein 7-X stellarator experiments. *Nucl. Fusion* **60**, 076024.

ZANINI, M. *et al.* 2020 ECCD-induced sawtooth crashes at W7-X. *Nucl. Fusion* **60**, 106021.

ZHOU, Y., ALEYNIKOVA, K. & FERRARO, N.M. 2023 Nonlinear magnetohydrodynamic modeling of current-drive-induced sawtooth-like crashes in the W7-X stellarator. *Phys. Plasmas* **30**, 032503.

https://doi.org/10.1017/S0022377826102153 Published online by Cambridge University Press